Simulation of the Periodontal Ligament During the Initial Phase of Orthodontic Tooth Movement

Dissertation
zur
Erlangung des Doktorgrades (Dr. rer. nat.)
der
Mathematisch-Naturwissenschaftlichen Fakultät
der
Rheinischen Friedrich-Wilhelms-Universität Bonn

von

Albert Heinrich KAISER
aus
Düngenheim

Bonn 2020

Angefertigt mit Genehmigung der Mathematisch-Naturwissenschaftlichen Fakultät der Rheinischen Friedrich-Wilhelms-Universität Bonn.

1. Gutachter:	Prof. Dr. Christoph BOURAUEL
2. Gutachter:	Prof. Dr. Reinhard KLEIN
Tag der Promotion:	08.07.2020
Erscheinungsjahr:	2020

Abstract

The present work is concerned with the simulation of the periodontal ligament response to force in the initial phase of orthodontic tooth movement. This is based on two previous investigations at the Universitätsklinikum Bonn, namely the in vitro experiment of Papadopoulou et al. (2013) with specimens of porcine mandibular premolars, and the in vivo experiment of Konermann et al. (2017) on human upper first incisors.

For the curve fit of the in vitro experiment a model function, assuming viscoelasticity, was introduced. The viscoelastic model function was augmented by a ramp rise time term, to account for observed dependence of the response on actuator velocity, and a previous load history term, to account for the effect of the previous tests on the current test. The correlation coefficient of a curve fit for all tests grouped together was $R^2 = 0.98$. Next, a curve fit of the in vivo experiment was done. Good correlation was found for a simplified model function, without viscoelastic term ($R^2 = 0.96$). Presumably due to the short test duration viscoelastic effects were not evident. For both tests, in vitro and in vivo, the ramp rise time term improved correlation.

The finite element model of Papadopoulou et al. (2013) was adapted for this investigation. The present work indicates that the macroscopic response of the periodontal ligament to an external load can be simulated with a poro-visco-hyperelastic model. For the hyperelastic model of the ground substance, Storåkers constitutive model was used, and parameters identified herein are in good agreement with values published in Bergomi et al. (2011). The simulation showed that poroelastic behaviour will gradually cease when viscoelastic relaxation progresses. This followed also from dimensionless analysis. As a consequence, for slow loading, or if initial response to fast loading is not of interest, a visco-hyperelastic model may suffice.

The curve fit of the model function conceived herein is in good agreement with measured data. The model function includes a ramp rise time term, which could not be covered with the poro-visco-hyperelastic simulation. A supposition to explain this effect on the micro scale is to assume *strain rate hardening*. For soft tissues strain rate effects were observed by other investigators, e.g. David Bell et al. (2018) and Burgin et al. (2014), however the underlying microstructural mechanism is still unknown. Papadopoulou et al. (2013) did not randomise the test sequence with respect to ramp rise time. Therefore, it can not be excluded that the effect is due to test sequence. To clarify this objection, further tests with randomised test sequence are recommended.

Zusammenfassung

In dieser Arbeit wird die Simulation der Reaktion des Periodontiums auf äußere Kräfte in der ersten Phase einer orthodontischen Zahnbewegung behandelt. Dies basiert auf In-vitro-Versuchen von Papadopoulou et al. (2013) an Proben des Prämolars von Schweinen und In-vivo-Untersuchungen von Konermann et al. (2017) an menschlichen Schneidezähnen.

Für die Regression der In-vitro-Daten wurde eine Modellfunktion eingeführt, die viskoelastisches Verhalten beschreibt. Diese wurde durch zwei Ausdrücke erweitert. Der erste beschreibt eine Abhängigkeit von der Geschwindigkeit des Aktuators, der zweite den Einfluss vorangegangener Tests auf den aktuellen Test. Eine Regression aller Tests ergab den Korrelationskoeffizient $R^2 = 0{,}98$. Anschließend wurde eine Regression der In-vivo-Daten durchgeführt. Eine gute Korrelation wurde für eine vereinfachte Modellfunktion ohne Viskoelastizität gefunden ($R^2 = 0{,}96$). Vermutlich waren viskoelastische Effekte aufgrund der kurzen Testdauer nicht erkennbar. Für beide Versuche, in vitro und in vivo, verbesserte der Ausdruck für die Geschwindigkeit des Aktuators die Korrelation.

Das Finite-Elemente-Modell von Papadopoulou et al. (2013) wurde angepasst. Die vorliegende Arbeit zeigt, dass die makroskopische Reaktion des Periodontiums auf eine externe Last mit einem poro-visko-hyperelastischen Modell simuliert werden kann. Für das hyperelastische Material wurde das Modell von Storåkers verwendet. Die hierfür gefundenen Parameter stimmen gut mit den Werten von Bergomi et al. (2011) überein. Die Simulation zeigt, dass poroelastisches Verhalten ausklingt, wenn viskoelastische Relaxation fortschreitet. Dies lässt auch eine dimensionslose Analyse erwarten. Daher kann für eine langsame Belastung, oder wenn die anfängliche Reaktion auf schnelle Belastung nicht von Interesse ist, ein visko-hyperelastisches Modell ausreichen.

Die Modellfunktion beinhaltet einen Ausdruck der eine Abhängigkeit von der Geschwindigkeit des Aktuators beschreibt. Dieser Effekt konnte nicht mit der poro-visko-hyperelastischen Simulation abgedeckt werden. Eine mögliche Erklärung ist dehnratenabhängige Verfestigung. Auch David Bell et al. (2018) und Burgin et al. (2014) haben dehnratenabhängig Effekte an biologischen Geweben beobachtet, die zugrundeliegenden mikro-mechanischen Mechanismen sind noch unbekannt. Die Versuchsreihe von Papadopoulou et al. (2013) wurde nicht bezüglich der Geschwindigkeit des Aktuators randomisiert. Daher kann ein Sequenzeffekt nicht ausgeschlossen werden. Um diesen Einwand auszuräumen, werden Versuche mit randomisierter Test Sequenz empfohlen.

Danksagung

Mein Dank gebührt Prof. Dr. Christoph Bourauel, dem Leiter des Instituts für Oralmedizinische Technologie am Universitätsklinikum Bonn und seinem Mitarbeiter Dr. Ludger Keilig. Beide haben durch zahlreiche Fragen, Anregungen und Diskussionen zum Gelingen der Arbeit beigetragen. Auch danke ich den ehemaligen Doktorandinnen am Institut auf deren Messungen meine Arbeit aufbaut, Dr. med. dent. Konstantina Papadopoulou und Prof. Dr. med. dent. Anna-Christin Konermann. Des Weiteren danke ich Prof. Dr. Reinhard Klein für die Zweitbetreuung meiner Arbeit.

Ich danke meinem Kollegen Dr.-Ing. Axel Hänschke, der mich in der ersten Phase meines Vorhabens unterstützt hat. Ebenso dem ehemaligen Mitarbeiter am Institut für Numerische Simulation der Universität Bonn, Dr. Christian Gross, für Einblicke in die Anwendung neuere Methoden der Informatik im Bereich des wissenschaftlichen Rechnens.

Auch danke ich meinen Lehrern, insbesondere Prof. Dr. Reinhard Bressler von der Hochschule Koblenz. Er organisierte ein vom DAAD gefördertes Austauschprogramm mit der University of Tennessee, Knoxville, USA, an dem ich teilnahm. Des Weiteren nennen möchte ich meinen Physiklehrer an der Fachoberschule Cochem, Dipl.-Ing. (FH) Wilfried Luy. Die analytische Betrachtungsweise, die er vermittelte, geleitete mich sicher durch Studium und Beruf.

Danken möchte ich meinem Sohn Simon für die beharrliche Ablenkung, sowie meinen Eltern Alfons Kaiser und Sybilla Kaiser, geb. Johann, für Zuversicht und langen Atem.

Contents

Chapter 1

Introduction

For decades, orthodontic tooth movement (OTM) has been subject of extensive research. A classification of OTM is given in Davidovitch and Krishnan (2015),

> The magnitude of orthodontic forces has received significant attention. It was previously reported ... that light pressure produces favorable tooth displacement, resulting in minimal discomfort and pain to the patient, whereas heavy pressure, exceeding 20–25 g/cm^2 of root surface (Schwarz, 1932) produces a classical three-phase reaction ... In 1962, Burstone suggested that, if the rates of OTM were plotted against time, there would be three phases of OTM: the initial phase, a lag phase, and a postlag phase ... The initial phase is characterized by a period of very rapid movement, which occurs immediately after application of force to the tooth. This rate is attributed to the displacement of the tooth within the PDL space and bending of the alveolar bone. This phase is followed by a lag period, when no or low rates of tooth displacement occur. This lag results from hyalinization of the PDL in areas of compression. No further tooth movement will occur until cells complete the removal of all necrotic tissues. During the third phase, the rate of movement gradually or suddenly increases. [1]

The present work is concerned with simulation of the periodontal ligament (PDL) response to force in the initial phase of orthodontic tooth movement. This is based on two previous investigations at the Universitätsklinikum Bonn, namely the in vitro experiment of Papadopoulou et al. (2013) with specimens of porcine mandibular premolars, and the in vivo experiment of Konermann et al. (2017) on human upper first incisors. In the first experiment, biochemical in vivo processes are not present. For both tests, test time was well within the limits of OTM initial phase.

---

[1] The references in the citation are Schwarz (1932) and Burstone (1962).

Exemplary, a review of biochemical processes involved in orthodontic tooth movement is found in Schroeder (1986) and the edited volume of Krishnan and Davidovitch (2015). The periodontium is a compound of several tissues that support the teeth. It includes the gingiva, the cementum, the periodontal ligament and the alveolar bone proper. The textbook of Hand and Frank (2015) describes the periodontal ligament function and structure,

> The periodontal ligament attaches the tooth root to alveolar bone, and it serves to absorb and resist the forces of occlusion on the tooth. It consists of collagenous fiber bundles ... The collagen fibrils and other extracellular matrix components are synthesized and maintained by periodontal ligament fibroblasts. Type I collagen is the major constituent of the fibers, ... The periodontal ligament fiber bundles are embedded, as Sharpey's fibers, in cementum on the root and in the alveolar bone facing the tooth. The embedded portions of Sharpey's fibers are fully mineralized in acellular cementum and partially mineralized in cellular cementum and bone. Interstitial areas containing loose connective tissue, blood vessels, and nerves are present between the fiber bundles in the periodontal ligament. These interstitial areas are continuous with openings through the alveolar bone (Volkmann's canals) to the marrow spaces of the alveolar process.

In general, a ligament is soft tissue that connects bone to bone and its mechanical function is to guide and restrict relative motion of joints. A tendon is a soft tissue that connects muscle to bone and its mechanical function is to carry tensile loads from muscle to bone. Tendons and ligaments are similar in composition and structure. In Chap. 16 of Cowin and Doty (2007) tendons and ligaments are described,

> Tendons and ligaments are constituted mainly of fibers of fibrous type I collagen and are dense, often parallel-fibered, tissues. ... Generally, tendons and ligaments consist of about $20\,\%$ cellular material and about $80\,\%$ extracellular material; the extracellular material is further subdivided into about $30\,\%$ solids and $70\,\%$ water. These extracellular solids are collagen, the ground substance, and a small amount of elastin (1 to $2\,\%$ of dry weight). The collagen content is generally over $75\,\%$ and is somewhat greater in tendons than in ligaments ... in tendons of the extremities the collagen may be up to

> $99\,\%$ of dry weight. ... The ground substance in ligaments and tendons consists of proteoglycans (PGs) (up to about $20\,\%$ of the solids) along with structural glycoproteins, plasma proteins, and a variety of small molecules. ... Although the exact mechanical roles of PGs in ligaments and tendons are unknown, as they are in bone, it is likely that the large PG aggregates function similarly to those in articular cartilage, binding extracellular water to create a gel-like material extrafibrillar matrix. ... The broad, general description of the structure of tendons and ligaments is that the collagenous fibers composing the tendons have a parallel arrangement and that the collagenous fibers composing ligaments may not be completely parallel but are close to parallel with one another. ... A broad general description of the fiber structure of unstressed tendons is that they exhibit gentle planar sinusoidal waviness. ... The waviness in unstressed tendons is called the "crimp" of collagen.

The collagen fibre axes of tendons and ligaments are aligned with the predominant loading direction in vivo. Tensile tests of tendons and ligaments are typically done with specimens, where collagen fibre axes are aligned with the load direction. The stress strain curve observed depicts a progressive behaviour and is typically divided into three regions (e.g. Holzapfel (2001)): At first, in the *toe region*, small force levels are necessary to elongate the tissue initially. Then, in the *heel region*, with increased load a progressively increased force is observed. The crimped collagen fibres gradually line up with load direction and at the end of the heel region, when collagen fibres are straightened, a transition into the *linear region* is observed. Here the stress strain curve is dominated by the straightened collagen fibres. At the end of the linear region, with gradual failure of highly stretched fibre bundles, drops in the stress strain curve and ultimate failure is observed. When subject to dynamic loads tendons and ligaments show viscoelastic behaviour. Minns et al. (1972) associated this with the shear interaction of the interfibre matrix, that is, with the interaction of the collagen fibres with the ground substance proteoglycans.

Now we want to elaborate on points, that distinguish the periodontal ligament from other ligaments. As mentioned above, the common ligament is loaded in tension, whereas under forces of occlusion, regions of tension and compression are observed in the periodontal ligament. Therefore it is anticipated that compression behaviour has a significant contribution to the overall response of the periodontal ligament. With respect to that, it may have similarities to cartilage. A second point is the vascular system of the periodontal ligament, which is not found in the common ligament. Cowin and Doty (2007) state for bone tissue a vascular relaxation time of $1.36\,\mu\mathrm{s}$ and argued that: 'even under accidental impact loading, the stress rise time never approaches the vascular porosity relaxation time.' On these grounds, for the tests considered here, the contribution of the vascular system may be negligible. However, after loading, blood pressure variations in the vascular system may play a significant role in the recovery of the periodontal ligament in vivo.

Concluding, a numerical model of the periodontal ligament should capture the progressive characteristic of the stress strain curve and the viscous behaviour mentioned above. It is clear that linear elastic models are not sufficient. The progressive characteristic suggests to choose a suitable hyperelastic constitutive material model. To account for viscous effects a viscoelastic model, a poroelastic model or a combination of these models is conceivable.

At this point it is instructive to distinguish the basic principle of the viscoelastic and poroelastic phenomenological model. Assume a representative control volume of the periodontal ligament exhibits only viscoelastic behaviour. Then, there is no flow of the interstitial fluid across the boundary of the control volume. The viscous behaviour could be due to the above mentioned interaction of the collagen fibres with the ground substance proteoglycans. Contrary, if the periodontal ligament exhibits only poroelastic behaviour, then a net flow across the boundary of the control volume is possible. This could be due to a pressure gradient induced flow of the interstitial fluid. It is conceivable that both effects take place at the same time.

A review of models for periodontal ligament is found in Fill et al. (2012). They point out the discrepancies in the literature of the various model approaches used and in the periodontal ligament's mechanical properties published. Previous periodontal ligament models, the author would like to highlight, are the quasi-linear viscoelastic model used by Toms et al. (2002) and the poro-hyperelastic model used by Bergomi et al. (2011). The findings of Fill et al. (2012) are,

> Results: The review revealed that significant variations exist, some on the order of six orders of magnitude, in the PDL's elastic constants and mechanical properties. Possible explanations may be attributable to different modelling approaches and behavioural assumptions.

> Significance: The discrepancies highlight the need for further research into determining what the key factors that contribute to tooth movement are, their correlations and their degree of impact. Despite the PDL's definitive role in orthodontic tooth movement, proposed models of the PDL's mechanical behaviour thus far have been unsatisfactorily inadequate. Hence, there is a need to develop a robust PDL model that more accurately simulates the PDL's biomechanical response to orthodontic loads. Better understanding of the PDL's biomechanical behaviour under physiologic and traumatic loading conditions might enhance the understanding of the PDL's biologic reaction in health and disease.

Obviously, the author agrees with the conclusion. Though part of the discrepancies may be revealed by a thorough investigation considering first principles and bias towards recent publications.

This work is structured as follows: First, in Chap. 2, suitable constitutive models, and basic concepts of poroelasticity and viscoelasticity are discussed. Than, in Chap. 3, an attempt is made, based on dimensionless analysis, to classify the experimental setup and distinguish poroelasticity and viscoelasticity. In Chap. 4, a curve fit of the in vitro experiment of Papadopoulou et al. (2013) and the in vivo experiment of Konermann et al. (2017), is described. For this, a model function, assuming viscoelasticity, is introduced. In order to improve correlation, the model function is successively refined, taking additional effects identified into account. In Chap. 5, the in vitro experiment of Papadopoulou et al. (2013) is simulated. First, in a static analysis, parameters of two constitutive models were identified. Then, visco-hyperelastic and poro-visco-hyperelastic response were simulated, and model parameters identified, that maximise correlation to the suitable model function. Finally, in Chap. 6, summary, discussion and conclusion follows.

Chapter 2

Review of Constitutive Models, Poro- and Viscoelasticity

2.1 Constitutive Models

2.1.1 Introduction

Stresses inside a body result from deformation of the material caused by external and internal loads. *Constitutive equations* relate the stress in a material body to a measure of deformation, such as strain, and must satisfy certain physical principles. For example, constitutive equations must be *objective*, i.e. they must be frame invariant. A *Cauchy-elastic* or *elastic* material is one for which the stress field at time t and point x solely depends on the state of deformation and temperature at that time, and there is no dependence on the history of these variables. A material is called *Green-elastic* or *hyperelastic*, if there exists a *Helmholtz free-energy potential* Ψ, whose derivative with respect to a strain measure gives the corresponding stress, and whose derivative with respect to temperature gives the heat flux vector. When the potential is only a function of a strain measure, the potential is called *strain energy density function* and is often denoted by U. As a consequence, the work done by the stresses during isothermal deformation depends only on the initial and final state, that is, the work done is *path independent*.

The strain energy density function U must be invariant when the material body undergoes a rigid body rotation. This implies that U depends only on the stretch component of the deformation measure. For an *isotropic* material the behaviour is identical in any material direction, i.e. U must be a function of the invariants of the deformation measure.

Ogden (1972) proposed a strain energy density function as a linear combination of the strain invariants, given by the principle stretches $\lambda_i, i \in \{1, 2, 3\}$, that has the form

$$U\left(\lambda_1, \lambda_2, \lambda_3\right) = \sum_{i=1}^{N} \frac{\mu_i}{\alpha_i}\left(\lambda_1^{\alpha_i} + \lambda_2^{\alpha_i} + \lambda_3^{\alpha_i} - 3\right), \tag{2.1}$$

where N is the number of terms summed, and μ_i and α_i are material constants that are determined by curve fitting of experimental data. For incompressible material, which implies $\lambda_1\lambda_2\lambda_3 = 1$, with $N = 1$ and $\alpha_1 = 2$ the *neo-Hookean* form proposed by Treloar (1943), and with $N = 2$, $\alpha_1 = 2$ and $\alpha_2 = -2$ the *Mooney–Rivlin* form proposed by Mooney (1940) and Rivlin (1948), follows. Various other strain energy density functions have been proposed, that are not derived from the Ogden model. Arruda and Boyce (1993) derived a strain energy density function from statistical models of chain orientations in polymers. Based on thermodynamic equations of state of a real gas, Kilian et al. (1986) suggested by analogy the *van der Waals* stain energy potential. The Yeoh (1990) and Marlow (2003) model are functions of the first strain invariant.

Various parameters of the strain energy density function are determined by curve fitting to test data. The Ogden, Mooney-Rivlin and van der Waals model require experimental data from multiple test modes, e.g. uniaxial and equibiaxial, for curve fitting. 'If limited test data are available for calibration, the Arruda-Boyce, van der Waals, Yeoh, or reduced polynomial forms provide reasonable behaviour. When only one set of test data (uniaxial, equibiaxial, or planar test data) is available, the Marlow form is recommended. In this case a strain energy potential is constructed that will reproduce the test data exactly and that will have reasonable behaviour in other deformation modes.' (ABAQUS (2016), Analysis Users Guide, Chap. 22.5.1).

2.1.2 A Hyperelastic Constitutive Model for Compressible Material - The Storåkers Model

For *compressible* materials, the strain energy density function U is split up in a deviatoric U_{dev} and a volumetric U_{vol} part,

$$U(\hat{I}, J) = U_{dev}(\hat{I}) + U_{vol}(J), \tag{2.2}$$

with the first deviatoric strain invariant $\hat{I} = \hat{\lambda}_1^2 + \hat{\lambda}_2^2 + \hat{\lambda}_3^2$, defined in terms of the deviatoric stretches $\hat{\lambda}_i = J^{-\frac{1}{3}}\lambda_i$, and the determinant of the deformation gradient J.

Storåkers (1986) proposed the strain energy density function

$$U\left(\hat{\lambda}, J\right) = \sum_{i=1}^{N} \frac{2\mu_i}{\alpha_i^2} \left[\left(\hat{\lambda}_1^{\alpha_i} + \hat{\lambda}_2^{\alpha_i} + \hat{\lambda}_3^{\alpha_i} - 3 \right) + \frac{1}{\beta_i} \left(J^{-\alpha_i \beta_i} - 1 \right) \right], \tag{2.3}$$

where N is the number of terms used, μ_i, α_i and β_i are material parameters, $\hat{\lambda}_i = J^{-\frac{1}{3}}\lambda_i,\ i \in \{1,2,3\}$ are the deviatoric stretches, and J is the determinant of the deformation gradient. Observe that the first term, in round brackets, represents the deviatoric part, which is defined analogue to an Ogden Material Eq. 2.1, except that deviatoric stretches are used, and the second term represents the volumetric part.

According to ABAQUS (2016), Analysis User's Manual, Chap. 19.5.2, ' The coefficients μ_i are related to the initial shear modulus, μ_0, by

$$\mu_0 = \sum_{i=1}^{N} \mu_i,$$

while the initial bulk modulus, K_0, follows from

$$K_0 = \sum_{i=1}^{N} 2\mu_i \left(\frac{1}{3} + \beta_i \right).$$

For each term in the energy function, the coefficient β_i determines the degree of compressibility. β_i is related to the Poisson's ratio, ν_i, by the expressions

$$\beta_i = \frac{\nu_i}{1 - 2\nu_i} \qquad \text{and} \qquad \nu_i = \frac{\beta_1}{1 + 2\beta_i}.$$

Thus, if β_i is the same for all terms, we have a single effective Poisson's ratio, ν.'

Storåkers (1986) showed, that for an uniaxial state of stress, and with $N = 1$, the stress-stretch relation is

$$\sigma = \frac{2\mu}{\alpha} \left(\lambda^{-\alpha \frac{1+3\beta}{1+2\beta}} - 1 \right) \lambda^{\alpha - 1}. \tag{2.4}$$

2.1.3 A First-Invariant Hyperelastic Constitutive Model - The Marlow Model

The constitutive model described in this chapter was published by Marlow (2003), based on earlier work of Gough et al. (1999).

The invariants of the left Cauchy-Green deformation tensor $\mathbf{b} = \mathbf{F}\mathbf{F}^T$, with deformation gradient $\mathbf{F}$, are,

$$I(\mathbf{b}) = tr(\mathbf{b}) \, , \tag{2.5a}$$

$$II(\mathbf{b}) = tr(\mathbf{b}^2) \, , \tag{2.5b}$$

$$III(\mathbf{b}) = det(\mathbf{b}) \, . \tag{2.5c}$$

The invariants can be written in terms of the principle stretches $\lambda_i, i \in \{1, 2, 3\}$,

$$I(\mathbf{b}) = \lambda_1^2 + \lambda_2^2 + \lambda_3^2 \, , \tag{2.6a}$$

$$II(\mathbf{b}) = \lambda_1^4 + \lambda_2^4 + \lambda_3^4 \, , \tag{2.6b}$$

$$III(\mathbf{b}) = \lambda_1^2 \, \lambda_2^2 \, \lambda_3^2 \, . \tag{2.6c}$$

Assuming incompressible material, the determinant of the deformation gradient $\mathbf{F}$ is 1, and from Eq. 2.6c follows

$$\lambda_3^2 = \frac{1}{\lambda_1^2 \lambda_2^2} \, . \tag{2.7}$$

The first invariant, Eq. 2.6a, can be written with Eq. 2.7, in terms of the first and second principle stretch:

$$I(\mathbf{b}) = \lambda_1^2 + \lambda_2^2 + \frac{1}{\lambda_1^2 \lambda_2^2} = I(\lambda_1, \lambda_2) \, . \tag{2.8}$$

Consider a uniaxial load, with the force applied in e_1 direction. Then $\sigma_1 \neq 0$, $\sigma_2 = \sigma_3 = 0$, and $\varepsilon_2 = \varepsilon_3 = -\nu\varepsilon_1$, where ν is Poisson's ratio. Therefore, $\lambda_2 = \lambda_3$, and from Eq. 2.7 follows

$$\lambda_2 = \frac{1}{\sqrt{\lambda_1}} \, . \tag{2.9}$$

With Eq. 2.9, we can write Eq. 2.8 in terms of the first principle stretch

$$I(\mathbf{b}) = \lambda_1^2 + \frac{2}{\lambda_1} = I(\lambda_1) \, . \tag{2.10}$$

Equation 2.10 is a mapping of the uniaxial stretch λ_1 to the first invariant of the left Cauchy-Green deformation tensor. We split the domain in compression and tension. That is, in compression $(0,1) \ni \lambda_1 \rightarrow I(\lambda_1) \in (\infty, 3)$, in tension $(1,\infty) \ni \lambda_1 \rightarrow I(\lambda_1) \in (3,\infty)$, and with minimum at $I(\lambda_1 = 1) = 3$.

Consider a general deformation, with a particular value of the first invariant at a material point called $\widehat{I}$. Assuming uniaxial load and incompressible material, we can find the first principle stretch λ_1, with the same first invariant $\widehat{I}$, by rearranging Eq. 2.10,

$$\lambda_1^3 - \lambda_1 \widehat{I} + 2 = 0\,. \tag{2.11}$$

This is a third order polynomial. Consider the discriminant (Bronstein et al. (2005), Chap. 1.6.2.3) of the polynomial. For $\widehat{I} = 3$ the discriminant is zero, i.e. we have three real roots, with one double root $\lambda_1 = 1$. For $\widehat{I} > 3$, the discriminant is greater than zero, i.e. we have three distinct real roots. Taking into account *Descartes' Rule of Signs* (e.g. Bronstein et al. (2005), Chapter 1.6.3.2), and noting that the polynomial in λ_1 has two sign changes, whereas the polynomial in $-\lambda_1$ has one sign change, we conclude that there are two positive real roots and one negative root of the cubic polynomial. The negative root can be discarded, since stretch is greater than zero. Further, the polynomial is already in reduced form. The roots may be obtained using *Cardano's formula* (Beyer (1984)). Applied to our cubic in λ_1, we can find the roots dependent on first invariant at a material point $\widehat{I} \in (3,\infty)$, and establish the limits $\lim_{\widehat{I}\rightarrow 3}(\lambda_k) = (-2,1,1)$. For $\widehat{I} \rightarrow \infty$ we have $\lim_{\widehat{I}\rightarrow\infty}(\lambda_k) = (-\infty, 0, \infty)$. A plot of the roots of Eq. 2.11 is shown in Fig. 2.1. The positive roots represent the compression and tension part for an uniaxial test.

For a general deformation at a material point, with $\lambda_1 > 1$, $\lambda_2, \lambda_3 \in (0,1)$, and corresponding first invariant $\widehat{I} > 3$, we find a unique equivalent stretch $\lambda_1 > 1$, with the same first invariant, which henceforth will be called λ_t. A similar argument can be made for compression with $\lambda_1 \in (0,1)$, $\lambda_2, \lambda_3 > 1$.

Suppose from a uniaxial tension test, we have the uniaxial stress, $\sigma_t = \sigma_1$, versus strain, $\varepsilon_t = \varepsilon_1 = \lambda_1 - 1$, diagram. The corresponding strain energy density function is obtained by integrating the uniaxial stress strain graph. For the lower boundary of the integral we choose zero, since in the absence of stretch, the strain energy density must be zero, i.e. $U(I=3) = 0$. The upper boundary of the integral is $\varepsilon_t = \lambda_t(I) - 1$:

$$U(I) = \int_0^{\lambda_t(I)-1} \sigma_t(\varepsilon_t) d\varepsilon_t\,. \tag{2.12}$$

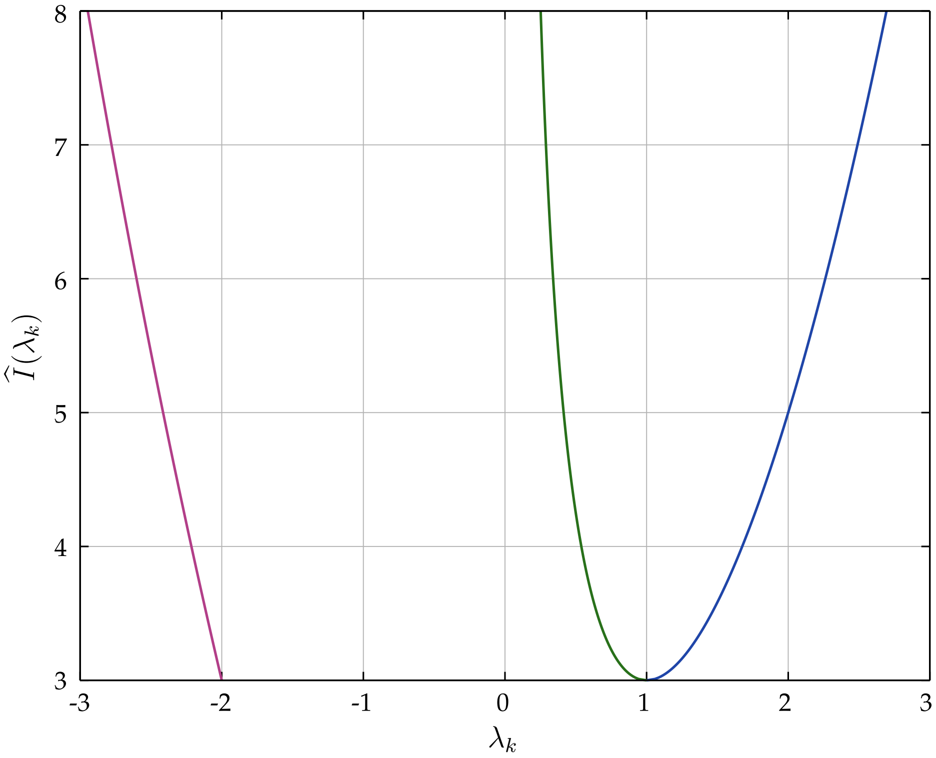

FIGURE 2.1: Roots of Eq. 2.11, that is, the principle stretch $\lambda_k, k \in \{1,2,3\}$, depending on the first invariant $\widehat{I}$, representing left to right, a non physical solution (red), uniaxial compression (green) and uniaxial tension (blue).

For uniaxial tension, the strain energy density function Eq. 2.12 will reproduce the measured stress-strain response used in the integral precisely.

Consider *equibiaxial tension*, with $\sigma_{11} = 0$, $\sigma_{22} = \sigma_{33} = \sigma_{eb}$, and $\lambda_2 = \lambda_3 = \lambda_{eb}$. Than, with the incompressibility condition and Eq. 2.6c follows $\lambda_1 = \lambda_{eq}^{-2}$. The first invariant of the Cauchy-Green deformation tensor is $I(\lambda_{eb}) = 2\lambda_{eb}^2 + \lambda_{eb}^{-4}$. Observe that for equibiaxial tension and uniaxial compression, there is a bijective mapping of the deformation, and therefore also of the strain energy density. Taking the derivative of the strain energy density function with respect to stretch, gives the corresponding stress, $\sigma_{eb} = (\partial U(I)/\partial I)(\partial I/\partial \lambda_{eb})$, and observing that there is a factor of 2 in front of the integral in the biaxial case, we find

$$\sigma_{eb} = \frac{\lambda_{eb} + \lambda_{eb}^{-5}}{\lambda_t(I_{eb}) + \lambda_t(I_{eb})^{-2}} \sigma_t(\lambda_t(I_{eb}) - 1) \,. \tag{2.13}$$

Consider *plane strain*[1], then by definition $\lambda_3 = 1$. Call the first principle

---

[1] Marlow (2003) used the term *planar traction*.

stretch $\lambda_1 = \lambda_p$. By virtue of the incompressibility condition and Eq. 2.6c, the second principle stretch is $\lambda_2 = \lambda_p^{-1}$, and the first invariant of the Cauchy-Green deformation tensor is $I(\lambda_p) = \lambda_p^2 + \lambda_p^{-2} + 1$. Again, taking the derivative of the strain energy density function with respect to stretch gives

$$\sigma_p = \frac{\lambda_p + \lambda_p^{-3}}{\lambda_t(I_p) + \lambda_t(I_p)^{-2}} \sigma_t(\lambda_t(I_p) - 1) \,. \tag{2.14}$$

For compressible material, the deviatoric part of the strain energy density is defined by the Marlow model Eq. 2.12, and the volumetric part by appropriate volumetric response data, e.g. the bulk modulus.

2.2 Poroelasticity

2.2.1 Introduction

The subject of poroelasticity is the study of fluid filled, porous media. Terzaghi (1923) proposed a model of one-dimensional soils consolidation, to account for the influence of pore fluid on the quasi static deformation of clay soils. Rendulic (1936) generalised this theory to the three-dimensional case. Development of the three dimensional, linear theory of poroelasticity, taking compression of the pore fluid and solid phase into account, is in principle due to Biot (1941). Later works include the effect of dynamic loading and stress waves, Biot (1956a) and Biot (1956b), and of nonlinear elasticity, Biot (1973). Rice and Cleary (1976) used canonical notation of solid mechanics and linked poroelastic parameters to the limiting behaviour of drained and undrained response, which, in the opinion of the author, considerably elucidated physical interpretation of asymptotic poroelastic phenomena. An alternative approach to the subject, based on Truesdell's metaphysical principles (Truesdell, 1969) and mixture theory, was used by e.g. Bowen (1980), Boer and Ehlers (1986), and Coussy (1995). Their derivation of the governing equations was based on mixture theory, however the numerical implementation resorted to the effective stress principle of poroelasticity. This may have motivated the remark of Cheng and Detournay (1993), 'Alternative theories have also been developed using the formalism of mixtures theory, in practice they do not offer any advantage over the Biot theory.'

According to Verruijt (2013), 'The linear theory of poroelasticity (or consolidation) has now reached a stage where there is practically general consensus on the basic equations, see e.g. Cheng and Detournay (1993), Boer (2000), Wang (2000), Rudnicki (2001), Coussy (2004), Gambolati (2006) and Verruijt (2008). Unfortunately, there is no general agreement on the definitions and the notations of the basic physical parameters in the theory of poroelasticity or consolidation.'

The presentation of poroelastic theory in this chapter is restricted to linear elastic solids and follows along the lecture notes of Rice (1998), revision 2013, at Harvard University. Notation used by Cheng and Detournay (1993), in particular the concept of porosity and fluid mass content, were added, to ease comprehension and provide quantities accessible by measurement.

2.2.2 Constitutive Equations for Ideal Poroelasticity

The stress-strain relations for a linear elastic isotropic solid, with no pore pressure effects present, is given by (e.g. Bonet and Wood (2008))

$$\sigma_{ij} = 2\mu\varepsilon_{ij} + \lambda\varepsilon_{kk}\delta_{ij} \ , \tag{2.15}$$

where ε_{kk} is the trace of the strain tensor ε_{ij}, and δ_{ij} is the Kronecker delta, defined by $\delta_{ij} = 1$ if i=j and $\delta_{ij} = 0$ else. Note that, to describe the behaviour of a linear elastic isotropic solid, two independent elastic constants, the *Lamè coefficients* μ and λ, are sufficient. They are related to *Young's modulus* E, *Poisson ratio* ν, and the *shear modulus* G by

$$\mu = G = \frac{E}{2(1+\nu)} \ , \tag{2.16}$$

$$\lambda = \frac{\nu E}{(1+\nu)(1-2\nu)} \ . \tag{2.17}$$

With this, the stress-strain relation for a linear elastic isotropic solid is

$$\sigma_{ij} = \frac{E}{1+\nu}\varepsilon_{ij} + \frac{\nu E}{(1+\nu)(1-2\nu)}\varepsilon_{kk}\delta_{ij} \ . \tag{2.18}$$

Taking the trace of Eq. 2.18 gives

$$\varepsilon_{kk} = \frac{1-2\nu}{E}\sigma_{kk} = \frac{\sigma_{kk}}{3K} \ , \tag{2.19}$$

where K is the *bulk modulus*

$$K = \frac{E}{3(1-2\nu)} \ , \tag{2.20}$$

relating *hydrostatic stress*, defined by

$$\sigma_h = \frac{\sigma_{kk}}{3} \tag{2.21}$$

and *volume dilatation* ε_{kk}. Substitute Eq. 2.19 into Eq. 2.18 and inverting the stress-strain relation gives

$$\varepsilon_{ij} = \frac{1+\nu}{E}\sigma_{ij} - \frac{\nu}{E}\sigma_{kk}\delta_{ij} \ . \tag{2.22}$$

For reasons that become obvious later, we rewrite the stress-strain Eq. 2.18 and Eq. 2.22, using the elastic constants shear modulus G and bulk modulus K

$$\sigma_{ij} = 2G\varepsilon_{ij} + (K - \frac{2G}{3})\varepsilon_{kk}\delta_{ij} \; , \tag{2.23}$$

$$\varepsilon_{ij} = \frac{1}{2G}\sigma_{ij} - (\frac{1}{6G} - \frac{1}{9K})\sigma_{kk}\delta_{ij} \; . \tag{2.24}$$

For porous media, assume that the total stresses can be additively decomposed into effective stresses, i.e. the part of the total stresses that governs the deformation of solid phase, and the pore pressure contribution. When pore pressure p in the liquid phase is present, the change in stress is proportional to the pore pressure in the liquid phase. The proportionality factor is called *Biot–Willis coefficient* α. Based on stress-strain Eq. 2.23, the *effective stress* for a linear elastic isotropic solid, with pore pressure effects present, is total stress minus the pore pressure contribution:

$$\sigma_{ij} = 2G\varepsilon_{ij} + (K - \frac{2G}{3})\varepsilon_{kk}\delta_{ij} - \alpha p\delta_{ij} \; . \tag{2.25}$$

Inverting Eq. 2.25, strain is the sum of an effective stress and the pore pressure contribution:

$$\varepsilon_{ij} = \frac{1}{2G}\sigma_{ij} - (\frac{1}{6G} - \frac{1}{9K})\sigma_{kk}\delta_{ij} + \frac{\alpha}{3K}p\delta_{ij} \; . \tag{2.26}$$

We now consider the additive split of the stress and strain tensor in a deviatoric part (σ'_{ij}, ε'_{ij}) and a volumetric part (also called spherical or hydrostatic part), i.e.

$$\sigma_{ij} = \sigma'_{ij} + \frac{1}{3}\sigma_{kk}\delta_{ij} \; , \tag{2.27}$$

$$\varepsilon_{ij} = \varepsilon'_{ij} + \frac{1}{3}\varepsilon_{kk}\delta_{ij} \; . \tag{2.28}$$

Substituting Eq. 2.28 into Eq. 2.25 gives:

$$\sigma_{ij} = 2G\varepsilon'_{ij} + K\varepsilon_{kk}\delta_{ij} - \alpha p\delta_{ij} \; . \tag{2.29}$$

Comparing Eq. 2.27 and Eq. 2.29, we observe that the stress-strain Eq. 2.29 consists of a uncoupled deviatoric and volumetric response:

$$\sigma'_{ij} = 2G\varepsilon'_{ij} \,, \tag{2.30a}$$

$$\frac{\sigma_{kk}}{3} = K\varepsilon_{kk} - \alpha p \,. \tag{2.30b}$$

Consider Eq. 2.30 and assume constant strain. Than, if pore pressure is increased by ∂p, normal stresses are decreased by $-\alpha\partial p\delta_{ij}$ and $\partial\sigma_{kk} = -\alpha 3\partial p$.

Substituting Eq. 2.27 into Eq. 2.26, we find the uncoupled strain-stress relation:

$$\varepsilon_{ij} = \frac{1}{2G}\sigma'_{ij} + \frac{1}{9K}\sigma_{kk}\delta_{ij} + \frac{\alpha}{3K}p\delta_{ij} \,, \tag{2.31}$$

with deviatoric and volumetric response

$$\varepsilon'_{ij} = \frac{1}{2G}\sigma'_{ij} \,, \tag{2.32a}$$

$$\varepsilon_{kk} = \frac{1}{3K}\sigma_{kk} + \frac{\alpha}{K}p \,. \tag{2.32b}$$

2.2.3 Drained and Undrained Boundary Condition

The bulk modulus K is the bulk modulus with *drained boundary condition*. Drained boundary condition corresponds to deformation of the porous media, with pore fluid allowed to flow in or out of the representative elementary volume, and constant pore pressure. Alternatively, one can consider the long term response, when pore pressure comes back to its original value, after instantaneous deformation response.

On the other hand, *undrained boundary condition* refers to the case where pore fluid is not allowed to flow in or out of the deforming porous media. In general, undrained deformation will induce a pore pressure change. Alternatively, one can consider the instantaneous deformation response, when the time period is too short for pore fluid to move in or out of the representative elementary volume.

It is well known, that the trace of the deviatoric stress tensor is zero and that deviatoric deformation does not involve volume change, that is $\sigma'_{kk} = 0$ and $\varepsilon'_{kk} = 0$ (e.g. Bonet and Wood (2008)). Therefore deviatoric deformation does not cause a pressure change in the pore fluid, and the shear modulus G is identical for drained and undrained boundary condition. This is also evident from Eq. 2.32, observing that deviatoric and volumetric response are uncoupled.

Consider a porous material of representative elementary volume V, in a stress and pressure free reference state, containing the volume of fluid V_f and the mass of fluid M_f. Then *porosity* n, and *fluid mass content* m, are defined as

$$n = \frac{V_f}{V} \, , \tag{2.33}$$

$$m = \frac{M_f}{V} \, . \tag{2.34}$$

We assume, that the pore space is connected and fully saturated with fluid, i.e. there is no trapped fluid, and pore space is equal to the void space. With the density of the fluid $\rho_f = M_f/V_f$, it is evident that

$$m = \rho_f n \, . \tag{2.35}$$

The variation in fluid mass content

$$\delta m = \delta \rho_f n + \rho_f \delta n \tag{2.36}$$

is due to two effects, the variation in fluid density, and the variation in porosity. The variation in fluid density can be accounted to volume dilatation of the fluid $(\varepsilon_{kk})_f = dV_f/V_f = -p/K_f$, where K_f is the bulk modulus of the fluid. Consider a representative elementary fluid volume of constant mass in reference configuration dV_f and deformed configuration dv_f. From conservation of mass $\rho_f^0 dV_f = \rho_f dv_f$, we obtain the relation for fluid density $\rho_f J_f = \rho_f^0$, with $J_f = dv_f/dV_f$. We can now write the variation in fluid density as $\delta\rho_f = \rho_f - \rho_f^0 = (1 - J_f)\rho_f$. Recalling the basic kinematic equation $J = 1 + \varepsilon_{kk}$ (Bonet and Wood, 2008), we have $\delta\rho_f = \rho_f p/K_f$. With this, the variation in fluid mass content is

$$\delta m = \rho_f n \frac{p}{K_f} + \rho_f \delta n \, . \tag{2.37}$$

The variation of fluid volume δV_f of a sample of porous material can be decomposed into two parts, the variation due to compression or dilation of the interstitial fluid δV_{1f}, and the variation in fluid content δV_{2f}. Assuming full saturation, the variation in fluid content is equal to the fluid flow through the boundary. Divided by the representative elementary volume of the porous material V we get

$$\delta n = \delta n_1 + \delta n_2 \, , \tag{2.38}$$

$$\delta n_1 = \frac{\delta V_{1f}}{V} = n\frac{\delta V_{1f}}{V_f} = -n\frac{p}{K_f} \, , \tag{2.39}$$

$$\delta n_2 = \frac{\delta V_{2f}}{V} = \frac{\delta m}{\rho_f} \, , \tag{2.40}$$

where δn_1 is the variation of porosity due to dilation of the interstitial fluid, and δn_2 is the variation of porosity due to variation in fluid content. This is often abbreviated with $\zeta = \delta n_2$.

Now consider an infinitesimal deformation of a porous material. The increment of work per unit volume (strain energy density) is the sum of the strain energy density increment in the solid $\sigma_{ij} d\varepsilon_{ij}$ and fluid phase $dw_f = pdV_f/V = pdn$. For undrained boundary condition, there is no fluid passing the boundary, i.e. $\delta n_2 = 0$. Then, the variation in porosity is $\delta n = \delta n_1 = -np/K_f$, multiplied by a infinitesimal pressure increment $dp = -K_f(\varepsilon_{kk})_f = K_f(dV_f/V_f)$, we find $\delta n dp = -pdn$. Together, we can write the increment of work per unit volume, to deform a porous material, in two equivalent forms:

$$dw = \sigma_{ij} d\varepsilon_{ij} + pdn = \sigma_{ij} d\varepsilon_{ij} - \delta n dp \, . \tag{2.41}$$

Differentiating Eq. 2.41 with respect to strain and pressure, and substituting the stress-strain Eq. 2.25 gives

$$\frac{\partial^2 (dw)}{\partial \varepsilon_{ij} \partial p} = \frac{\partial \sigma_{ij}}{dp} = \frac{-\partial(\delta n)}{\partial \varepsilon_{ij}} = -\alpha \delta_{ij} \, . \tag{2.42}$$

Rearrange Eq. 2.42 and integrate, to get the porosity variation δn. Analogue to volumetric stress response, the porosity variation is a function of dilation and pressure, i.e. $\delta n = \delta n(\varepsilon_{kk}, p)$. Therefore, the integration constant must be a linear function of pressure:

$$\delta n = \alpha \varepsilon_{kk} + bp \, , \quad b \in \mathbb{R} \, . \tag{2.43}$$

Substitute in Eq. 2.37, the variation of mass becomes

$$\delta m = \rho_f n \frac{p}{K_f} + \rho_f (\alpha \varepsilon_{kk} + bp)$$

and rearranging gives

$$\delta m = \rho_f \alpha \varepsilon_{kk} + \rho_f (\frac{n}{K_f} + b) p \, .$$

By choosing

$$b = \frac{\alpha^2}{K_u - K} - \frac{n}{K_f} \,, \tag{2.44}$$

where K_u is the bulk modulus of the undrained response, we finally find

$$\delta m = \rho_f \alpha \varepsilon_{kk} + \frac{\rho_f \alpha^2}{K_u - K} p \,. \tag{2.45}$$

For undrained response, variation of fluid mass content is zero, that is $\delta m = 0$, and we find

$$\alpha p = -(K_u - K)\varepsilon_{kk} \,.$$

Substitution in the stress strain Eq. 2.25 gives

$$\sigma_{ij} = 2G\varepsilon_{ij} + (K - \frac{2G}{3})\varepsilon_{kk}\delta_{ij} + (K_u - K)\varepsilon_{kk}\delta_{ij} \,.$$

After collecting terms, the stress strain equation for the undrained response follows:

$$\sigma_{ij} = 2G\varepsilon_{ij} + (K_u - \frac{2G}{3})\varepsilon_{kk}\delta_{ij} \,. \tag{2.46}$$

Notice that, by appropriate choice of b, Eq. 2.44, pressure is eliminated from the undrained stress strain equation.

Substituting b, Eq. 2.44, in the variation of porosity, Eq. 2.43, gives

$$\delta n = \alpha \varepsilon_{kk} + (\frac{\alpha^2}{K_u - K} - \frac{n}{K_f})p = \frac{\delta m}{\rho_f} - n\frac{p}{K_f} = \delta n_2 + \delta n_1 \,. \tag{2.47}$$

The *variation fluid content* ζ is then

$$\zeta = \delta n_2 = \frac{\delta V_{2f}}{V} = \frac{\delta m}{\rho_f} = \alpha \varepsilon_{kk} + \frac{\alpha^2}{K_u - K} p \,. \tag{2.48}$$

Substituting e_{kk}, Eq. 2.32, in Eq. 2.48 we find

$$\zeta = \frac{\alpha}{K}(\frac{\sigma_{kk}}{3} + \frac{\alpha K_u}{K_u - K} p)$$

or

$$\zeta = \frac{\alpha}{K}(\frac{\sigma_{kk}}{3} + \frac{p}{B}) \,, \tag{2.49}$$

where

$$B = \frac{K_u - K}{\alpha K_u} \tag{2.50}$$

is the *Skempton pore pressure coefficient*.

If no fluid is allowed to leave the sample we refer to *undrained* boundary condition. The variation in fluid content is then zero and with Eq. 2.49 we find

$$B = -\frac{\partial p}{\partial \sigma_{kk}/3}\bigg|_{\zeta=0} \quad . \tag{2.51}$$

That is, Skempton's pore pressure coefficient can be interpreted to be the ratio of change in induced pore pressure to the change in applied stress, for undrained boundary conditions (Skempton, 1954). In a confined compression test, Skempton's pore pressure coefficient can be calculated from measured pore pressure change ∂p and applied confining pressure change $-\partial\sigma_{kk}/3$. From Eq. 2.49 follows $p = -B\sigma_{kk}/3$, and with Eq. 2.48 we find

$$\varepsilon_{kk} = \frac{\sigma_{kk}}{3K_u}\bigg|_{\zeta=0} \quad . \tag{2.52}$$

The undrained bulk modulus K_u can be estimated from confining pressure change and corresponding volume dilation $\varepsilon_{kk} = \delta V/V$.

If fluid is allowed to leave the sample, we refer to *drained* boundary condition. With drained boundary condition, pore pressure is allowed to return to its initial value, that is $p = 0$. With Eq. 2.32b follows

$$\varepsilon_{kk} = \frac{\sigma_{kk}}{3K}\bigg|_{p=0} \quad , \tag{2.53}$$

that is, the drained bulk modulus K can be estimated from applied confining pressure change and corresponding volume dilation. From Eq. 2.48 follows

$$\zeta = \alpha\varepsilon_{kk}\bigg|_{p=0} \quad . \tag{2.54}$$

Recalling that the variation in fluid content can be calculated from the fluid volume passing the boundary $\zeta = \delta V_f/V$, and that volume dilation is $\varepsilon_{kk} = \delta V/V$, the *Biot–Willis coefficient* can be written as

$$\alpha = \frac{\delta V_f}{\delta V}\bigg|_{p=0} \quad . \tag{2.55}$$

This gives a physical interpretation of the Biot–Willis coefficient α as the ratio of the fluid volume passing the boundary, which equals the fluid volume lost in a material element, to the volume change of that element under drained boundary condition. The volume of fluid lost by an element cannot be greater than the total volume change of that element. Therefore, the upper limit of α is one.

2.2.4 Confined Compression Test

Provided sample size is sufficient, a confined compression test can be used for estimation of poroelastic parameters. Typically, a cylindrical plug of the sample is put in a rigid, cylindrical chamber between two end plates. This is placed in a pressure vessel, where a confining pressure can be applied. To test drained boundary condition, end plates with drainage holes are used. For undrained boundary condition impenetrable end plates are used. Refer to Zimmerman et al. (1985) for a description of a device with control of confining and pore pressure. An overview of drained and undrained test conditions is given in Tab. 2.1. Recall that three poroelastic parameters are independent. The fourth parameter can be calculated with Eq. 2.50.

TABLE 2.1: Undrained and drained test overview

Test	Boundary Condition	Measurement	Poroelastic Parameter
drained	$\sigma_{kk}/3$	$\delta V/V$	K
	$p = 0$	$\delta V_f/V$	α
undrained	$\sigma_{kk}/3$	$\delta V/V$	K_u
	$\zeta = 0$	p	B

Examples of confined compression test of articular cartilage, with plug diameter of ca. $5\,\mathrm{mm}$, are found in e.g. Ateshian et al. (1997) and Boschetti et al. (2004). To the best knowledge of the author, confined compression tests for smaller tissue samples were not performed to date. An alternative approach are tests with microneedles, that allow measurements down to cellular and subcellular length scale. For a first overview refer to Sharpe (2008), Chap. 30: Mechanical Testing at the Micro/Nonoscale.

2.2.5 Conservation of Fluid Mass, Darcy's Law and Diffusion Equation

Taking the time derivative of Eq. 2.48, gives

$$\frac{\partial \zeta}{\partial t} = \alpha \frac{\partial \varepsilon_{kk}}{\partial t} + \frac{\alpha^2}{K_u - K} \frac{\partial p}{\partial t} \,. \tag{2.56}$$

Consider a porous media, that occupies the region Ω, and with boundary $\partial\Omega$. With fluid flux vector q, the total volume of fluid that passes through a surface element dA, per unit time, is $q \cdot ndA$, where n is the outward unit normal vector of the surface. The integral over the boundary $\partial\Omega$ gives the total volumetric flux of fluid leaving the region per unit time. The variation in fluid content integrated over the region Ω must be equal to total flux into the region. The surface integral is transformed with the Gauss divergence theorem:

$$\int_\Omega \frac{\partial\zeta}{\partial t} d\Omega = -\int_{\partial\Omega} q \cdot ndA \overset{Gauss}{=} -\int_\Omega \nabla \cdot qd\Omega \,,$$

$$\int_\Omega (\frac{\partial\zeta}{\partial t} + \nabla \cdot q) d\Omega = 0 \,. \tag{2.57}$$

For Eq. 2.57 to be true for the entire region, the integrand must vanish identically, and therefore:

$$\frac{\partial\zeta}{\partial t} + \nabla \cdot q = 0 \,. \tag{2.58}$$

Combining Eq. 2.58 and Eq. 2.56, we find the so called *storage equation*:

$$\alpha \frac{\partial\varepsilon_{kk}}{\partial t} + S \frac{\partial p}{\partial t} = -\nabla \cdot q \,, \tag{2.59}$$

where

$$S = \frac{\alpha^2}{K_u - K} \tag{2.60}$$

is the *storage coefficient*. Combining the storage Eq. 2.59 and Eq. 2.58, we find

$$S = \frac{\partial\zeta}{\partial p}\Bigg|_{\partial\varepsilon_{kk}=0} \,. \tag{2.61}$$

That is, the storage coefficient can be interpreted as the increase of the amount of fluid, per unit volume of porous media, as a result of an increase of pore pressure, at constant volumetric strain (Biot and Willis, 1957).

Consider a fully saturated porous material with isotropic solid phase and bulk modulus K_s. Suppose we apply at the boundary a hydrostatic pressure $p = p_0$. Then, the stress in the solid is $\sigma_{ij} = -p_0\delta_{ij}$. This stress will cause the dilation $\varepsilon_{kk} = \sigma_{kk}/3K_s = -p_0/K_s$, corresponding strain $\varepsilon_{ij} = -p_0\delta_{ij}/3K_s$, and change in porosity $\delta n = -np_0/K_s = n\varepsilon_{kk}$ in the solid phase.

Substituting in Eq. 2.25

$$-p_0\delta_{ij} = 2G\frac{-p_0}{3K_s}\delta_{ij} + (K - \frac{2G}{3})\frac{-p_0}{K_s}\delta_{ij} - \alpha p_0\delta_{ij} \ ,$$

we find an expression for the Biot–Willis coefficient (Biot and Willis, 1957):

$$\alpha = 1 - \frac{K}{K_s} \ , \qquad \textit{with} \qquad \alpha \in [0,1] \ . \tag{2.62}$$

The bulk modulus of the solid phase K_s is higher than the bulk modulus of the porous media with drained boundary condition K. Assuming incompressible solid phase, the upper limit $\alpha = 1$ is observed. Substituting above mentioned hydrostatic boundary pressure conditions in Eq. 2.47, we find

$$n\frac{-p_0}{K_s} = \alpha\frac{-p_0}{K_s} + (\frac{\alpha^2}{K_u - K} - \frac{n}{K_f})p_0 \ ,$$

and an expression for the undrained bulk modulus follows:

$$K_u = K + \frac{\alpha^2 K_s K_f}{nK_s + (\alpha - n)K_f} \ , \qquad \textit{with} \qquad K_u \in [K, \infty) \ . \tag{2.63}$$

Darcy's law is an empirical equation for seepage flow in porous media. It states, that the volume flux q_i of the fluid, relative to the solid, is proportional to the pressure gradient:

$$q_i = -\frac{k}{\mu_f}\frac{\partial p}{\partial x_i} \ , \tag{2.64}$$

where the pore fluid viscosity μ_f has units $Pa\ s$, the *intrinsic permeability* k has units m^2. The volume flux q_i has units m/s and is also called discharge-, seepage- or filter-velocity. According to Cheng and Detournay (1993), 'The intrinsic permeability k is generally a function of the pore geometry. In particular, it is strongly dependent on porosity.'

Conservation of fluid mass requires that the variation in fluid mass content per unit time $\partial(\delta m)/\partial t$ is equal to the net inwards flux across the boundary $-\partial(\rho_f q_i)/\partial x_i$, or

$$\frac{\partial(\rho_f q_i)}{\partial x_i} + \frac{\partial(\delta m)}{\partial t} = 0 \ . \tag{2.65}$$

Substituting in Darcy's Law Eq. 2.64 and mass variation Eq. 2.45, with $\varepsilon_{ii} = 1/2(u_{i,i} + u_{i,i}) = u_{i,i}$, we get the partial differential equation

$$-\frac{k}{\mu_f}p_{,ii} + \alpha\frac{\partial}{\partial t}(u_{i,i} + \frac{\alpha}{K_u - K}p) = 0 \ . \tag{2.66}$$

Consider the equilibrium equation $\sigma_{ij,i} = 0$. Substituting Eq. 2.25, with $\varepsilon_{ij,i} = 1/2(u_{i,ji} + u_{j,ii})$, the partial differential equations for the three coordinate directions (free index j) are

$$(K + \frac{1}{3}G)u_{i,ij} + Gu_{j,ii} - \alpha p_{,j} = 0\,. \tag{2.67}$$

Differentiating with respect to $(.)_{,j}$, and by virtue of Schwarz' theorem, we find

$$(K + \frac{4}{3}G)u_{i,ijj} - \alpha p_{,jj} = 0 \tag{2.68}$$

and after some algebraic manipulations

$$u_{i,ijj} = \frac{K_u - K}{K + (4/3)G}(u_{i,ijj} - \frac{\alpha}{K_u - K}p_{,jj})\,. \tag{2.69}$$

Substituting $p_{,jj}$ from Eq. 2.68 in the partial differential Eq. 2.66, and together with Eq. 2.69, gives

$$c\nabla^2(u_{i,i} + \frac{\alpha}{K_u - K}p) = \frac{\partial}{\partial t}(u_{i,i} + \frac{\alpha}{K_u - K}p)\,, \tag{2.70}$$

where c is the *diffusion coefficient*

$$c = \frac{k(K_u - K)(K + 4G/3)}{\mu_f \alpha^2 (K_u + 4G/3)}\,. \tag{2.71}$$

Observe that the terms in brackets on left and right hand side of the partial differential Eq. 2.70 are identical. It has the form of a diffusion equation. According to Eq. 2.45, the terms in brackets multiplied by $\rho_f \alpha$ are the variation in fluid mass content. That is, Eq. 2.70 is a *diffusion equation* in terms of variation in fluid mass content:

$$c\nabla^2(\delta m) = \frac{\partial}{\partial t}(\delta m)\,. \tag{2.72}$$

After some algebraic manipulations, the diffusion equation can also be written in terms of pore pressure (Zimmerman (2000)):

$$(\frac{k}{\mu_f}\frac{K_u - K}{\alpha^2})\nabla^2 p - (\frac{K_u - K}{\alpha})\frac{\partial \varepsilon_{kk}}{\partial t} = \frac{\partial p}{\partial t}\,. \tag{2.73}$$

Note that the diffusion equation in terms of pressure, Eq. 2.73, has a source term, which couples the rate of change in dilation $\partial \varepsilon_{kk}/\partial t$.

2.2.6 Some Remarks on the Numerical Implementation

Early contributions to the numerical implementation of poroelasticity with the finite element method are, for example, from Sandhu and Wilson (1969), Christian (1968) and Ghaboussi and Wilson (1973). For an introduction refer to the textbook of Zienkiewicz et al. (2005), Chap. 18.3: Soil-pore fluid interaction. Based on the variational formulation of the stress-strain Eq. 2.25 and the storage Eq. 2.59, coupled equations in terms of the nodal unknowns displacement and pore pressure are derived.

Later contributions based on bipahsic mixture theory, like Levenston et al. (1998) and Ehlers and Markert (2001), assumed incompressible solid and fluid phases. With this assumption we have $\alpha = 1$, $K = K_u$ and $S = 0$. Therefore, in the storage Eq. 2.59, the time derivative of pressure term is zero, and the corresponding term in Eq. 18.75 in the textbook of Zienkiewicz et al. (2005) can be neglected.

As a final remark, observing the analogy of the poroelastic diffusion Eq. 2.73 and the heat diffusion equation, one could solve poroelastic problems with procedures implemented for thermal analysis (Zimmerman, 2000; Capone, 2010).

2.3 Viscoelasticity

2.3.1 Introduction

According to the definition of Pandolfi (2012), a continuum is said to be viscoelastic if it exhibits elastic and viscous material behaviour at the same time, that is, if its state of stress depends on deformation, rate of deformation and temperature.

Various phenomenological models have been proposed. For an introduction into the theory of viscoelasticity refer to the textbooks of e.g. Findley and Lai (1976), Christensen (1982) and Severino and Guillermo (2012), as well as the articles of Simo (1987) and Reese and Govindjee (1998).

Here, the Generalised Maxwell Model for isothermal condition is described, following the paper of Kaliske and Rothert (1997).

2.3.2 Phenomenological Viscoelastic Model

One Dimensional Linear Viscoelasticity

A one dimensional viscoelastic behaviour can be modelled with the basic constitutive rheological elements of an elastic spring, called *Hooke-element* and a viscous damper, called *Newton-element*. Hooke's law states that elastic stress σ_e is proportional to elastic strain ε_e:

$$\sigma_e = \mu \varepsilon_e \,, \tag{2.74}$$

where the proportionality factor is the spring stiffness μ. Assuming viscous response is governed by a Newtonian fluid, the viscous stress σ_v is proportional to the strain rate $\dot{\varepsilon_v}$:

$$\sigma_v = \eta \dot{\varepsilon_v} \,, \tag{2.75}$$

where the proportionality factor is the viscosity η. The connection in series of a Hooke-element and a Newton-element is called *Maxwell-element* (Fig. 2.2). The total strain of the Maxwell-element ε, is the sum of the elastic and viscous strain

$$\varepsilon = \varepsilon_e + \varepsilon_v \,, \tag{2.76}$$

whereas the stress in the Hooke-element and the Newton-element are identical

$$\sigma = \mu \varepsilon_e = \eta \dot{\varepsilon_v} \,. \tag{2.77}$$

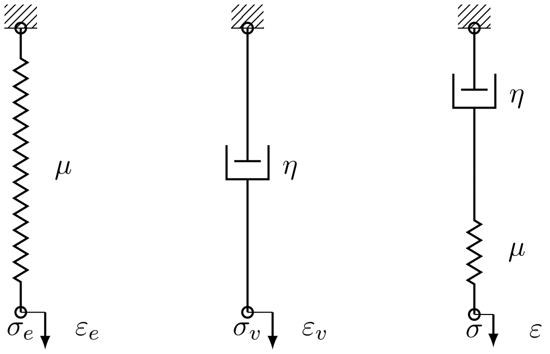

FIGURE 2.2: From left to right: Hooke-, Newton- and Maxwell-element.

Taking the time derivative of Eq. 2.76 and substituting Eq. 2.77 gives the differential equation of the Maxwell-element:

$$\dot{\varepsilon} = \frac{\dot{\sigma}}{\mu} + \frac{\sigma}{\eta} \,. \tag{2.78}$$

Consider the response of the Maxwell-element to a relaxation test, where strain input changes from zero to ε_0 at $t_0 = 0$. With the unit step function $u(\,)$, the strain input for the relaxation test is $\varepsilon(t) = \varepsilon_0 u(t - t_0)$. With the initial condition $\sigma_0 = \mu\varepsilon_0$, the solution of Eq. 2.78 is

$$\sigma(t) = \mu\varepsilon_0 e^{-t/\tau} \,, \tag{2.79}$$

where $\tau = \eta/\mu$ is the *time constant* of the Maxwell-element. Dividing Eq. 2.79 by ε_0 gives the *relaxation function*

$$\Gamma(t) := \frac{\sigma(t)}{\varepsilon_0} = \mu e^{-t/\tau} \,, \tag{2.80}$$

which is characteristic for the viscoelastic material. The response of a Maxwell-element to a relaxation test (Eq. 2.79) in normalised form (divided by $\mu\varepsilon_0$) is plotted in Fig. 2.3. The initial value is $\sigma(t = 0)/\mu\varepsilon_0 = 1$. After $t = \tau$ stress has reduced to $36.8\,\%$ and after $t = 4\tau$ stress has reduced to $1.83\,\%$. For long times stress reduces to zero, $\sigma(t \to \infty) = 0$. The slope of the curve at $t/\tau = 0$ is 1 and the tangent at $t = 0$ intercepts the time axis at $t = \tau$. This property can be useful when evaluating measured relaxation curves.

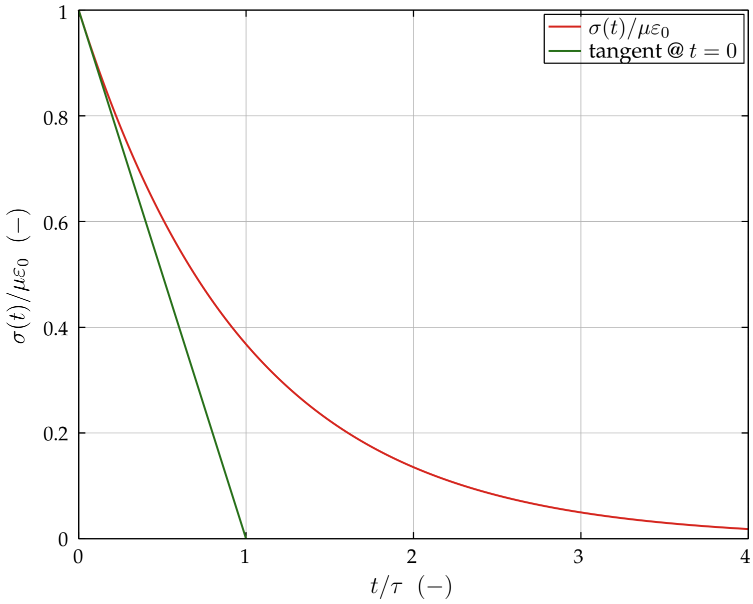

FIGURE 2.3: Relaxation test of a Maxwell-element.

We now consider a generalised Maxwell-element (Fig. 2.4), where a finite number of Maxwell-elements $j = 1, .., N$ are connected in parallel to a single Hooke-element. The response of a generalised Maxwell-element to a relaxation test is obtained by adding the contribution of the parallel elements

$$\sigma(t) = \mu_0 \varepsilon_0 + \sum_{j=1}^{N} \mu_j \varepsilon_0 e^{-t/\tau_j} \tag{2.81}$$

and the corresponding relaxation function is

$$\Gamma(t) = \mu_0 + \sum_{j=1}^{N} \mu_j e^{-t/\tau_j} \ . \tag{2.82}$$

Dividing Eq. 2.82 by μ_0 gives relaxation function in normalised form

$$\gamma(t) := \frac{\Gamma(t)}{\mu_0} = 1 + \sum_{j=1}^{N} \gamma_j e^{-t/\tau_j} \ , \tag{2.83}$$

where $\gamma_j = \mu_j/\mu_0$ and $\tau_j = \mu_j/\eta_j$.

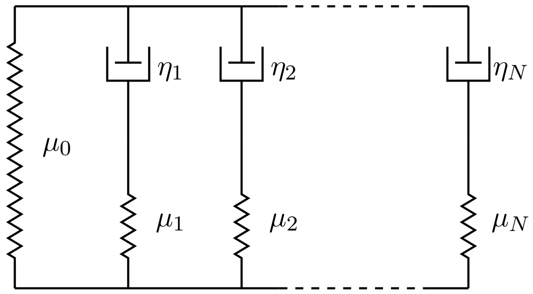

FIGURE 2.4: Generalised Maxwell-element.

We now consider the response of a generalised Maxwell-element to relaxation test with $i = 1, .., M$ incremental strain inputs $\delta\varepsilon_i$ at time t_i:

$$\varepsilon(t) = \sum_{i=1}^{M} \delta\varepsilon_i \, u(t - t_i) \, . \tag{2.84}$$

The response of a material to a given load is, according to the Boltzmann superposition principle[2], independent of the response of the material to any previous loads already applied to the material. As a consequence, the response to each incremental load $\delta\varepsilon_i$ is independent of those due to the previous incremental loads, and the response to the complete load history equals the sum of the individual responses:

$$\sigma(t) = \sum_{i=1}^{M} \sigma_i(t - t_i) = \sum_{i=1}^{M} \Gamma(t - t_i) \, \delta\varepsilon_i \, u(t - t_i) \, . \tag{2.85}$$

In the limiting case of infinitesimal strain input $d\varepsilon$, the total stress is given by the integral:

$$\sigma(t) = \int_0^t \Gamma(t - t_i) \, u(t - t_i) \, d\varepsilon \, . \tag{2.86}$$

Provided the strain input history is differentiable with respect to time, the integral reduces to

$$\sigma(t) = \int_0^t \Gamma(t - s) \, \frac{\partial \varepsilon}{\partial s} \, ds \, , \tag{2.87}$$

where

$$\Gamma(t - s) = \mu_0 + \sum_{j=1}^{N} \mu_j e^{-(t-s)/\tau_j} \, . \tag{2.88}$$

---

[2] Boltzmann (1874)

Substituting Eq. 2.88 into Eq. 2.87 and dividing the integral into the elastic and viscoelastic part gives

$$\begin{aligned}\sigma(t) &= \int_0^t \mu_0 \frac{\partial \varepsilon}{\partial s}\, ds + \int_0^t \sum_{j=1}^{N} \mu_j e^{-(t-s)/\tau_j} \frac{\partial \varepsilon}{\partial s}\, ds \\ &= \mu_0\, \varepsilon(t) + \sum_{j=1}^{N} \int_0^t \mu_j e^{-(t-s)/\tau_j} \frac{\partial \varepsilon}{\partial s}\, ds \\ &= \sigma_0(t) + \sum_{j=1}^{N} h_j(t)\,.\end{aligned} \tag{2.89}$$

The stress response is composed of the elastic stress component

$$\sigma_0(t) = \mu_0 \varepsilon(t) \tag{2.90}$$

and the sum of the internal stress variables $h_j(t)$, which represent the response of the N Maxwell-elements

$$h_j(t) = \int_0^t \mu_j e^{-(t-s)/\tau_j} \frac{\partial \varepsilon(s)}{\partial s}\, ds\,. \tag{2.91}$$

Substituting Eq. 2.90 in Eq. 2.91 gives

$$h_j(t) = \int_0^t \gamma_j e^{-(t-s)/\tau_j} \frac{\partial \sigma_0(s)}{\partial s}\, ds\,. \tag{2.92}$$

Analogue to Eq. 2.78 the differential equation of Maxwell-element j, corresponding to Eq. 2.92 is

$$\dot{h}_j + \frac{1}{\tau_j} h_j = \gamma_j \dot{\sigma}_0\,. \tag{2.93}$$

Numerical integration of Eq. 2.92 is accomplished by a recurrence relation similarly proposed by Hermann and Peterson (1968) and Taylor et al. (1970). For the time interval $[t_n, t_{n+1}]$ we define the time step $\Delta t = t_{n+1} - t_n$ and write the exponential term $e^{-t_{n+1}/\tau_j} = e^{-(t_n+\Delta t)/\tau_j} = e^{-t_n/\tau_j} e^{-\Delta t/\tau_j}$. Integration of the deformation history is split into the interval $[0, t_n]$, where the integrated result at t_n is known and the present interval $[t_n, t_{n+1}]$, where the result at t_{n+1} is unknown. Substituting into Eq. 2.92 gives

$$\begin{aligned} h_j(t_{n+1}) &= \gamma_j \int_0^{t_{n+1}} e^{-(t_{n+1}-s)/\tau_j} \, \frac{\partial \sigma_0(s)}{\partial s} \, ds \\ &= \gamma_j e^{-\Delta t/\tau_j} \int_0^{t_n} e^{-(t_n-s)/\tau_j} \, \frac{\partial \sigma_0(s)}{\partial s} \, ds + \gamma_j \int_{t_n}^{t_{n+1}} e^{-(t_{n+1}-s)/\tau_j} \, \frac{\partial \sigma_0(s)}{\partial s} \, ds \\ &= e^{-\Delta t/\tau_j} h_j(t_n) + \gamma_j \int_{t_n}^{t_{n+1}} e^{-(t_{n+1}-s)/\tau_j} \, \frac{\partial \sigma_0(s)}{\partial s} \, ds \, . \end{aligned} \tag{2.94}$$

Up to this point no numerical approximation was involved and the recursive equation provides the exact value of the current internal stress variable $h_j(t_{n+1})$. The derivative in the integral is written in discrete form. For ease of notation we use superscript n for t_n:

$$\frac{\partial \sigma_0(s)}{\partial s} = \lim_{\Delta s \to 0} \frac{\Delta \sigma_0(s)}{\Delta s} = \lim_{\Delta t \to 0} \frac{\sigma_0^{n+1} - \sigma_0^n}{\Delta t} \, . \tag{2.95}$$

Substituted in Eq. 2.94

$$h_j^{n+1} = e^{-\Delta t/\tau_j} h_j^n + \gamma_j \int_{t_n}^{t_{n+1}} e^{-(t_{n+1}-s)/\tau_j} \, \frac{\sigma_0^{n+1} - \sigma_0^n}{\Delta t} \, ds \tag{2.96}$$

and integration provides the recursive equation for the internal stress variable

$$h_j^{n+1} = e^{-\Delta t/\tau_j} h_j^n + \gamma_j \frac{1 - e^{-\Delta t/\tau_j}}{\Delta t/\tau_j} \, [\sigma_0^{n+1} - \sigma_0^n] \, . \tag{2.97}$$

Then, the current stress at t_{n+1} is

$$\sigma^{n+1} = \mu_0 \varepsilon^{n+1} + \sum_{j=1}^{N} h_j^{n+1} \tag{2.98}$$

and the viscoelastic stiffness is

$$C^{n+1} = \frac{\partial \sigma^{n+1}}{\partial \varepsilon^{n+1}} = \mu_0 (1 + \sum_{j=1}^{N} \gamma_j \frac{1 - e^{-\Delta t/\tau_j}}{\Delta t/\tau_j}) \, . \tag{2.99}$$

For constant stiffness μ_0 and fixed time step Δt the viscoelastic stiffness is constant (Eq. 2.99). For the recursive estimation of the internal stress variable h_j^{n+1} in Eq. 2.97 knowledge of the previous stress state σ_0^n and h_j^n, with

$j = 1, .., N$ is necessary. These variables are available from the previous time step t_n. The stress at the Hooke-element σ_0^{n+1} can be estimated from the strain increment of the current step. 'The shown strain-driven integration algorithm is unconditionally stable for small and large time steps and it is second order accurate' (Kaliske and Rothert, 1997).

Finite Viscoelasticity

In this section we extend the viscoelastic model to the three dimensional case and finite strain. 'Experimental investigations have shown that in many cases viscoelastic behaviour is mainly related to the isochoric part of the deformation. Thus, the volume dilation is considered as being purely elastic. In contrast to total viscoelasticity introduced before, a volumetric and isochoric split of the stresses is required to formulate separate material properties' (Kaliske and Rothert, 1997). Based on a local multiplicative decomposition of the deformation gradient into volume preserving and dilational part, which to the best of knowledge of the author goes back to Flory (1961), stress tensor is split into a deviatoric and volumetric part. For ease of notation we use bold face letters for second order tensors in Eq. 2.27, with $tr()$ denoting the trace operator and $\mathbf{I}$ the second order unit tensor:

$$\boldsymbol{\sigma} = \boldsymbol{\sigma}' + \frac{1}{3} tr(\boldsymbol{\sigma})\, \mathbf{I}\,. \tag{2.100}$$

The first part $\boldsymbol{\sigma}'$ is the deviatoric stress tensor, which involves the volume preserving (isochoric) response. The second part $1/3tr(\boldsymbol{\sigma})\, \mathbf{I}$ is the volumetric stress tensor, also called spherical or hydrostatic strees tensor. It involves dilational volumetric response conserving the shape.

Isochoric finite viscoelasticity is associated to the deviatoric response. In analogy Eq. 2.98 and Eq. 2.97 are written for the deviatoric response

$$\boldsymbol{\sigma}'^{\,n+1} = \boldsymbol{\sigma}_0'^{\,n+1} + \sum_{j=1}^{N} \mathbf{H}_j'^{\,n+1}\,, \tag{2.101}$$

$$\mathbf{H}_j'^{\,n+1} = e^{-\Delta t/\tau_j} \mathbf{H}_j'^{\,n} + \gamma_j \frac{1 - e^{-\Delta t/\tau_j}}{\Delta t/\tau_j} \left[\boldsymbol{\sigma}_0'^{\,n+1} - \boldsymbol{\sigma}_0'^{\,n}\right] \tag{2.102}$$

and Eq. 2.99 becomes

$$\mathbb{C}^{v\,n+1} = \mathbb{C}_{vol}^{e\,n+1} + \mathbb{C}_{iso}^{e\,n+1}\left(1 + \sum_{j=1}^{N} \gamma_j \frac{1 - e^{-\Delta t/\tau_j}}{\Delta t/\tau_j}\right). \tag{2.103}$$

The forth order viscoelastic stiffness tensor $\mathbb{C}^v$ contains a volumetric term $\mathbb{C}^e_{vol}$ and an isochoric term $\mathbb{C}^e_{iso}$ multiplied by a constant. The elastic stiffness tensor, analogue to μ_0 of linear viscoelasticity, is $\mathbb{C}^e = \mathbb{C}^e_{vol} + \mathbb{C}^e_{iso}$. For hyperelastic materials the stiffness tensors can be obtained from the appropriate strain energy density function (see e.g. Bonet and Wood (2008)). Again, for the recursive estimation of the internal stress variable $\mathbf{H}'^{n+1}_j$ in Eq. 2.102 knowledge of the previous stress state $\boldsymbol{\sigma}'^{n}_0$ and $\mathbf{H}'^{n}_j$, with $j = 1, .., N$ is necessary. These variables are available from the previous time step t_n.

Chapter 3

Dimensionless Analysis

3.1 Dimensionless Analysis and the Péclet Number

Consider the deformation of a representative control volume of a porous material with fluid filled, interconnected pores. If the material behaves viscoelastic, there is a viscous interaction between the fluid and the porous material, however the fluid remains at its location. That is, there is no flow of the interstitial fluid across the boundary of the control volume. On the other hand, if the material behaves poroelastic, a net flow across the boundary of the control volume is admissible, which could be due to a pressure gradient induced flow of the interstitial fluid through the porous material.

Dimensionless numbers are used to characterise physical processes. In the context of mass transfer[1] in a continuum, the dimensionless number, defined by the ratio of advection to diffusion mass flux, is called *Péclet* number[2]. The advection mass flux, i.e. the mass per time passing the boundary due to bulk fluid motion with *velocity* v, is $\rho_f\, v$, where ρ_f is the density of the fluid. The diffusion mass flux is $D \nabla \rho_f$, where D is the *mass diffusion coefficient* (units: m^2/s). Upon replacement of the gradient by a *characteristic length* L of the experiment, the Péclet number is

$$Pe = \frac{L\, v}{D}\,. \tag{3.1}$$

From the definition it is clear that for $Pe \gg 1$ advection mass flux is dominant and for $Pe \ll 1$ diffusion mass flux is dominant.

In the context of poroelasticity, advection mass flux is due to bulk fluid motion forced by a pressure gradient, usually described by *Dray's Law*. The diffusion mass flux is due to a mass density gradient of the interstitial fluid and usually described by *Fick's Law*. For a viscoelastic material, an important characteristic describing the relaxation behaviour is the time constant τ_v. The test

---

[1] For an introduction to mass transfer refer to textbooks like Incropera and DeWitt (1985).

[2] For an analogue definition of the Péclet number in heat transfer refer to Eckert (1949).

time t is made dimensionless by dividing through the time constant τ_v, i.e. the *normalised time* is t/τ_v. If in Eq. 3.1 velocity is replaced by $v = L/t$, the product of Péclet number and normalised time becomes

$$Pe \cdot \frac{t}{\tau_v} = \frac{L^2}{D\,\tau_v} = \frac{L^2}{L_d^2}\,. \tag{3.2}$$

This is again a dimensionless number, defined as the quotient of the characteristic length L and the material specific diffusion length L_d, squared. For a given test $L^2/D\,\tau_v$ is constant, and characterises the *dimensionless length* $(L/L_d)^2$ of the experimental setup. The material specific *diffusion length*

$$L_d = \sqrt{D\,\tau_v} \tag{3.3}$$

can be interpreted as the distance of mass transfer due to diffusion, within the time characteristic for viscoelastic relaxation.

For a given characteristic length L of the experiment, the diffusion time is $t_d \propto L^2/D$ and the advection time is $t_a \propto L/v$. With that, the Péclet number

$$Pe = \frac{L\,v}{D} = \frac{L^2}{D}\frac{v}{L} = \frac{t_d}{t_a} \tag{3.4}$$

can be interpreted as the ratio of diffusion time and advection time, which can be considered as the *dimensionless time* of the experimental setup. If $t_d \gg t_a$ advection mass flux is dominant, and if $t_d \ll t_a$ diffusion mass flux is dominant.

The upper plot of Fig. 3.1 shows the Péclet number and the middle plot shows $L^2/D\tau_v$ versus normalised time on a double logarithmic scale. A green line was plotted for $Pe = 1$ and cyan lines were plotted for $Pe = 0.1$ and $Pe = 10$. The lower plot shows a exponential decay function (blue line) on semilogarithmic scale.

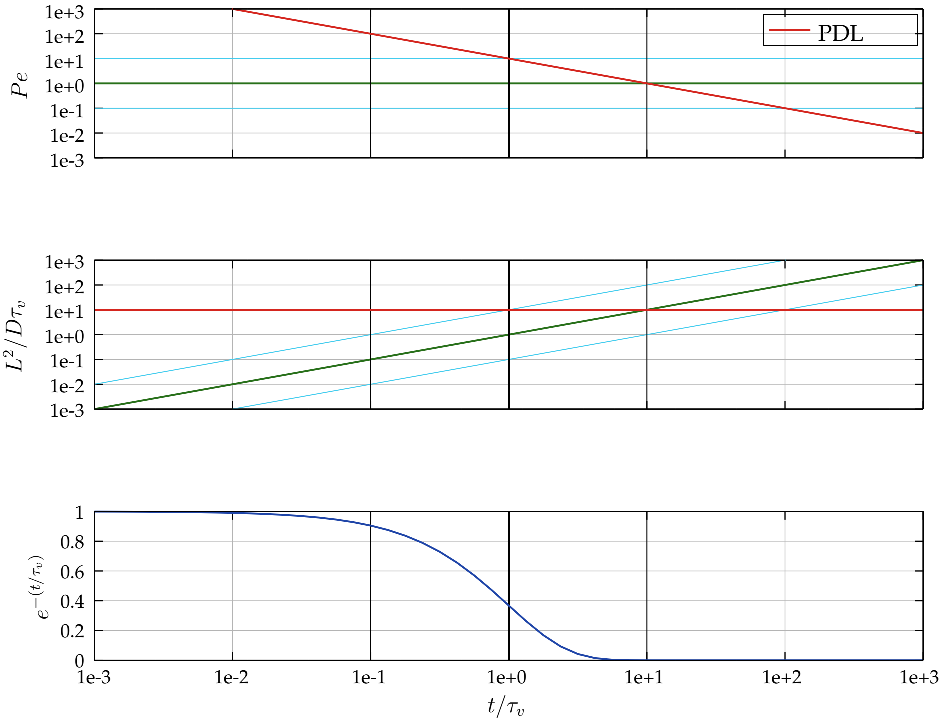

FIGURE 3.1: Plot Péclet number, normalised length and exponential decay function versus normalised time. The red line is for the PDL in situ with $L = 0.1\,\mathrm{mm}$, $D = 1 \cdot 10^{-10}\,\mathrm{m^2\,s^{-1}}$ and $\tau_v = 10\,\mathrm{s}$. The green line is $Pe = 1$, cyan lines are for $Pe = 0.1$ and $Pe = 10$.

3.2 Application to the Periodontium and Discussion

Consider an in situ test of the periodontium. In the presence of an external load on the tooth, part of the interstitial fluid is likely to move to the alveolar bone. Therefore, an obvious choice for the characteristic length is the width of the periodontal ligament, which is in the order of magnitude of $0.1\,\mathrm{mm}$. Based on experiments with cells and tissue tested with atomic force microscopes and nanoindentation by Charras et al. (2009) and Rosenbluth et al. (2008), the mass diffusion coefficient D is in the order of magnitude of $1 \cdot 10^{-10}\,\mathrm{m^2\,s^{-1}}$. The time constant τ_v is in the order of magnitude of $10\,\mathrm{s}$ (Toms et al., 2002). With these figures, we can estimate the constant $L^2/D\tau_v$ and find from Eq. 3.2 the Péclet number as a function of inverse normalised time:

$$Pe = \frac{L^2}{D\tau_v}\left(\frac{t}{\tau_v}\right)^{-1}. \tag{3.5}$$

Figure 3.1 shows a plot of Eq. 3.5 (red line) with above mentioned constants for the PDL in situ. For $t/\tau_v \ll 10^{-1}$ viscoelastic relaxation is marginal and advection, i.e. poroelastic behaviour, is dominant. For $t/\tau_v > 10^{-1}$ viscoelastic relaxation is noticeable ($e^{-0.1} = 0.905$), at $t/\tau_v = 1$ viscoelastic relaxation is in progress ($e^{-1} = 0.368$) and at $t/\tau_v = 10$ viscoelastic relaxation is practically completed ($e^{-10} = 0.000$). Between $t/\tau_v = 1$ and $t/\tau_v > 10^2$ transition from advection to diffusion is observed and for $t/\tau_v > 10^2$ diffusion mass flux becomes dominant.

Concluding, for an in situ relaxation test of the periodontium, it is anticipated that poroelastic behaviour will be observed during the initial phase of the test, and poroelastic behaviour will gradually cease between $t/\tau_v = 1$ and $t/\tau_v = 10$. Further, viscoelastic behaviour is anticipated to be noticeable after about $t/\tau_v = 10^{-2}$. Taking into account that in practice several time constant for viscoelastic relaxation were reported (e.g. Toms et al. (2002)), it is anticipated that, after the initial phase, viscoelastic behaviour will be observed throughout the test.

Chapter 4

Curve Fit of Test Data

4.1 Curve Fit - In Vitro Test of Papadopoulou

4.1.1 Test Data

For the in vitro measurements done by Papadopoulou et al. (2013), actuator displacement $x(t)$ was input as a function of time t. The displacement of the actuator rose at constant speed, $v_{ramp} = d_{ramp}/t_{ramp}$, between $t = 0$ and the ramp rise time $t = t_{ramp}$, to the maximum actuator displacement d_{ramp}. Thereafter, the actuator displacement stayed constant at d_{ramp}, until the measurement was finished at time t_{max} :

$$x = x(t) = \begin{cases} v_{ramp} \cdot t, & 0 \leq t \leq t_{ramp} \\ d_{ramp}, & t_{ramp} < t \leq t_{max} \end{cases} . \tag{4.1}$$

An overview of the measurements done is shown in Tab. 4.1. The first column list the test number. In the following three columns, the time of day when the test was started t_{start}, the ramp rise time t_{ramp}, and maximum actuator displacement d_{ramp}, as encoded in the measurement log file name, are listed. Subsequently, it was assumed that t_{Fmax} is the actual ramp rise time of the actuator. The next two columns provide the measured peak force F_{max}, and the time when this peak force occurred t_{Fmax}. Actuator force values were recorded at a sample interval t_{sample}.

Observe that for test number 13, 15, 16, 17 and 18 the ramp time encoded in the file name t_{ramp}, deviates considerably form the peak force time t_{Fmax}, recorded in the measurement protocol. Apparently, this was due to an issue with the actuator displacement controller. Exemplary, in Fig. 4.1 test number 1, 2, 11 and 12 are plotted. The force curve of test No. 1 shows a kink at ca. 200 seconds, even though there was no change of the actuator input. Due to these peculiarities, test number 1, 13, 15, 16, 17 and 18 were discarded from curve fit.

Consider Fig. 4.1, small jumps in the measured force are observed. Due to scaling of the force axis, this is clearly visible for tests with lower peak force, in particular test number 11. For test 11 and 12, in response to actuator displacement until ramp rise time, respectively $60\,\mathrm{s}$ and $120\,\mathrm{s}$, a progressive force characteristic is observed. For all tests, after the maximum force is reached at ramp rise time, a force decay with decreasing slope is observed.

TABLE 4.1: Papadopoulou et al. (2013) test – overview for specimen 14.

test -	t_{start} hh:mm	t_{ramp} s	d_{ramp} mm	t_{sample} s	t_{max} s	t_{Fmax} s	F_{max} N	t_{rest} s
1	10:59	5	0.1	0.2	605.1	5.4	2.5	-
2	11:20	5	0.2	0.2	605.1	6.4	9.5	655
3	12:21	10	0.1	0.2	610.1	10.6	1.6	3055
4	12:36	10	0.2	0.2	610.1	10.4	8.1	290
5	12:54	20	0.1	0.2	620.1	21.0	1.0	470
6	13:14	20	0.2	0.2	620.1	20.6	6.7	580
7	13:31	30	0.1	0.2	630.1	30.6	0.9	400
8	13:49	30	0.2	0.2	630.1	30.8	5.9	450
9	14:07	60	0.1	0.2	660.2	60.5	0.7	450
10	14:30	60	0.2	0.2	660.1	61.9	4.6	720
11	14:50	120	0.1	0.5	720.0	120.2	0.5	540
12	15:12	120	0.2	0.5	720.0	123.2	4.3	600
13	15:32	300	0.1	0.5	900.3	191.3	0.4	480
14	15:57	300	0.2	0.5	900.3	305.4	3.8	600
15	16:30	450	0.1	0.5	1050.0	191.8	0.4	1080
16	17:11	450	0.2	0.5	1050.0	391.6	3.0	1410
17	17:36	600	0.1	0.5	1200.2	193.8	0.3	450
18	18:01	600	0.2	0.5	1200.2	387.1	3.2	300

4.1.2 Model Function

A well known method for solving partial differential equations is separation of variables. Analogue, the model function for actuator force $Y(x,t,p)$ is assumed to be the product of a function of actuator displacement $F(x,p_F)$ and a function of time $G(t,p_G)$, with time $t \in [0, t_{max}]$, actuator displacement $x(t)$ and parameters $p = [p_F, p_G]$ of F and G:

$$Y(t,p) = F(x(t),p_F) \cdot G(t,p_G)\,. \tag{4.2}$$

The Boltzmann superposition principle is employed. That is, response to the complete load history is the sum of the individual responses due to $i =$

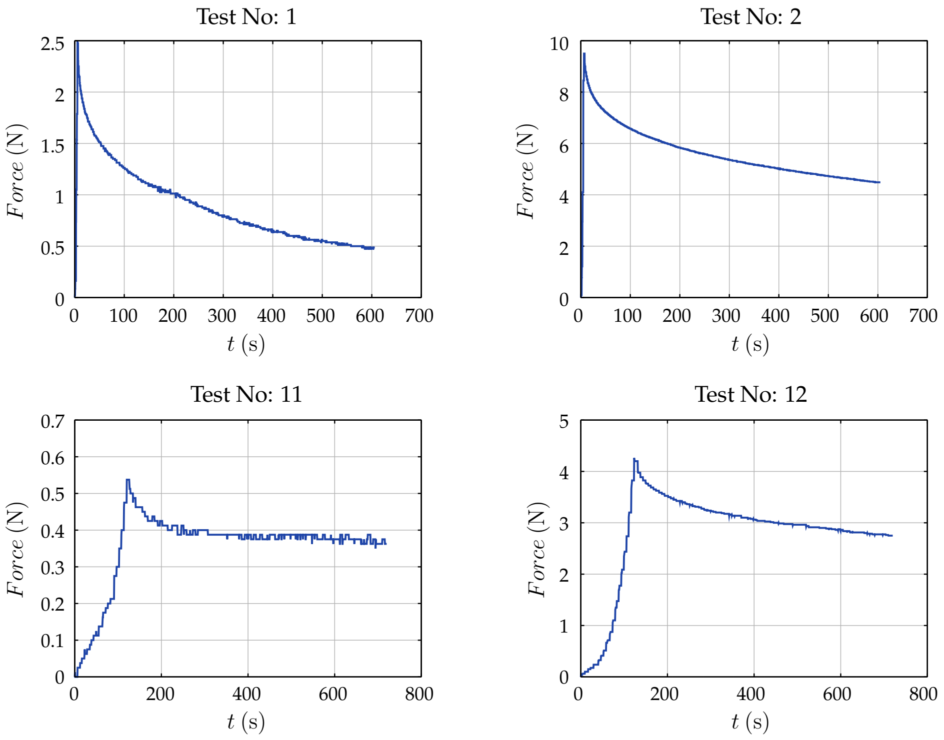

FIGURE 4.1: Plot of test No. 1, 2, 11 and 12.

$1, .., M$ incremental displacement inputs δx_i at time t_i, with actuator displacement defined in Eq. 4.1 approximated by $x(t) = \sum_{i=1}^{M} \delta x_i \, u(t - t_i)$, where u is the unit step (Heaviside) function.

Consider the plot to test data, Fig. 4.1. Force increases with actuator displacement $x(t)$ and a progressive characteristic is observed. This could be approximated by a polynomial, with constant term set to zero in order to satisfy $F(x = 0) = 0$. A first curve fit was done with a polynomial of second order. The polynomial order was successively increased to improve approximation of the progressive characteristic. It was observed that the coefficients of the power series terms changed sign and decreased. This led to the idea, recalling the power series of e^x, that this could be described by an expression of the form $e^x - 1$, which requires the estimation of two parameters instead of n parameters, for a polynomial of order n without constant term. Concluding, the proposed equation for $F(x, p_F)$, with parameters $p_F = \{p_1, p_2\}$ is

$$F(x, p_F) = p_1(e^{p_2 \cdot x} - 1) \, . \tag{4.3}$$

Sensitivity of Eq. 4.3 to parameter changes p_1 and p_2 are plotted in Fig. 4.2

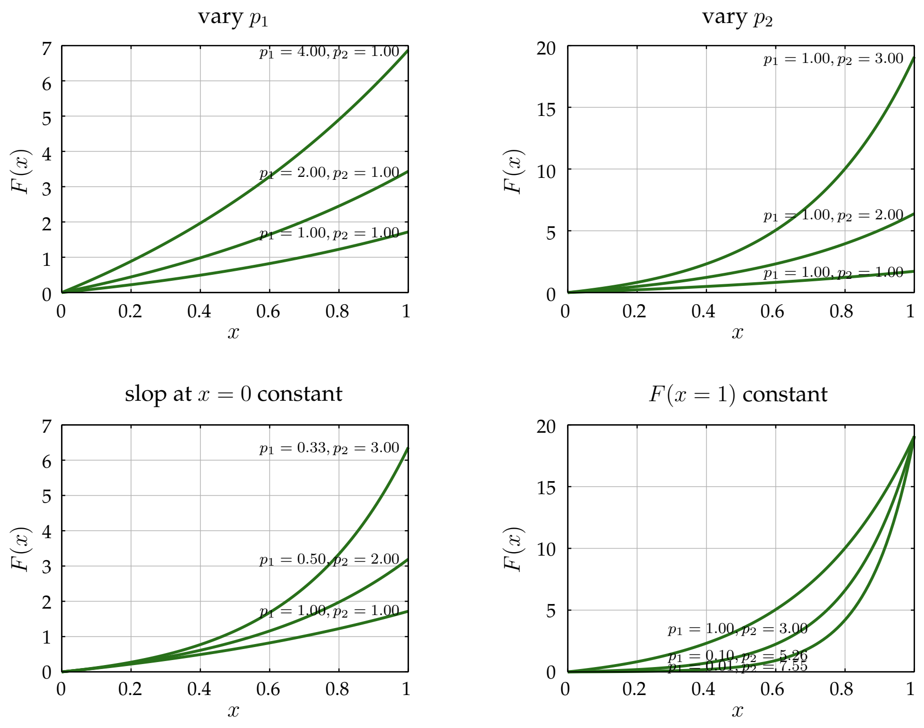

FIGURE 4.2: Sensitivity to parameter changes of Eq. 4.3, the model function for displacement $F(x, p_F) = p_1(e^{p_2 \cdot x} - 1)$.

upper left and right. Observe that changes of the parameters p_1 or p_2 effects both, initial slope at $x = 0$ and the value of F at e.g. $x = 1$.

Consider the derivative of F with respect to x. By changing the factor in front of the bracket from p_1 to p_1/p_2, the gradient at $x = 0$ becomes independent of p_2. Than, for a fixed value of p_1 we can choose p_2 to fit F at a selected point, e.g. $x = d_{ramp}$, to a desired value, without altering the initial slope at $x = 0$. Therefore Eq. 4.3 is changed to

$$F(x, p_F) = \frac{p_1}{p_2}(e^{p_2 \cdot x} - 1)\ . \tag{4.4}$$

Observe that Eq. 4.4 is analogue to the equation proposed by Fung (1967)[1] for the quasi static one-dimensional passive response of soft tissue in integrated form.

---

[1] $\frac{\partial T(\lambda)}{\partial \lambda} = E + \beta T(\lambda)$ with T traction, λ stretch, E Young's modulus, β a constant.

In order to keep $F(x = d_{ramp})$ constant for varying initial slope, with $p_1^{new} = c\, p_1$ and constant $c \in \mathbb{R}^+ \setminus 0$, we find p_2^{new} from the nonlinear equation

$$p_2^{new}\,(e^{p_2 d_{ramp}} \;-\; 1) - c\, p_2\,(e^{p_2^{new} d_{ramp}} \;-\; 1) = 0\,. \tag{4.5}$$

With this in mind, we can use p_2 and p_1 to curve fit the model function of the two ramp displacements 0.2 and 0.1 mm independently, provided the parameters of $G(t, p_G)$ do not depend on ramp displacement. This means, we can first fit the model function to ramp displacement 0.2 mm tests and than find constant c, with $p_1^{new} = c\, p_1$ and p_2^{new} adapted according to Eq. 4.5, that best fits the ramp displacement 0.1 mm test data, without altering the response to ramp displacement 0.2 mm input for times larger than the ramp rise time.

Consider again the plot of test data, Fig. 4.1. For the response right of the peak force point, i.e. where the actuator displacement input remains constant, a decay of the force with time is observed and the force appears to converge against an equilibrium value. This suggests to define $G(t, p_G)$ as the sum of an exponential decay function and a constant term, to cover the steady state response. The structure of $G(t, p_G)$ was defined analogue to a viscoelastic stress relaxation function. According to ABAQUS (2016), Analysis User's Guide, Chap. 19.7.1, 'The number of terms in the Prony series should be typically not more than the number of logarithmic "decades" spanned by the test data. The number of logarithmic "decades" is defined as $n = lg(t_{max}/t_{min})$, where t_{max} and t_{min} are the maximum and minimum time in the test data, respectively.' With the figures from Tab. 4.1 we estimate $n = lg(1200/0.5) = 3.38$. Therefore three exponential terms, with time constants $\tau_i = 1/p_j;\ i, j \in \{(1,5),(2,7),(3,9)\}$ are used and the proposed equation for $G(t, p_G)$, with parameters $p_G = \{p_3, ..., p_9\}$ is

$$G(t, p_G) = p_3 + p_4 e^{-p_5 \cdot t} + p_6 e^{-p_7 \cdot t} + p_8 e^{-p_9 \cdot t}\,. \tag{4.6}$$

Collecting terms, the proposed model function is

$$\begin{aligned} Y(t,p) &= F(x(t), p_F) \cdot G(t, p_G)\,, \\ F(x(t), p_F) &= \frac{p_1}{p_2}(e^{p_2 \cdot x} - 1)\,, \\ G(t, p_G) &= p_3 + p_4 e^{-p_5 \cdot t} + p_6 e^{-p_7 \cdot t} + p_8 e^{-p_9 \cdot t}\,. \end{aligned} \tag{4.7}$$

The bounds of the parameters are

$$p_i \in (0, \infty) \quad \text{for} \quad i = 1, 2, 5, 7, 9 \quad \text{and} \tag{4.8}$$

$$p_i \in (0, 1) \quad \text{for} \quad i = 3, 4, 6, 8\,. \tag{4.9}$$

The sum of the coefficients for the viscoelastic material was chosen to be unity, in line with the viscoelastic material model implemented in ABAQUS (2016) . This is an equality constraint:

$$p_3 + p_4 + p_6 + p_8 = 1\,. \tag{4.10}$$

The smallest time constant $\tau_{min} = 1/max(p_i); i \in \{5, 7, 9\}$ should be larger than minimum time of the measured data, i.e. the sampling interval t_{min}, and the largest time constant $\tau_{max} = 1/min(p_i); i \in \{5, 7, 9\}$ should be smaller than the measurement time t_{max}. The time constants τ of the viscoelastic constitutive model are separated by at least a factor C. For the curve fit $C = 8$ was chosen. These conditions provide the inequality constraints:

$$p_9 \geq 1/t_{max} \qquad p_5 \leq 1/t_{min} \qquad \text{and} \tag{4.11}$$

$$\frac{p_5}{p_7} \geq C \qquad \frac{p_7}{p_9} \geq C \qquad \text{with} \qquad C = 8\,. \tag{4.12}$$

4.1.3 Curve Fit Procedure

Problem Definition in Terms of Constrained Optimisation

For an introduction to nonlinear regression refer to textbooks like Draper and Smith (1998) and Deuflhard and Hohmann (2002). Denote the reading points of the measured actuator force curve with $(t_i, y_i);\ i = 1, \ldots, m$, where m is the number of readings and y_i is the actuator force at time t_i. We want to find the parameters p of the model function Eq. 4.7, $Y(t, p)$, that best approximates measurement points and fulfil the equality and inequality constrains for the parameters. This can be stated as a *constrained optimisation* problem, which is customary written as (Chong and Zak, 2013)

$$\begin{array}{rll} \min & f(\mathbf{x}) & \mathbf{x} \in \mathbb{R}^n\,, \\ \text{subject to} & h_i(\mathbf{x}) = 0 & \text{for } i = 1, \ldots, k\,, \\ & g_j(\mathbf{x}) \leq 0 & \text{for } j = 1, \ldots, l\,, \end{array} \tag{4.13}$$

where $f\colon \mathbb{R}^n \to \mathbb{R}$ is the function to be optimised, also referred to as *objective function*, $h_i\colon \mathbb{R}^n \to \mathbb{R}$ with $k \leq n$ are the *equality constraints* and $g_j\colon \mathbb{R}^n \to \mathbb{R}$ are the *inequality constraints*.

The difference between measured value y_i at time t_i and predicted value $Y(t_i, p)$ is called error or *residual*. For the curve fit we want to minimise the sum of the squared residuals. With $\mathbf{x} = [t_i, y_i, p]$, the objective function is

$$f(\mathbf{x}) = \sum_{i=1}^{m} (y_i - Y(t_i, p))^2 \,. \tag{4.14}$$

For nonlinear least squares curve fit the *Levenberg-Marquardt method* (Levenberg, 1944; Marquardt, 1963) implemented in GNU Octave (Eaton et al., 2017) was used. Refer to the GNU Octave documentation of the function *leasqr* for details. The equality constraint is given by Eq. 4.10. Inequality constraints were derived from Eq. 4.11 and 4.12. The range of the parameters, that is Eq. 4.8 and Eq. 4.9, represent inequality constraints, however bounds of parameters were specified directly.

To mention is that in addition to Eq. 4.14 a weighting can be specified, i.e. sum of weighted squares of the residuals is minimised. This could be used to weight measured values if there is a known measurement error dependency.

Remarks on the Coefficient of Multiple Correlation

The coefficient of multiple correlation indicates how well measured and predicted values correlate. It is used throughout this work and therefore briefly discussed here. We start with some definitions. The sum of the squares of the difference of the measured value y_i and the mean value $\bar{y}$ is called *total sum of squares*:

$$SS_{tot} = \sum_{i=1}^{m} (y_i - \bar{y})^2 \,.$$

The sum of the squares of the deviations of the predicted curve fit value $Y(t_i, p)$ from the mean value $\bar{y}$ is called *regression sum of squares*:

$$SS_{reg} = \sum_{i=1}^{m} (Y(t_i, p) - \bar{y})^2 \,.$$

The sum of the squares of the difference of the measured value y_i and the predicted curve fit value $Y(t_i, p)$ is called *residual sum of squares*:

$$SS_{res} = \sum_{i=1}^{m} (y_i - Y(t_i, p))^2 \,.$$

The *coefficient of multiple correlation* is than defined by (Neter et al., 2004)

$$R^2 = 1 - \frac{SS_{res}}{SS_{tot}} \,. \tag{4.15}$$

In the case of *linear regression* it can be shown that, at the minimum, the residual is orthogonal to the range of the model function (Deuflhard and Hohmann, 2002) and therefore

$$SS_{tot} = SS_{reg} + SS_{res} \,.$$

With that R^2 can be written as

$$R^2 = \frac{SS_{reg}}{SS_{tot}} \,. \tag{4.16}$$

Motivated by this expression we can interpret R^2 as a measure of the part of the total variation that is explained by the regression. For linear regression the limits of R^2 are $0 \leq R^2 \leq 1$. The lower limit is obtained if $SS_{reg} = 0$, respectively $SS_{tot} = SS_{res}$, i.e. if the regression curve fits the data no better than a horizontal line through the mean value of the measured date. The upper limit is obtained if $SS_{reg} = SS_{tot}$, respectively $SS_{res} = 0$, that is if the regression curve passes through all measured data points.

For nonlinear regression we resort to Eq. 4.15. Here the notation R^2 is misleading in the sense that R^2 can have negative values. This is the case when $SS_{res} > SS_{tot}$, i.e. if the regression curve fits the data worse than a horizontal line through the mean value of the measured date. Again, the upper limit of R^2 is obtained when the residuals are zero.

As a final remark, high values of the coefficient of multiple correlation R^2 only tell that the regression curve is close to the measured values, it does not tell whether the chosen model function is physically meaningful. To illustrate the point, one could fit a degree $m-1$ polynomial that passes through the m measurement points[2], however this may be a poor model, that is pointless to understand the physical processes involved.

---

[2] Follows from the Fundamental Theorem of Algebra, see e.g. Bronstein et al. (2005)

Pre-processing of the Measured Data

Consider Tab. 4.1, test No. 10 has about 3300 measurement points. In principle it is feasible to do the curve fit with all measurement points. However, a preliminary investigation has shown that it is sufficient to use a reduced number of data points. Apart from computing time savings, there are further reasons to use a reduced number of data points. The model function Eq. 4.7 consists of a displacement function with two parameters and a time function with seven parameters. The time function is made up of exponential functions with time constants separated by about one order of magnitude. By using an appropriate method for selecting points, one can attempt to give all parameters equal weight, which should improve the curve fit.

Consider Fig. 4.3. The response for $0 \leq t \leq t_{ramp}$, i.e. left of the peak force point, is dominated by the displacement function. The displacement function has two from nine parameters. Therefore, as an initial estimate $20\,\%$ of the data points are placed in the first interval. To give the response close to the peak force point a higher weight, the points are biased towards the peak force point by decreasing the distance according to a geometric series. For $t > t_{ramp}$ actuator displacement remains constant, the displacement function does not change and the response is governed by the time function. The time function is made up from three decaying exponential terms. For larger times the exponential terms decay successively, according to their time constants. To give the exponential terms equal weight the distance between the data points is increased according to a geometric sequence. This reduces the weight of the long term response, where the first two exponential terms have already decayed and there is little change in the actuator force. In Fig. 4.3 the measured data of test No. 10 and the selected points are plotted. Preliminary analysis showed that a weight of $14\,\%$ for the first interval and approximately 40 points are sufficient for an acceptable curve fit.

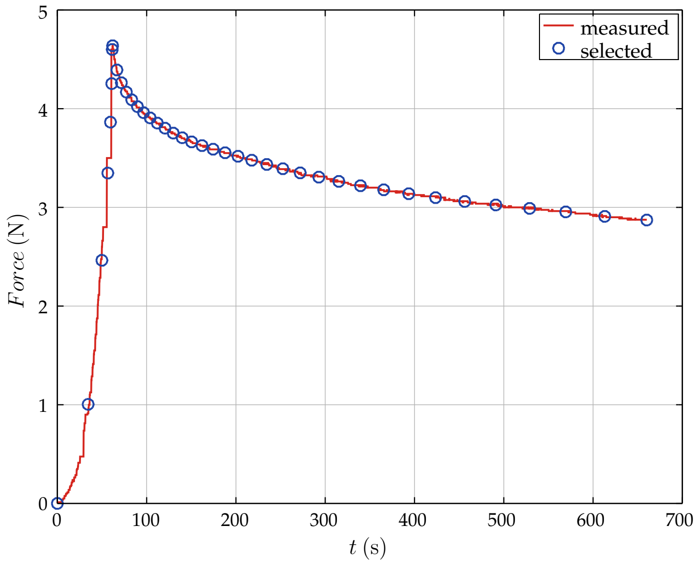

FIGURE 4.3: Measured and selected points of test No. 10.

As discussed in Chap. 4.1.1, small jumps in the measured force were observed. Using the measured force value at the selected point may be misleading. For example, if there is an systematic error in the recorded force that repeats with a pattern, it could be that forces are used at the low or high level, if points are selected with the same pattern. The steps in the recorded force could be due to delay effects or the data transmission rate of the digital data recording equipment.

To avoid these issues, local interpolations of the data around the selected points were performed and the interpolated force values were used for subsequent analysis. For the interpolations local curve fits with second-order polynomials were used. Depending on the position, data from up to three selected neighbouring points were used for the interpolation. For the first point, with $F(t = 0) = 0$ and the peak force point, with $t = t_{ramp}$, the measured values were retained. The value of the last point, with $t = t_{max}$, was interpolated from the last time interval. An example is shown in Fig. 4.4.

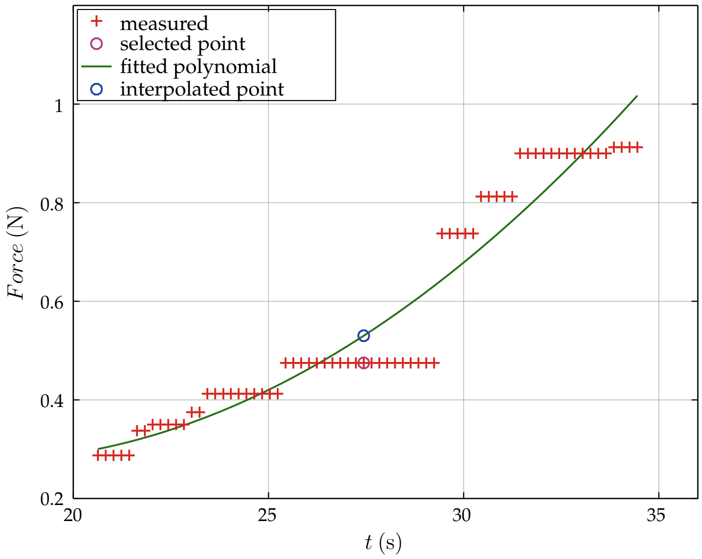

FIGURE 4.4: Interpolation of measured data (test No. 10 at 27.44 s).

Quasi-Static Response and Initial Estimate for Parameter p_1 and p_2

For a quasi-static load the model function reduces to Eq. 4.4 and the derivative with respect to x is

$$\frac{\partial F(x)}{\partial x} = p_2 F(x) + p_1 \tag{4.17}$$

Observe that this is a first order polynomial, i.e. a plot of $\partial F(x)/\partial x$ versus $F(x)$ should be a straight line for quasi-static load condition. In practice, measurements are taken over time and we replace $\partial F(x)/\partial x$ with help of the chain rule by $(\partial F(x)/\partial t)(\partial t/\partial x)$, i.e. we evaluate the time derivative of the measured force, divided by the velocity of the actuator input displacement, at constant actuator displacement velocity. An alternative approach would be to evaluate the steady state response, i.e. at several defined constant displacement inputs, evaluate the steady state force and estimate $\partial F(x)/\partial x$ from these data. Considering Fig. 4.1 we observe that steady state response is not achieved within the time of measurement. Therefore, we cannot evaluate the measurements of Papadopoulou et al. (2013) with the steady state approach.

Test No. 12 and No. 14, which are the valid tests closest to the quasi static condition, were evaluated with the first approach. The partial derivative of $\partial F(x)/\partial t$ was approximated with the difference quotient of the measured force and time data. The partial derivative $\partial t/\partial x$ is the inverse of the actuator velocity, which is readily obtained from actuator displacement and ramp time. With that, the estimate of $\partial F(x)/\partial x$ is obtained. The parameters p_1 and p_2 are calculated using a first order polynomial curve fit of the estimated $\partial F(x)/\partial x$ values. A plot of the evaluation is shown in Fig. 4.5 and the fitted parameters p_1 and p_2 of Eq. 4.17 are given in Tab. 4.2.

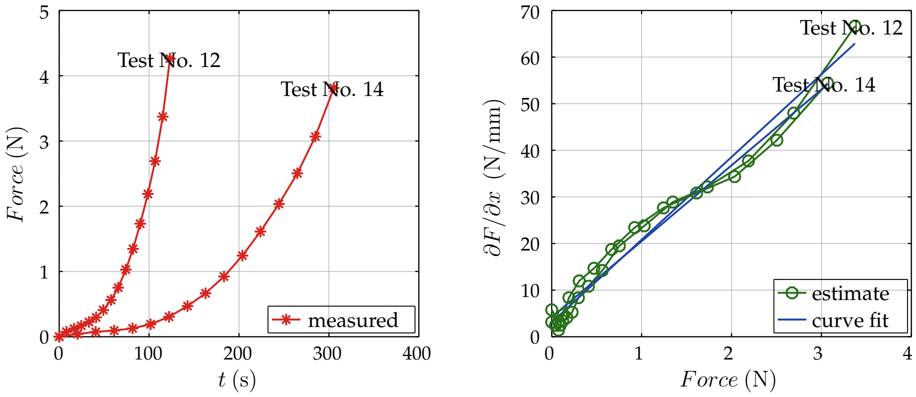

FIGURE 4.5: Initial estimate for parameter p_1 and p_2 of Eq. 4.17 based on test No. 12 and 14.

TABLE 4.2: Initial estimate for parameter p_1 and p_2.

test No.	p_1	p_2
12	3.08	17.7
14	4.22	18.2

Taking into account that the largest time constant of the viscoelastic model anticipated has the same order of magnitude as the actuator ramp time of test No. 12 and 14, dynamic effects are present. Therefore the quasi static assumption does not hold and the estimate of parameter p_1 and p_2 can only be considered as a first starting point.

Curve Fit Algorithm

The previous section provided an initial estimate for the parameters of the displacement function, p_1 and p_2. Apart from the equality and inequality constraints, no initial estimates of the remaining parameters are known. To make sure that the result of the curve fit is independent of initial values for the parameters $p_i;\ i \in \{3, \dots, 9\}$ a *full factorial experiment* (analysis) was conducted. The constants of the time function, i.e. parameters $p_i;\ i \in \{3, 4, 6, 8\}$, were set in eight levels. Taking equality constraint Eq. 4.10 into account, and assume the lower limit of $(p_i)_{min} = 0.1$, the upper limit $(p_i)_{max} = 0.7$ follows. The time constants were $\tau_j = 1/p_i;\ (j, i) \in \{(1, 5), (2, 7), (3, 9)\}$. The upper and lower limits of the interval for the time constants are obtained from Eq. 4.11 and Eq. 4.12. The intervals are than defined by $[C^{i-1}\tau_{min},\ \tau_{max}/C^{3-i}]_i;\ i = 1, 2, 3$. The interval was set in five levels, with intermediate level values increased according to a geometric sequence.

The full factorial experiment was realised in GNU octave with nested loops for the parameter. If the equality and inequality constrains were met, the model function was evaluated and the coefficient of multiple correlation R^2 was calculated. Than, if the R^2 value was larger than a threshold, the Levenberg-Marquardt curve fit procedure, including all parameters, was executed. Inputs, optimised parameters and corresponding results were stored in a text file for later evaluation.

The full factorial experiment results in $3^5 \cdot 4^8 = 512000$ combinations. After checking constraints 1820 evaluations of the model function remained. The threshold was chosen so that the Levenberg-Marquardt curve fit was executed about 20 times for an investigation. The last step should be kept to a minimum because each Levenberg-Marquardt curve fit execution noticeably increases computation time.

Algorithmus 1 : CURVE FIT PROCEDURE

```
Input : Measurement protocols (text files)
Output : A table with parameters and $R^2$ values (text file)

Read Input
Pre-process measured data
Input $p_1, p_2$ and test number(s)
begin FULL FACTORIAL EXPERIMENT on $p_i,\ i \in \{3, \dots, 9\}$
    if equality and inequality constraints are satisfied then
        Calculate $Y(t, p),\ R^2$
        Write $p,\ R^2$ to Output
        if $R^2 > threshold$ then
            Execute a Levenberg-Marquardt curve fit with all parameters
            Write $p,\ R^2$ to Output
        end
    end
end
```

Post-processing of the Curve Fit Results

Output of Algorithm 1 is a table with columns containing a flag, that indicates a function evaluation or a Levenberg-Marquardt curve fit, the corresponding parameters and R^2 value. For the Levenberg-Marquardt curve fits sanity checks were performed. The first check was whether one of the time constant parameters converged against the upper or lower constraint given by Eq. 4.11. The second check was whether one of the coefficients of the time function $p_i;\ i \in \{3, 4, 6, 8\}$ converged against zero. These conditions indicate that one of the exponential terms is superfluous. Therefore the corresponding curve fits were discarded from further evaluation.

The remaining Levenberg-Marquardt curve fits, with R^2 values above a threshold, were used for further evaluation. It is not assured that all Levenberg-Marquardt curve fits approach the global minimum of Eq. 4.14 and the data may contain local minima. If this is the case the average of the parameter values would be misleading. Instead, the remaining curve fits were clustered based on similarity of the time constants and the average of the parameters within the dominant cluster with highest R^2 value was calculated. With the averaged parameter values further Levenberg-Marquardt curve fits were done, until the third relevant digit of the recalculated parameters were settled and R^2 value was maximal.

4.1.4 Curve Fit of Individual Tests to Model Function Eq. 4.7

Curve fits of model function Eq. 4.7 to individual tests were performed. Results are listed in Tab. 4.3. A plot of the curve fit with lowest R^2 value, i.e. test No. 4 with $R^2 = 0.9673$, is shown in Fig. 4.6.

Discussion

Curve fits of individual tests approximate test data well. However, observe that time constants vary considerably between individual test. For example, the first time constant τ_1 of the test with 0.1 mm ramp displacement varies between $0.20\,\mathrm{s}$ for test No. 9, and $14.5\,\mathrm{s}$ for test No. 7. The first time constant τ_1 of the test with 0.2 mm ramp displacement varies between $0.20\,\mathrm{s}$ for test No. 8 and 10, and $8.00\,\mathrm{s}$ for test No. 14. Similar observations are made for the other parameters and this is also reflected in the large standard deviation. Recalling that all tests were made with the same specimen, one would expect lower variation in estimated parameters, at least for tests with the same actuator displacement.

TABLE 4.3: Curve fit of individual tests with actuator displacement 0.1 mm (odd test No.) and 0.2 mm (even test No.) to model function Eq. 4.7. Identified parameters of the model function, R^2, mean and standard deviation (S.D.) of the curve fit.

test	p_1	p_2	p_3	p_4	τ_1	p_6	τ_2	p_8	τ_3	R^2
-	-	-	-	-	s	-	s	-	s	-
3	17.1	7.89	0.178	0.480	3.38	0.116	30.7	0.226	395	0.9998
5	17.0	12.1	0.157	0.526	1.30	0.262	13.6	0.055	269	0.9971
7	5.70	18.0	0.277	0.592	14.5	0.058	169.	0.073	2520	0.9907
9	4.91	23.9	0.185	0.036	0.20	0.745	25.0	0.034	200	0.9841
11	3.49	26.1	0.151	0.153	5.65	0.608	45.2	0.088	2880	0.9967
2	18.6	9.49	0.307	0.249	6.27	0.126	57.9	0.318	506	0.9964
4	6.86	16.2	0.321	0.108	1.76	0.193	53.9	0.378	788	0.9673
6	13.6	13.1	0.251	0.431	1.32	0.159	18.9	0.159	310	0.9988
8	9.77	14.3	0.273	0.280	0.20	0.293	20.3	0.154	383	0.9931
10	8.72	14.9	0.239	0.279	0.20	0.344	28.0	0.138	374	0.9985
12	8.00	14.9	0.140	0.325	6.48	0.322	66.4	0.213	1490	0.9981
14	8.83	14.4	0.174	0.309	8.00	0.400	169.	0.117	2208	0.9967
mean	10.2	15.4	0.221	0.314	4.11	0.302	58.2	0.163	1027	-
S.D.	5.12	5.26	0.064	0.169	4.30	0.205	54.4	0.105	982.	-

4.1.5 Curve Fit of Test Groups to Model Function Eq. 4.7

A curve fit using model function Eq. 4.7 to tests with 0.2 ramp displacement, i.e. test No. 2, 4, 6, 8, 10, 12 and 14, grouped together was performed. Results are found in Tab. 4.4 and a plot is shown in Fig. 4.7. The correlation coefficient is $R^2 = 0.7636$. The maximum force F_{max} is shown in the lower left diagram. The curve fit of the maximum force follows the trend of the measured data, however increased deviation for test No. 6, 8, 10 and 12 is observed. The force at the end of the measurement F_{tmax} for each test is shown in the lower right diagram. Though curve fit of test No. 12 matches the test data well, the general trend of the remaining tests is not captured, in particular the progressively increased force characteristic observed for short ramp rise times of test No. 2, 4, 6 and 8 is not reproduced. Note that for test No. 4 an outlier is observed.

TABLE 4.4: Parameters for curve fit of model function Eq. 4.7 to tests with $d_{ramp} = 0.2\,\mathrm{mm}$, i.e. test No. 2, 4, 6, 8, 10, 12 and 14

d_{ramp}	p_1	p_2	p_3	p_4	τ_1	p_6	τ_2	p_8	τ_3	R^2
mm	-	-	-	-	s	-	s	-	s	-
0.2	15.6	10.9	0.137	0.219	4.30	0.353	34.4	0.291	798	0.7636

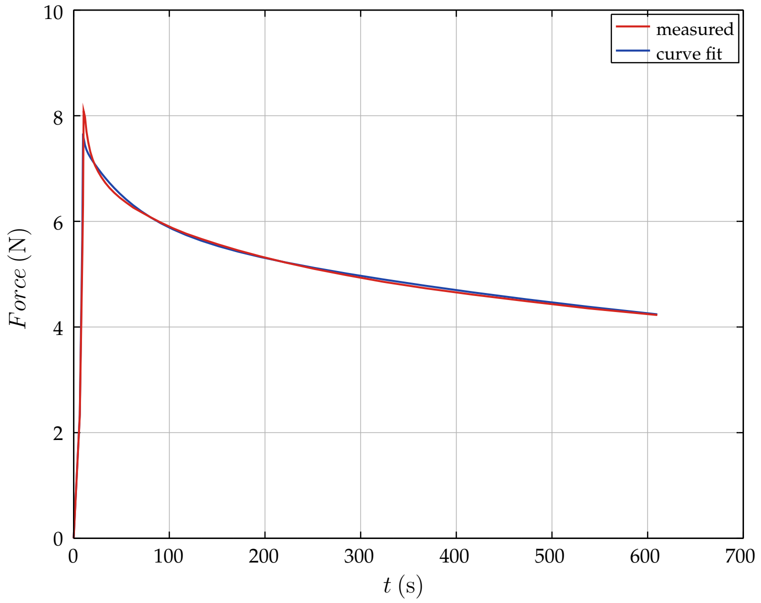

FIGURE 4.6: Curve fit of model function Eq. 4.7 to test No. 4, $R^2 = 0.9673$

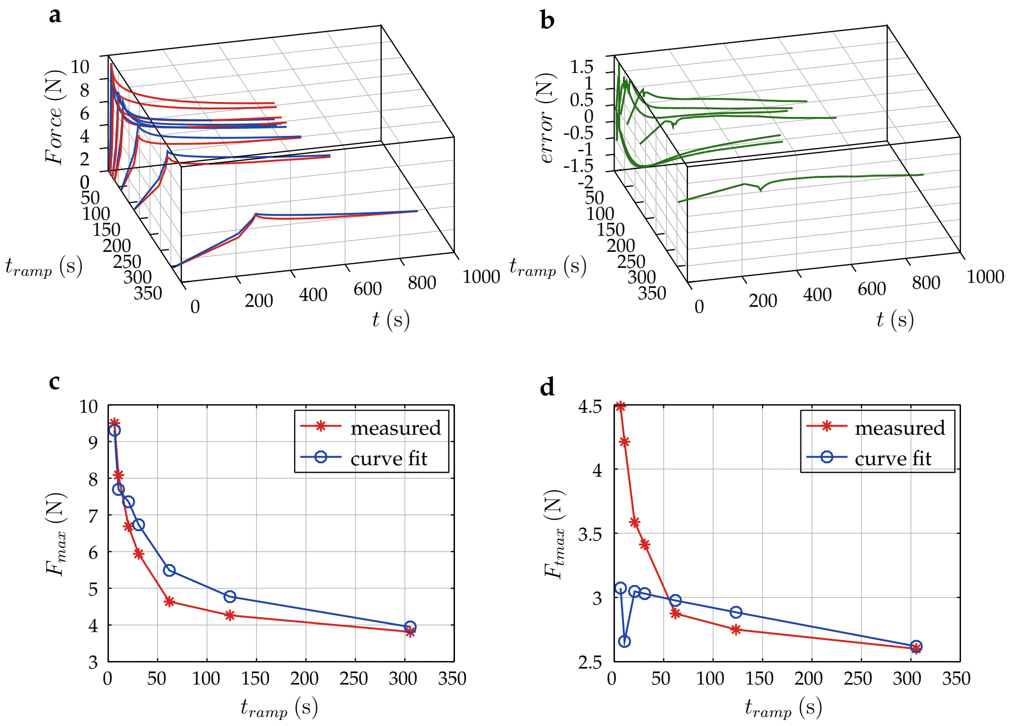

FIGURE 4.7: Curve fit of model function Eq. 4.7 to tests with $d_{ramp} = 0.2\,\mathrm{mm}$, i.e. test No. 2, 4, 6, 8, 10, 12 and 14, $R^2 = 0.7636$:

- **a**, measured (red) and curve fit force (blue) versus time t and ramp rise time t_{ramp} of the test;
- **b**, error, that is curve fit minus measured force versus time t and ramp rise time t_{ramp} of the test;
- **c**, peak force, measured (red) and curve fit (blue), versus ramp rise time t_{ramp} of the test;
- **d**, force at the end of the test, measured (red) and curve fit (blue), versus ramp rise time of the test.

Improved Model Function - Ramp Rise Time Term

Observe that for low ramp rise times t_{ramp}, the response between $t >> t_{ramp}$ and t_{max} shows a nearly constant error, i.e. difference between measured and fitted actuator force.

Attempts to improve correlation with additional exponential decay terms in $G(t, p_G)$ were not successful. With four exponential terms, depending on initial parameters, the lowest time constant converged to the lower limit given by the sample interval t_{sample} or one factor in front of a exponential function converged to zero. This indicates that the additional exponential term in $G(t, p_G)$ is superfluous.

Model function Eq. 4.7 describes a visco-elastic response and we may need an additional term in the model function that takes the described behaviour into account and further reduces the difference between curve fit and measured data. Considering Fig. 4.7 lower right, it is observed that above mentioned error decays with ramp rise time t_{ramp}. The error should also be a proportional to actuator displacement. Therefore the model function Eq. 4.7 is augmented by an additional term $H(x, p_H)$, that is proportional to actuator displacement and decays with ramp rise time t_{ramp} :

$$\begin{aligned} Y(t,p) &= F(x(t),p_F) \cdot G(t,p_G) + H(x(t),p_H) \, , \\ F(x,p_F) &= \frac{p_1}{p_2}(e^{p_2 \cdot x} - 1) \, , \\ G(t,p_G) &= p_3 + p_4 e^{-p_5 \cdot t} + p_6 e^{-p_7 \cdot t} + p_8 e^{-p_9 \cdot t} \, , \\ H(x,p_H) &= p_{10} \cdot x \cdot e^{-p_{11} \cdot t_{ramp}} \, , \end{aligned} \tag{4.18}$$

with parameters $p = \{p_F, p_G, p_H\}$. Bounds of the additional parameters $p_H = \{p_{10}, p_{11}\}$ are:

$$p_i \in (0, \infty) \qquad for \qquad i = 10, 11 \, .$$

Since actuator ramp velocity is inversely proportional to the actuator ramp time, the additional term $H(x, p_H)$ could also be written dependent on actuator ramp velocity. This indicates that there may be a velocity dependent effect present.

4.1.6 Curve Fit of Test Groups to Model Function Eq. 4.18

A curve fit of model function Eq. 4.18 to tests with $0.2\,\mathrm{mm}$ ramp displacement, i.e. test No. 2, 4, 6, 8, 10, 12, 14 and to tests with $0.1\,\mathrm{mm}$ ramp displacement, i.e. test No. 3, 5, 7, 9, 11 grouped together was performed. Results are listed in Tab. 4.5 and plots are shown in Fig. 4.8 and Fig. 4.9. The correlation coefficients are $R^2 = 0.9776$ and $R^2 = 0.9748$. Compared to Chap. 4.1.5 curve fit improved. Consider Fig. 4.8 lower left, the curve fit better replicates the measured characteristic. Test No. 2 shows largest F_{tmax} deviation.

TABLE 4.5: Parameters for curve fit of model function Eq. 4.18 to tests with $d_{ramp} = 0.2\,\mathrm{mm}$ (test No. 2, 4, 6, 8, 10, 12, 14) and to tests with $d_{ramp} = 0.1\,\mathrm{mm}$ (test No. 3, 5, 7, 9, 11).

d_{ramp}	p_1	p_2	p_3	p_4	τ_1	p_6	τ_2	p_8	τ_3	p_{10}	$1/p_{11}$	R^2
mm	-	-	-	-	s	-	s	-	s	-	s	-
0.2	7.66	13.8	0.291	0.216	3.87	0.261	33.1	0.232	400	20.2	14.1	0.9776
0.1	7.85	15.7	0.192	0.247	1.45	0.419	11.6	0.142	116	7.72	15.5	0.9748

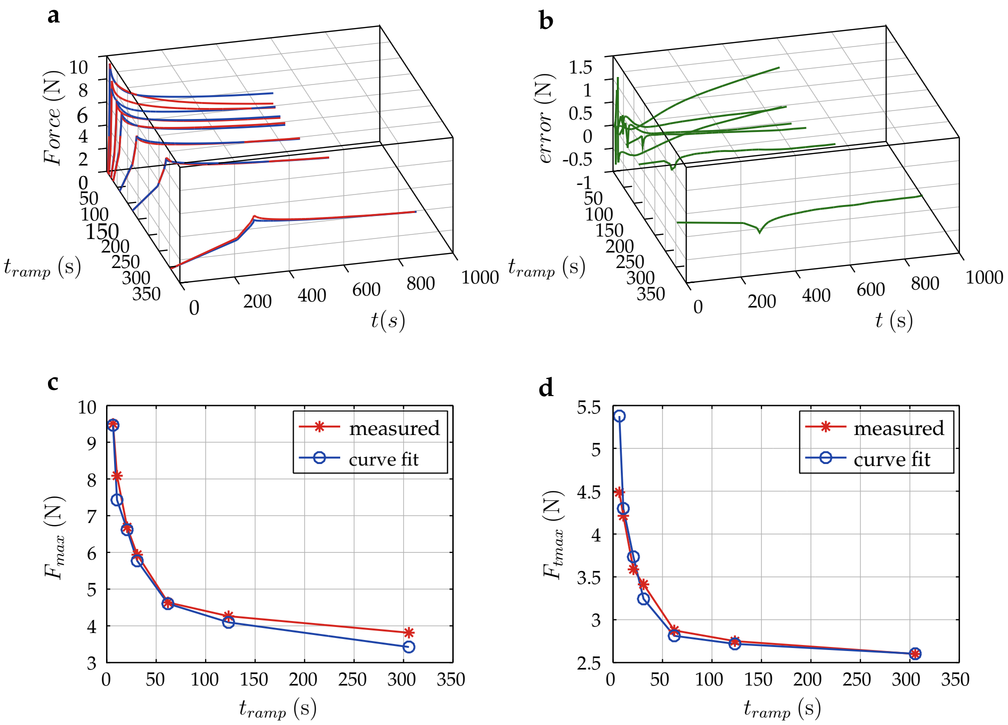

FIGURE 4.8: Curve fit of model function Eq. 4.18 to tests with $d_{ramp} = 0.2\,\mathrm{mm}$ ramp displacement (test No. 2, 4, 6, 8, 10, 12, 14), $R^2 = 0.9776$:

- **a**, measured (red) and curve fit force (blue) versus time t and ramp rise time t_{ramp} of the test;
- **b**, error, that is curve fit minus measured force versus time t and ramp rise time t_{ramp} of the test;
- **c**, peak force, measured (red) and curve fit (blue), versus ramp rise time t_{ramp} of the test;
- **d**, force at the end of the test, measured (red) and curve fit (blue), versus ramp rise time of the test.

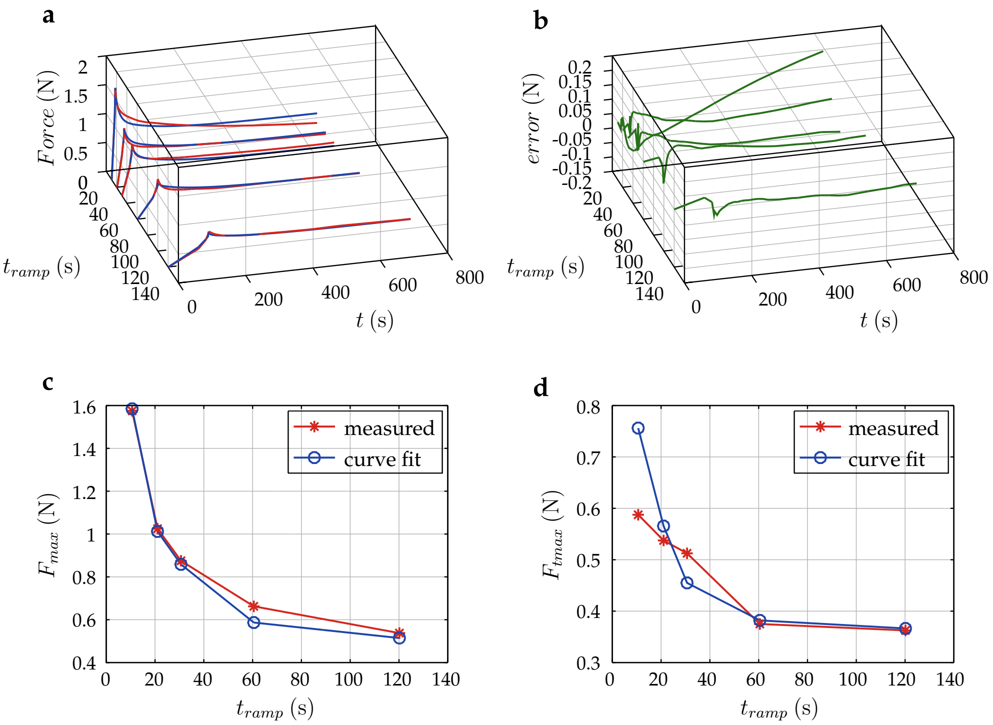

FIGURE 4.9: Curve fit of model function Eq. 4.18 to tests with $d_{ramp} = 0.1\,\mathrm{mm}$ ramp displacement (test No. 3, 5, 7, 9, 11), $R^2 = 0.9748$:

- **a**, measured (red) and curve fit force (blue) versus time t and ramp rise time t_{ramp} of the test;
- **b**, error, that is curve fit minus measured force versus time t and ramp rise time t_{ramp} of the test;
- **c**, peak force, measured (red) and curve fit (blue), versus ramp rise time t_{ramp} of the test;
- **d**, force at the end of the test, measured (red) and curve fit (blue), versus ramp rise time of the test.

Improved Model Function - Prior Load History Term

Considering Tab. 4.1 it is observed that the rest time t_{rest}, that is, the difference between the start time of the current test and the end time of the previous test, varied considerably from test to test.

Assume visco elastic material behaviour is valid. If the rest time is not considerably larger than the largest time constant of the visco elastic material, the influence of residual strains due to the previous tests may not be neglected. To illustrate the point consider the response of a Maxwell Element to the three pulses $x(t)$ shown in Fig. 4.10. The total displacement of the Maxwell Element $x(t)$ is the sum of the spring displacement $x_s(t)$ and damper displacement $x_d(t)$,

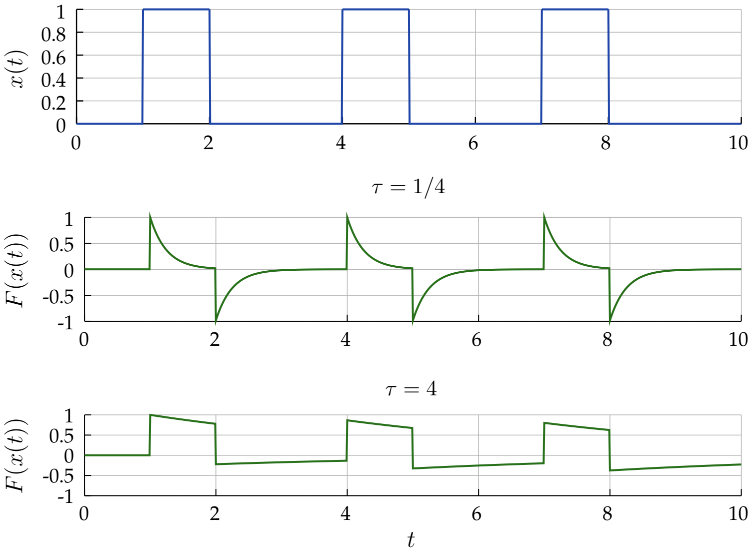

FIGURE 4.10: Response of a Maxwell element $F(x(t))$ to a pulse input x(t) depending on time constant τ.

i.e. $x(t) = x_s(t) + x_d(t)$. The force in the spring $f = \mu x_s(t)$, with spring stiffness μ, and the force in the damper $f = \eta \dot{x}_d(t)$, with viscosity η, are equal. Differentiating the total displacement with respect to time and substituting the time derivative of spring and damper displacement leads to the differential equation

$$\dot{f}(t) + \frac{1}{\tau} f(t) = \mu \dot{x}(t) ,$$

with time constant $\tau = \eta/\mu$. To solve the differential equation we take the Laplace Transformation[3] and find, with initial conditions equal to zero:

$$f(s) = \frac{\mu s}{1/\tau + s} x(s) .$$

The pulse signal $x(t)$ can be written in the time domain in terms of two unit step functions $u(t - t_0)$, with t_0 set to the corresponding start time t_{ps} and end time t_{pe} of the pulse

$$x(t) = \sum_{k=1}^{3} [\, u(t - t_{ps}) - u(t - t_{pe}) \,]_k .$$

---

[3] see e.g. Bronstein et al. (2005), Chap. 15.2

Taking the Laplace Transformation

$$x(s) = \sum_{k=1}^{3} [\, \frac{e^{-t_{ps}\, s}}{s} - \frac{e^{-t_{pe}\, s}}{s} \,]_k$$

and substituted into $F(s)$ gives

$$F(s) = \sum_{k=1}^{3} [\frac{\mu}{1/\tau + s}(e^{-t_{ps}\, s} - e^{-t_{pe}\, s})]_k \, .$$

The inverse Laplace Transformation provides the solution in the time domain

$$F(t) = \mu \sum_{k=1}^{3} [\, e^{-(t-t_{ps})/\tau}\, u(t-t_{ps}) - e^{-(t-t_{pe})/\tau}\, u(t-t_{pe}) \,]_k \, . \tag{4.19}$$

A plot of $F(t)$, with $\mu = 1$, for time constant $\tau = 1/4\,\mathrm{s}$ and $\tau = 4\,\mathrm{s}$, is given in Fig. 4.10. In the first case the time constant is $1/4$ of the pulse width of $1\,\mathrm{s}$ and $1/8$ of the rest time of $2\,\mathrm{s}$. At the end of the pulse the contribution of the first positive unit step has decayed to $e^{-4} = 0.018$ and at the end of the rest time the contribution of the second negative unit step has decayed to $e^{-8} = 3.4 \cdot 10^{-4}$. This means at the start of the next pulse, the contribution of the previous pulse is negligible. In the second case the time constant is 4 times the pulse width of $1\,\mathrm{s}$ and 2 times the rest time of $2\,\mathrm{s}$. At the end of the pulse the contribution of the first positive unit step has decayed to $e^{-(1/4)} = 0.779$ and at the end of the rest time the contribution of the second negative unit step has decayed to $e^{-(1/2)} = 0.607$. This means at the start of the next pulse, the contribution of the previous pulse is significant. This is also observed in the lower plot of Fig. 4.10.

Consider Tab. 4.1 and 4.3. For test No 4 the rest time was $290\,\mathrm{s}$ and the largest time constant of the previous test is $395\,\mathrm{s}$. This means that the rest time is smaller than the largest time constant. Therefore the contribution of the previous test No. 3 to the response of test No. 4 is present. However for test No. 4, the actuator displacement of the previous test No. 3 was $0.1\,\mathrm{mm}$, with corresponding low actuator force magnitude and low contribution of test No. 3 residual strain to the actuator force response of test No. 4. For test No. 7 the rest time was $400\,\mathrm{s}$ and the largest time constant of the previous test is $310\,\mathrm{s}$. This means that the rest time is smaller than the largest time constant. Therefore the contribution of the previous test No. 6 to the response of test No. 7 is present. For test No. 7, the actuator displacement of the previous test No. 6 was $0.2\,\mathrm{mm}$, with corresponding high actuator force magnitude and large contribution of test No. 6 residual strain to the actuator force response of test No. 7. Similar observations can be made for the other tests.

Concluding, for odd numbered tests, if the largest time constant of the previous test is not considerably smaller than the rest time of the current test, a significant contribution of the previous test residual strain to the response of the current test is anticipated.

In order to take into account the residual strain effects of previous tests on the current test, we introduce in Eq. 4.18 an additional term $K(t, p_K)$ analogue to Eq. 4.19. Only the contribution of the exponential function in $G(t, p_G)$ with the largest time constant is taken into account, since, by virtue of the inequality constraints, the decay of the other exponential terms is at least by a factor of $e^{-8} = 3.4 \cdot 10^{-4}$ smaller. We sum the contribution of all tests before the current test. The actuator displacement of the previous test is approximated by a pulse of height d_{ramp}, starting at the end of the ramp and ending at the end of the test. The time variable t of the current test starts at zero. As fixed reference time for the previous test we choose start of test No. 1. We provide the start time of the current test t_{start} and the pulse start times t_{ps} and pulse end times t_{pe} of the previous tests relative to this reference. The measured force was set to zero at the start of the test. Therefore we have to subtract $K(t = 0, p_K)$ to satisfy $Y(x, t = 0, p) = 0$. The augmented model function is than

$$
\begin{aligned}
Y(t,p) &= F(x(t),p_F) \cdot G(t,p_G) + H(x(t),p_H) + K(t,p_K) - K(t=0,p_K)\;, \\
F(x,p_F) &= \frac{p_1}{p_2}(e^{p_2 \cdot x} - 1)\;, \\
G(t,p_G) &= p_3 + p_4 e^{-p_5 \cdot t} + p_6 e^{-p_7 \cdot t} + p_8 e^{-p_9 \cdot t}\;, \\
H(x,p_H) &= p_{10} \cdot x \cdot e^{-p_{11} \cdot t_{ramp}}\;, \\
K(t,p_K) &= \sum_{k=1}^{testNo.-1} [\,F(d_{ramp},p_F)\, p_8\, (e^{-p_9(t_{start}-t_{ps}+t)} - e^{-p_9(t_{start}-t_{pe}+t)})\,]_k\;,
\end{aligned}
\tag{4.20}
$$

with $p_K = \{p_8, p_9, t_{start}, \{t_{ps}, t_{pe}, d_{ramp}\}_k\}$. Two parameters form p_G and known test data are required for calculation of $K(t, p_K)$. Hence, no additional parameter is introduced.

4.1.7 Curve Fit of Test Groups to Model Function Eq. 4.20

A curve fit of model function Eq. 4.20 to tests with $0.2\,\mathrm{mm}$ actuator displacement, i.e. test No. 2, 4, 6, 8, 10, 12, 14 and to tests with $0.1\,\mathrm{mm}$ actuator displacement, i.e. test No. 3, 5, 7, 9, 11 grouped together was performed. Results of the curve fit are shown in Tab. 4.6 and plots are shown in Fig. 4.11 and Fig. 4.12. The correlation coefficients are $R^2 = 0.9782$ and $R^2 = 0.9882$. Compared to Sec. 4.1.6 curve fit improved. For test with 0.2 mm actuator displacement a marginal improvement is observed. Consider Fig. 4.12 lower left, the replication of the measured F_{tmax} trend improved versus Fig. 4.9. Considering Tab. 4.6, observe that time constants estimated are similar, however the factors in front of the exponential terms are significantly different. This indicates a different behaviour of $0.2\,\mathrm{mm}$ and $0.1\,\mathrm{mm}$ actuator displacement test.

TABLE 4.6: Parameters for curve fit of model function Eq. 4.20 to tests with $d_{ramp} = 0.2\,\mathrm{mm}$ (test No. 2, 4, 6, 8, 10, 12, 14) and to tests with $d_{ramp} = 0.1\,\mathrm{mm}$ (test No. 3, 5, 7, 9, 11).

d_{ramp} mm	p_1 -	p_2 -	p_3 -	p_4 -	τ_1 s	p_6 -	τ_2 s	p_8 -	τ_3 s	p_{10} -	$1/p_{11}$ s	R^2 -
0.2	8.10	13.7	0.275	0.239	3.21	0.252	31.1	0.234	372	20.4	13.8	0.9782
0.1	14.9	9.27	0.027	0.663	2.99	0.156	47.6	0.154	381	14.3	10.1	0.9882

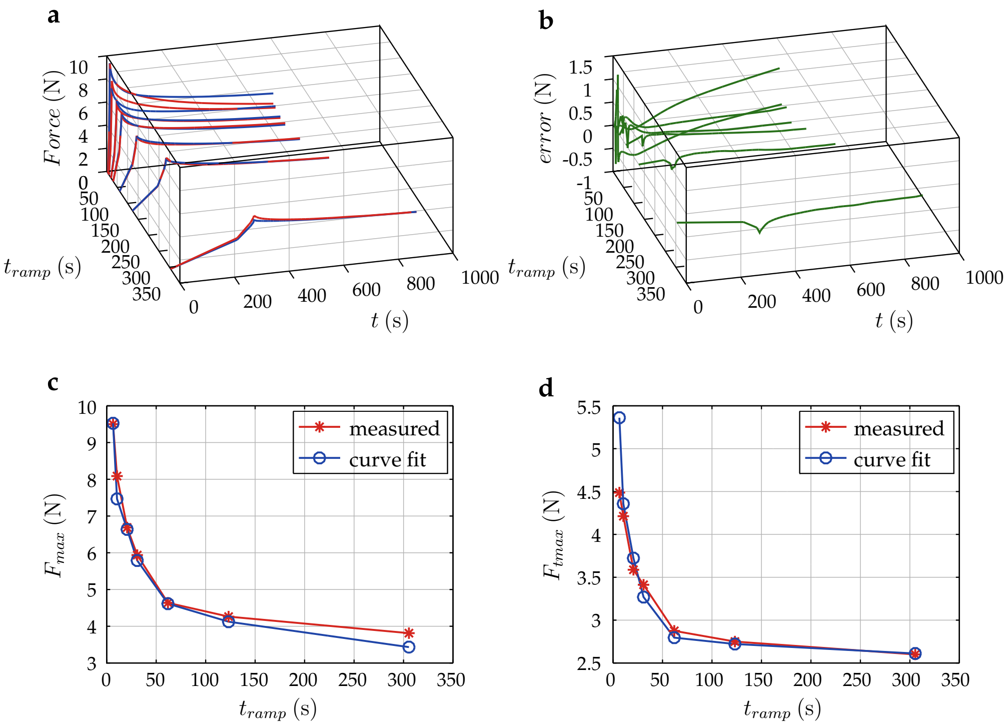

FIGURE 4.11: Curve fit of model function 4.20 to tests with $d_{ramp} = 0.2\,\text{mm}$, i.e. test No. 2, 4, 6, 8, 10, 12 and 14, $R^2 = 0.9782$:

- **a**, measured (red) and curve fit force (blue) versus time t and ramp rise time t_{ramp} of the test;
- **b**, error, that is curve fit minus measured force versus time t and ramp rise time t_{ramp} of the test;
- **c**, peak force, measured (red) and curve fit (blue), versus ramp rise time t_{ramp} of the test;
- **d**, force at the end of the test, measured (red) and curve fit (blue), versus ramp rise time of the test.

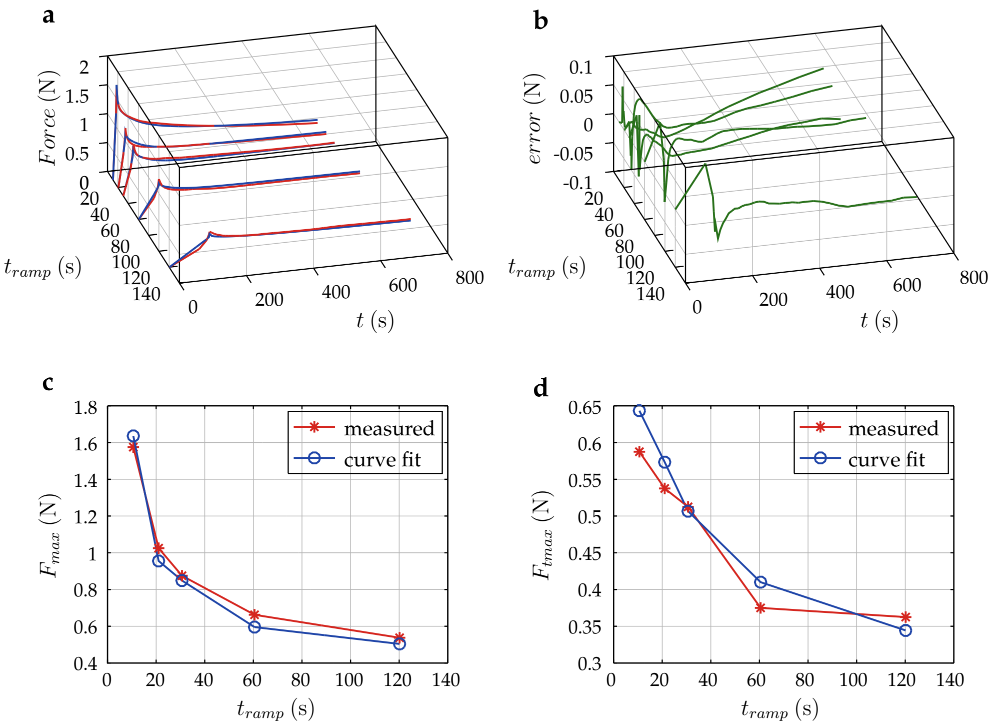

FIGURE 4.12: Curve fit of model function 4.20 to tests with $d_{ramp} = 0.1\,\mathrm{mm}$, i.e. test No. 3, 5, 7, 9 and 11, $R^2 = 0.9882$:

- **a**, measured (red) and curve fit force (blue) versus time t and ramp rise time t_{ramp} of the test;
- **b**, error, that is curve fit minus measured force versus time t and ramp rise time t_{ramp} of the test;
- **c**, peak force, measured (red) and curve fit (blue), versus ramp rise time t_{ramp} of the test;
- **d**, force at the end of the test, measured (red) and curve fit (blue), versus ramp rise time of the test.

4.1.8 Curve Fit of All Valid Tests to Model Function Eq. 4.20

A curve fit of model function Eq. 4.20 to all valid tests, i.e. test No. 2 to 12 and 14 was performed. Results of the cure fit are shown in Tab. 4.7, a plot with parameters of curve fit result No. 1 is shown in Fig. 4.13. Compared to Sec. 4.1.6 the curve fit correlation coefficient R^2 deteriorated. There was no unique solution, instead three parameter sets, with similar correlation coefficient were found. Observe that, compared to Sec. 4.1.7, time constants estimated are different. There we mentioned, that the factors in front of the exponential terms are significantly different for 0.2 and 0.1 mm actuator displacement test. The results indicate that it may not be possible to find a parameter set which fit both test conditions equally well. This assertion is supported by the observation that the curve fit procedure did not find a unique solution.

TABLE 4.7: Curve fit of model function Eq. 4.20 to all valid tests, i.e. test No. 2 to 12 and 14.

No.	p_1	p_2	p_3	p_4	τ_1	p_6	τ_2	p_8	τ_3	p_{10}	$1/p_{11}$	R^2
-	-	-	-	-	s	-	s	-	s	-	s	-
1	3.16	21.6	0.273	0.268	2.14	0.221	17.1	0.238	140.	20.6	10.0	0.9774
2	4.36	20.5	0.216	0.534	4.36	0.224	131.	0.026	1047	19.2	10.2	0.9744
3	2.64	21.0	0.252	0.424	22.7	0.247	308.	0.077	2468	19.3	10.5	0.9795

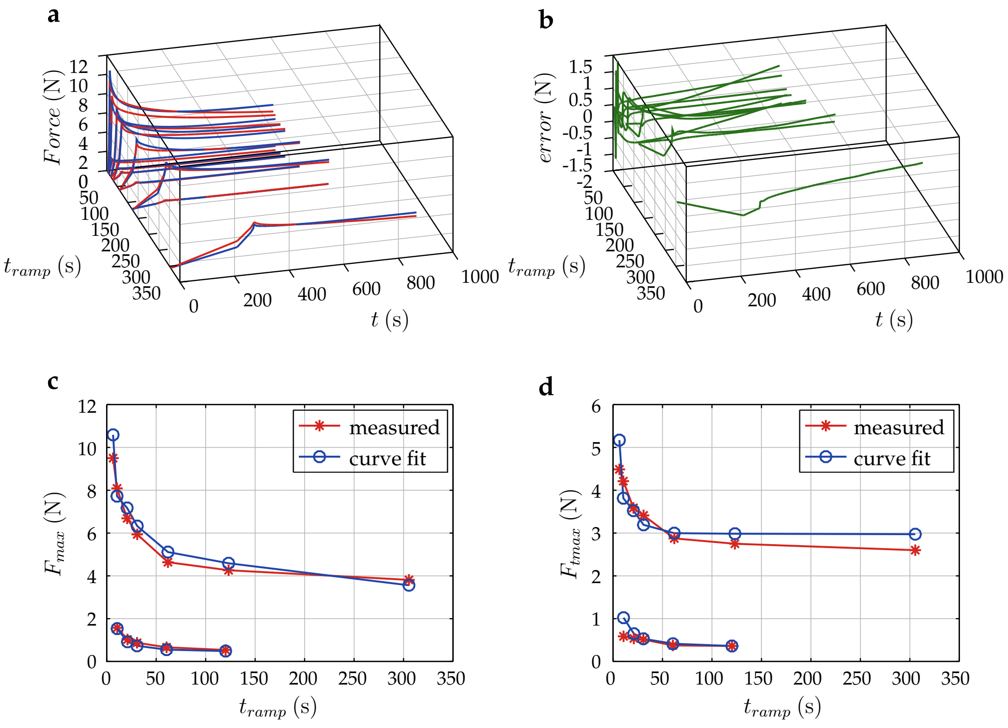

FIGURE 4.13: Curve fit of model function Eq. 4.20 to all valid tests, i.e. test No. 2 to 12, and 14, $R^2 = 0.9774$:

a, measured (red) and curve fit force (blue) versus time t and ramp rise time t_{ramp} of the test;

b, error, that is curve fit minus measured force versus time t and ramp rise time t_{ramp} of the test;

c, peak force, measured (red) and curve fit (blue), versus ramp rise time t_{ramp} of the test;

d, force at the end of the test, measured (red) and curve fit (blue), versus ramp rise time of the test.

Based on Sec. 4.1.7 results for the curve fit of model function Eq. 4.20 to tests with actuator displacement $d_{ramp} = 0.2\,\mathrm{mm}$, parameter p_1 and p_2 were varied according to Eq. 4.5 and a maximum of the correlation coefficient was found with $c = 0.30$. Results of the cure fit are shown in Tab. 4.8, a plot is given in Fig. 4.14. Observe that, by virtue of Eq. 4.5, the response of the actuator displacement $d_{ramp} = 0.2\,\mathrm{mm}$ tests did not change after the point where actuator displacement is kept constant, i.e. for times larger than t_{ramp}. Therefore the F_{max} and the F_{tmax} curve of the actuator displacement $d_{ramp} = 0.2\,\mathrm{mm}$ tests are identical to Fig. 4.11. The F_{max} curve of the actuator displacement $d_{ramp} = 0.1\,\mathrm{mm}$ tests replicates measured characteristics well. However for the F_{tmax} curve of the actuator displacement $d_{ramp} = 0.1\,\mathrm{mm}$ tests a deviation versus measured characteristics is observed. Overall, the correlation coefficient R^2 improved versus Tab. 4.7.

TABLE 4.8: Parameters of model function Eq. 4.20 for curve fit of all valid tests, based on results in Tab. 4.6 for actuator displacement $d_{ramp} = 0.2\,\mathrm{mm}$, parameter p_1 and p_2 varied according to Eq. 4.5 with $c = 0.30$.

p_1	p_2	p_3	p_4	τ_1	p_6	τ_2	p_8	τ_3	p_{10}	$1/p_{11}$	R^2
-	-	-	-	s	-	s	-	s	-	s	-
2.43	21.8	0.275	0.239	3.21	0.252	31.1	0.234	372.	20.4	13.8	0.9800

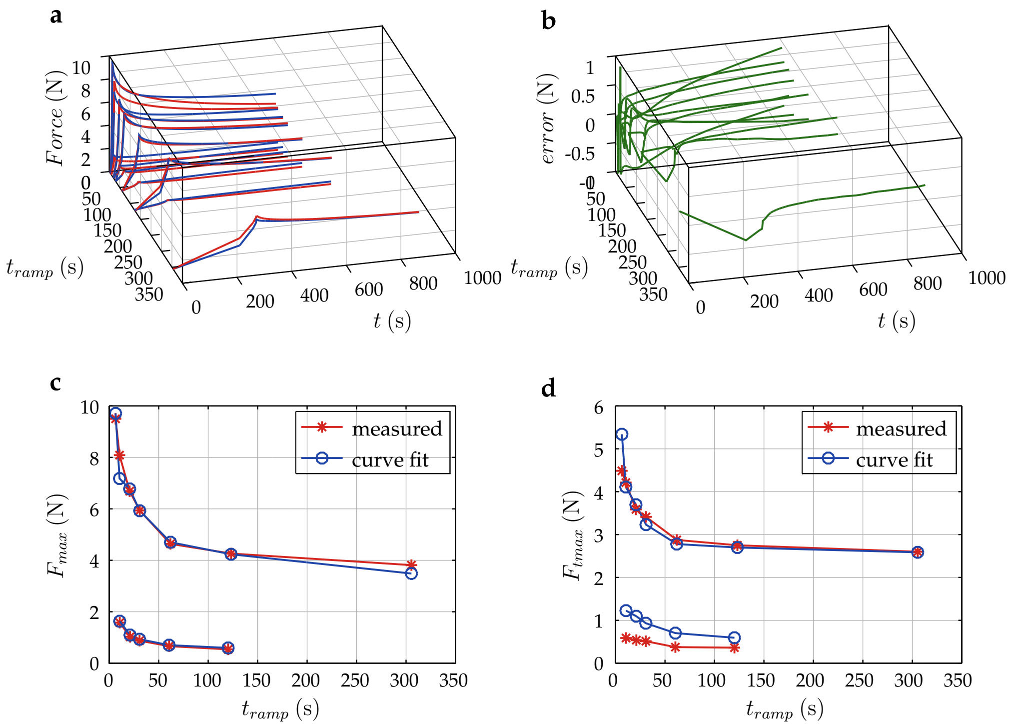

FIGURE 4.14: Curve fit of model function Eq. 4.20 for all valid tests, based on results in Tab. 4.6 actuator displacement $d_{ramp} = 0.2\,\mathrm{mm}$, parameter p_1 and p_2 varied according to Eq. 4.5 with $c = 0.30$, $R^2 = 0.9800$:

- **a**, measured (red) and curve fit force (blue) versus time t and ramp rise time t_{ramp} of the test;
- **b**, error, that is curve fit minus measured force versus time t and ramp rise time t_{ramp} of the test;
- **c**, peak force, measured (red) and curve fit (blue), versus ramp rise time t_{ramp} of the test;
- **d**, force at the end of the test, measured (red) and curve fit (blue), versus ramp rise time of the test.

4.2 Curve Fit - In Vivo Test of Konermann

4.2.1 Test Data

An overview of the in vivo measurements done by Konermann et al. (2017) is shown in Tab. 4.9. Actuator displacement $x(t)$ was input as a function of time t defined as follows: The displacement of the actuator rose at constant speed $v_{ramp} = d_{ramp}/t_{ramp}$, between $t = 0$ and the ramp rise time $t = t_{ramp}$, to the maximum actuator displacement d_{ramp}. Thereafter the actuator displacement decreased with constant speed v_{ramp} to zero at time $t = t_{max} = 2\,t_{ramp}$.

$$x = x(t) = \begin{cases} v_{ramp} \cdot t, & 0 \leq t \leq t_{ramp} \\ v_{ramp} \cdot (2\,t_{ramp} - t), & t_{ramp} < t \leq t_{max} \end{cases} \tag{4.21}$$

TABLE 4.9: Overview of the in vivo test, Konermann et al. (2017).

test	t_{start}	t_{ramp}	d_{ramp}	t_{sample}	t_{max}	t_{Fmax}	F_{max}	t_{rest}
-	hh:mm:ss	s	mm	s	s	s	N	s
1	17:04:07	0.2	0.2	0.02	0.4	0.24	15.9	-
2	17:04:46	0.5	0.2	0.05	1.0	0.55	14.8	38.6
3	17:05:19	1.0	0.2	0.05	2.0	1.0	14.5	32.0
4	17:05:57	2.0	0.2	0.10	4.0	2.0	13.4	36.0
5	17:06:33	5.0	0.2	0.25	10.0	5.0	12.5	32.0
6	17:07:17	10.0	0.2	0.50	20.0	10.0	11.7	34.0

4.2.2 Model Function

We come back to the final version of the model function Eq. 4.20 in Chap. 4.1. Now, the displacement function $x(t)$ is given by Eq. 4.21. Assuming the in vivo test is dominated by the PDL behaviour, the model function should be adequate to describe the in vivo test response. Consider Tab. 4.9, the sampling rate is $0.2\,\mathrm{s}$ and the longest test duration is $20\,\mathrm{s}$. For the in vitro tests in Chap. 4.1, the smallest time constant was about $4\,\mathrm{s}$. Therefore, assuming the smallest time constant of the in vivo test has about the same order of magnitude, it is presumed that at most one exponential decay term of the time function $G(t, p_G)$ can be estimated. Preliminary investigations showed that this is in fact the case. Therefore, only one exponential term of the time function $G(t, p_G)$ was retained.

The model function is than

$$
\begin{aligned}
Y(t,p) &= F(x(t),p_F)\cdot G(t,p_G) + H(x(t),p_H) + K(t,p_K) - K(t=0,p_K)\,,\\
F(x,p_F) &= \frac{p_1}{p_2}(e^{p_2\cdot x}-1)\,,\\
G(t,p_G) &= p_3 + p_4 e^{-p_5\cdot t}\,,\\
H(x,p_H) &= p_{10}\cdot x\cdot e^{-p_{11}\cdot t_{ramp}}\,,\\
K(t,p_K) &= \sum_{k=1}^{testNo.-1}\,[\,F(d_{ramp},p_F)\,p_4\,(e^{-p_5(t_{start}-t_{ps}+t)} - e^{-p_5(t_{start}-t_{pe}+t)})\,]_k\,.
\end{aligned}
\tag{4.22}
$$

Equality and inequality constraints carry over from Chap. 4.1. The curve fit procedure is, with the exception that the pre-processing step was skipped due to smaller number of data points, identical to Chap. 4.1.3.

4.2.3 Curve Fit of all Tests to Model Function Eq. 4.22

A first curve fit of model function Eq. 4.22, without the $H(x,p_H)$ and $K(t,p_K)$ term, was done for all tests grouped together. Results are listed in Tab. 4.10. The coefficient of multiple correlation is $R^2 = 0.99524$. Consider a plot of the results in Fig. 4.15, a dependency of the peak force on ramp time is observed. This is of the same kind as seen for the in vitro measurement in Chap. 4.1.6.

A second curve fit of model function 4.22, without the $K(t,p_K)$ term, was done for all tests grouped together. Results are listed in Tab. 4.10. The coefficient of multiple correlation improved to $R^2 = 0.9637$. Observe that the coefficient in front of the exponential decay term p_4 is zero. That is, the curve fit identified that the exponential decay term of $G(t,p_G)$ has no contribution. Therefore it could be omitted without deteriorating the curve fit. Consider a plot of the results in Fig. 4.16, the dependency of peak force on ramp rise time, and the force ascent and descent branch are captured well. However there is a difference between measured and curve fitted peak force. The measured force curve shows a broadly rounded peak response, that may be due to compliance of the measurement chain. Increasing the weight of the peak force in the curve fit procedure could improve the fit of the peak force at the expense of the fit of the ascent and descent branch.

A third curve fit of model function Eq. 4.22 with all terms was done for all tests grouped together. Results are listed in Tab. 4.10. The coefficient of multiple correlation is $R^2 = 0.9637$. The parameters p_1 and p_2, and the dependency of peak force on ramp rise time, i.e. p_{10} and p_{11}, are marginally different compared to the second curve fit. Again, the coefficient in front of the exponential decay term p_4 is zero. With that, the $K(t, p_K)$ term should be negligible, however the small contribution of this term may have lead to the slightly different parameters estimated.

Concluding, because of the negligible effect of the $G(t, p_G)$ and $K(t, p_K)$ terms identified, these terms are omitted in Eq. 4.22. The model function is than

$$\begin{aligned} Y(t,p) &= F(x(t),p_F) + H(x(t),p_H) \; , \\ F(x,p_F) &= \frac{p_1}{p_2}(e^{p_2 \cdot x} - 1) \; , \\ H(x,p_H) &= p_{10} \cdot x \cdot e^{-p_{11} \cdot t_{ramp}} \; . \end{aligned} \tag{4.23}$$

With model function 4.23 a fourth curve fit was done. Results are listed in Tab. 4.10. The coefficient of multiple correlation is to the fourth significant digit identical to second and third curve fit. Corresponding parameters of the model function are almost identical.

TABLE 4.10: Parameters for curve fit of model function Eq. 4.22 (No. 1 – without $H(x, p_H)$ and $K(t, p_K)$, No. 2 without $K(t, p_K)$, No. 3 – with all terms) and model function Eq. 4.23 (No. 4) for all tests grouped together.

curve fit	p_1	p_2	p_3	p_4	τ_1	p_{10}	$1/p_{11}$	R^2
-	-	-	-	-	s	-	s	-
1.	33.5	7.14	0.94	0.06	2.61	-	-	0.9524
2.	27.6	8.07	1.00	0.00	200.	14.9	1.36	0.9637
3.	27.5	8.10	1.00	0.00	200.	15.0	1.38	0.9637
4.	27.6	8.08	-	-	-	14.9	1.36	0.9637

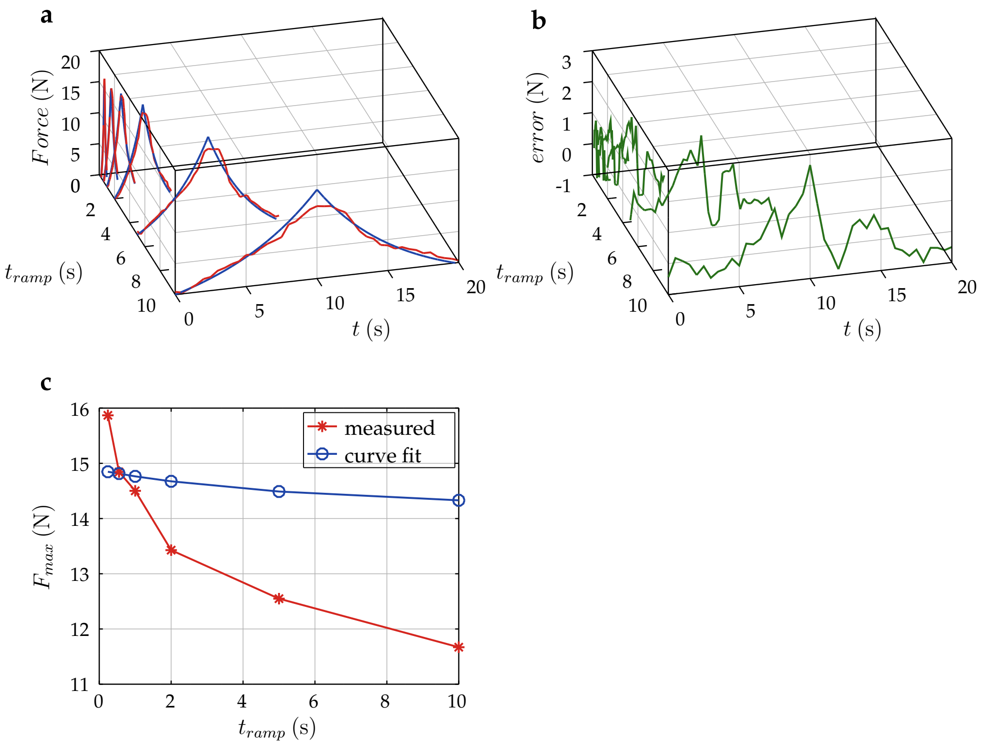

FIGURE 4.15: Curve fit of all tests to model function Eq. 4.22 without $H(x, p_H)$ and $K(t, p_K)$ term, $R^2 = 0.9524$:

a, measured (red) and curve fit force (blue) versus time t and ramp rise time t_{ramp} of the test;

b, error, that is curve fit minus measured force versus time t and ramp rise time t_{ramp} of the test;

c, peak force, measured (red) and curve fit (blue), versus ramp rise time t_{ramp} of the test.

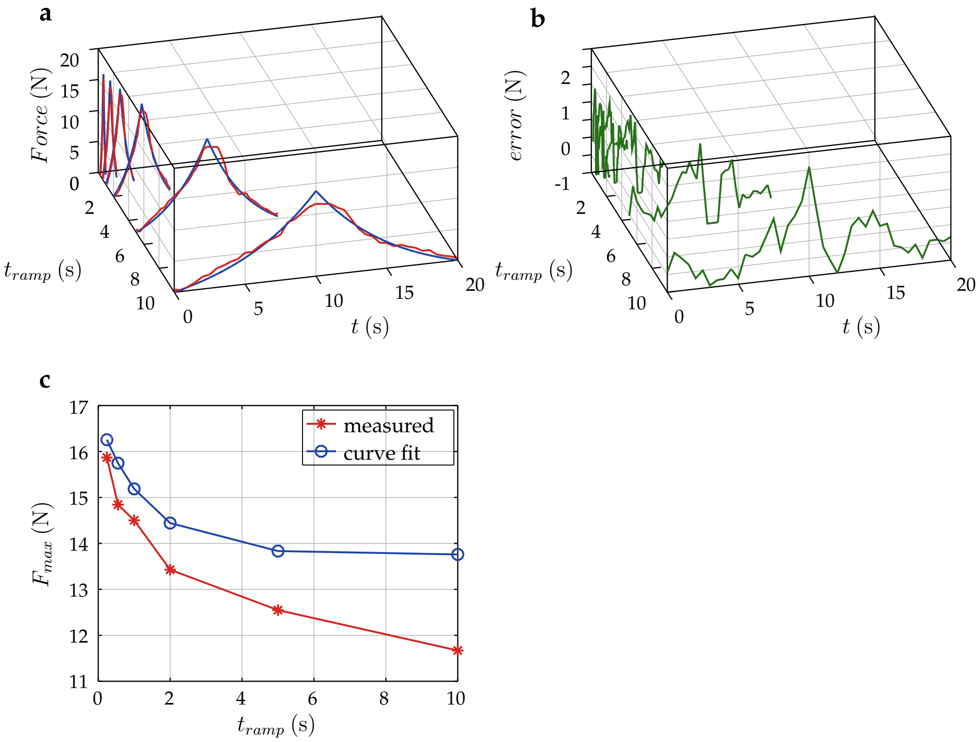

FIGURE 4.16: Curve fit of all tests to model function Eq. 4.22 without $K(t, p_K)$ term, $R^2 = 0.9637$:

a, measured (red) and curve fit force (blue) versus time t and ramp rise time t_{ramp} of the test;

b, error, that is curve fit minus measured force versus time t and ramp rise time t_{ramp} of the test;

c, peak force, measured (red) and curve fit (blue), versus ramp rise time t_{ramp} of the test.

Chapter 5

Simulation of the Papadopoulou Test

5.1 Triangulation, Boundary and Initial Conditions

5.1.1 Triangulation

The finite element model of the specimen, shown in Fig. 5.1, is based on the surface geometry described in Papadopoulou et al. (2013). Net generation was done with 10-node tetrahedron elements. Element type C3D10MP (ABAQUS (2016)), with displacement and pore pressure degree of freedom active at all nodes, modified second-order interpolation of displacement and pore pressure and with hourglass control was used. For the purpose of this work, element quality of the surface model was further improved and domains were then meshed with a lower growth rate for element length from the surface to the centre of the domain. In this way, starting from the surface, layers of approximately $0.5\,\mathrm{mm}$ thickness were generated. A cortical bone thickness of $2\,\mathrm{mm}$ and an alveolar bone thickness of $0.5\,\mathrm{mm}$ was assumed and material properties were assigned to the corresponding layers. Smooth transition from cortical to cancellous bone was modelled by means of assigning the average property of cortical and cancellous bone to the 4^{th} cortical element layer. Cancellous bone properties were assigned to the remaining part of the bone domain.

The tooth domain was not differentiated into enamel, dentine, pulp and cementum. Here, the tooth is loaded in bending, and the pulp is close to the neutral axis of bending. Therefore, variation of pulp stiffness has a small effect on the overall tooth stiffness, and the assumption of a homogeneous tooth domain, which was also used in previous investigations (e.g. Papadopoulou et al. (2013)), is considered justified.

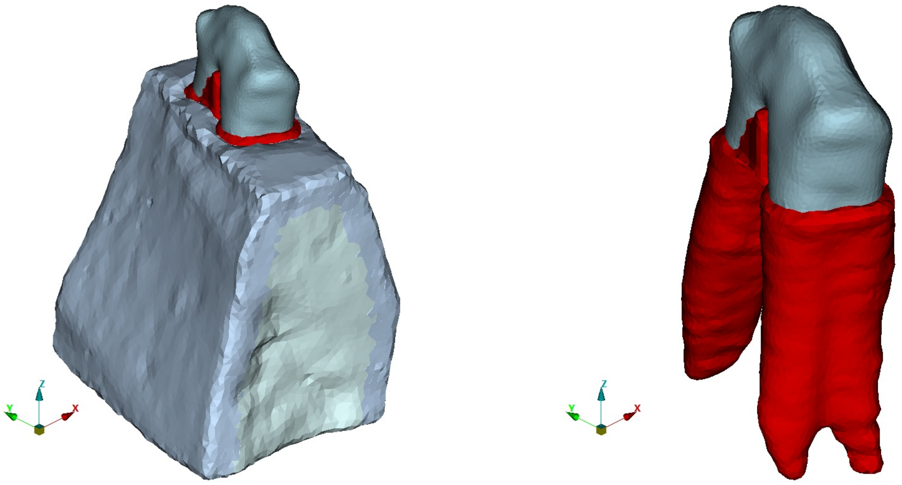

(A) Specimen (B) Tooth and PDL

FIGURE 5.1: Finite element model of the specimen.

5.1.2 Boundary Conditions

The lower third part of the mandible specimen was embedded in an acrylic resin during experimentation and fixed to the test bed. This was represented with Dirichlet boundary conditions for displacements at the corresponding surface. The acrylic resin prevents fluid flow. This was represented with Neumann boundary conditions for pressure at the affected surface.

Actuator displacement was applied to a reference point at the same position as the centre of the actuator contact surface in the experiment. The accuracy of the reference point position was within $0.1\,\mathrm{mm}$ of the test setup (Papadopoulou et al. (2013)). Nodes at the tooth surface within the contact area of the actuator were coupled to the reference node with multi point constraints.

5.1.3 Initial Condition - Void Ratio

ABAQUS (2016) uses *void ratio* e, defined as the ratio of the volume of voids to the volume of solid material, instead of porosity n. Recalling that porosity is the ratio of void volume to total volume, conversion of porosity in Tab. 5.1 to void ratio is given by $e = n/(1-n)$. The void ratio at the nodes was defined as initial condition. At the interfaces between domains, e.g. between PDL and alveolus, the average value of affected domains was used.

5.1.4 Initial Condition - Pore Pressure

Pore pressure calculated is the variation with respect to ambient pressure. Therefore initial value of pore pressure was set to zero.

5.2 Material Properties

Continuum models of bone have been subject of extensive research. For a thorough review refer to the papers of Cowin (1999) and Oftadeh et al. (2015), the edited volume of Cowin (2001) and the textbook of Cowin and Doty (2007). At the macroscopic scale two major forms of bone tissue are distinguished. The first is called *cortical bone*, which is a relatively dense, compact material, that forms most of the outer shell of the bone. At microscopic scale, adult cortical bone tissue can be lamellar, osteonal or woven. The second is called *cancellous bone*, also referred to as trabecular bone or spongy bone. It is generally found within the confines of cortical bone. Cancellous bone is built up of short struts of bone material, the so-called trabeculae. These are interconnected and give the material a spongy appearance. Both, cortical and cancellous bone possess porosity and corresponding permeability and according to Cowin and Doty (2007), 'The isotropic small strain, compressible poroelastic model is an appropriate model for the study of bone fluid movement and bone fluid pressures.'

5.2.1 Mandible - Cortical Bone

Citing Cowin and Doty (2007), Chap. 11.5, 'A visual inspection of cortical bone tissue suggests that, like a tree, it has shape-intrinsic orthotropic elastic symmetry. The degree of textured anisotropy of bone tissue also varies with anatomic site (and from individual to individual); thus, some cortical bone tissue might be transversely isotropic, or even isotropic.'

For the specimen of the Papadopoulou et al. (2013) test no information of trabeculae orientation is available. Further the focus of the present investigation is not on the micro structural behaviour of the trabeculae. At macroscopic scale, isotropic material behaviour is deemed appropriate and was assumed for cortical bone of the mandible. Poroelastic constants were taken from Cowin and Doty (2007), Chap. 11.6, in particular: Young's modulus $E = 14.58\,\mathrm{GPa}$, Poisson's ratio $\nu_s = 0.325$, Lacunar–Canalicular porosity $n = 0.05$, intrinsic permeability $k = 1.47 \cdot 10^{-20}\,\mathrm{m}^2$ and fluid viscosity $\mu = 1.0 \cdot 10^{-3}\,\mathrm{Pa\,s}$.

5.2.2 Mandible - Cancellous Bone

For human mandibular condyle Renders et al. (2007) measured cancellous bone porosity with cubic specimens of edge length $4\,\mathrm{mm}$ taken from the centre of the condyle. They reported a porosity of $n = 0.793 \pm 0.051$. To the best knowledge of the author, sound values of cancellous bone porosity and permeability for the human mandible in the vicinity of the alveolus have not been published to date. Due to the size of the mandible, the minimum specimen size necessary and observed variation of the spongy appearance of mandible sections direct measurement is deemed not feasible.

According to Cowin (2001), 'The published values of permeability of cancellous bone range over three orders of magnitude and depend strongly on porosity and anatomical site.' Observed porosity in Cowin (2001), Fig. 25.3, ranges from 0.30 to 0.95 and at a porosity of 0.8 measurements of human femoral neck, human calcaneus and bovine proximal tibia are depicted. For these data, intrinsic permeability is readily available from Eq. 25.22 and Eq. 25.23 in Cowin (2001) and the intrinsic permeability, with porosity rounded to one significant digit $n = 0.8$, is $k = 1.0 \cdot 10^{-9}\,\mathrm{m}^2$. Notice that measured intrinsic permeability, depicted in Cowin (2001), Fig. 25.3, for porosity $n = 0.8$, vary about one order of magnitude. Taking the above mentioned inhomogeneity of the observed spongy appearance of the mandibular section into account, the variations of permeability may be even larger.

The article of Oftadeh et al. (2015), 'highlights the high dependency of the mechanical properties of trabecular bone on species, age, anatomic site, loading direction, and size of the sample under consideration.' and reviews proposed anisotropic, orthotropic, transversely isotropic and isotropic constitutive models based on micro finite element methods and mechanical testing. For the specimen of the Papadopoulou et al. (2013) test no information of trabeculae orientation, which is required for a anisotropic constitutive model, is available. In the present investigation the main focus is not on the micro structural behaviour of the trabeculae. Furthermore, according to Cowin (2001), Chap. 15.7, 'Most of the trabeculae, however, are loaded in compression or bending. For these loading modes, only the longitudinal Young's modulus is of importance. Consequently, the anisotropic tissue material can be well represented as an isotropic material with an "effective" isotropic tissue modulus that represents the longitudinal stiffness of the bone tissue.'

A summary of relations for Young's modulus of cancellous bone is found in Oftadeh et al. (2015), Tab. 2. The relation between apparent density ρ_{app} and effective isotropic tissue modulus E_{mean} of Hodgskinson and Currey (1992), Tab. 2.2, is cited by Cowin (2001), Eq. 15.12, in the form

$$E_{mean} = 0.003715 \cdot {\rho_{app}}^{1.96} \,, \tag{5.1}$$

with ρ_{app} in $\mathrm{kg/m^3}$ and E_{mean} in MPa. The curve fit of Hodgskinson and Currey (1992) used 24 samples, and for the original curve in double logarithmic form, a coefficient of multiple correlation of $R^2 = 0.941$ was reported.

A commonly used parameter to characterise cancellous bone is *bone volume fraction*, defined as bone volume over total volume, $V_v = BV/TV$. With this notation, *apparent density*, also called structural density or bone density, is defined as bone mass per total volume, $\rho_{app} = m_b/TV$ and *tissue density* is defined as bone mass per bone volume, $\rho_{tissue} = m_b/BV$. The relationship between apparent and tissue density becomes

$$\rho_{app} = BV/TV \cdot \rho_{tissue} \,. \tag{5.2}$$

A frequently cited value for the tissue density of human cancellous bone is $1.874\,\mathrm{g/cc}$ (Gong et al. (1964)). For above mentioned porosity of $n = 0.8$ and assuming saturation condition is valid, i.e. total volume is bone volume plus void volume, the bone volume fraction is $V_v = 0.2$. With Eq. 5.2 and Eq. 5.1, Young's modulus is than $E_{mean} = 0.41\,\mathrm{GPa}$. This value is well within the range reported in literature, e.g. Oftadeh et al. (2015). Nevertheless it should be kept in mind that the value can vary considerably. Following Cowin (2001), Chap. 15.7, a Poisson's ratio of $\nu = 0.3$ is assumed.

5.2.3 Mandible - Alveolar Bone

Poroelastic constants for alveolar bone, taken from Bergomi et al. (2011), are: Young's modulus $E = 0.345\,\mathrm{GPa}$, Poisson's ratio $\nu = 0.31$ and intrinsic permeability $k = (5.29 \pm 3.81) \cdot 10^{-14}\,\mathrm{m}^2$. Bergomi et al. (2011) stated no values for alveolar bone porosity. After visual inspection of alveolus perforation of mandible specimen, the same porosity as for cancellous bone was assumed, i.e. $n = 0.8$.

5.2.4 Tooth

Material constants for the tooth, taken from Bergomi et al. (2011), are: Young's modulus $E = 15.0\,\mathrm{GPa}$, Poisson's ratio $\nu = 0.31$ and intrinsic permeability $k = (3.88 \pm 3.84) \cdot 10^{-17}\,\mathrm{m}^2$. For porosity the same value as for cortical bone was assumed, i.e. $n = 0.05$.

5.2.5 Periodontal Ligament

Bergomi et al. (2011) used a poro-hyperelastic constitutive model of the PDL, based on a modified version of Ogden's strain energy potential and porosity-dependent permeability, to identify poroelastic constants. They measured a porosity value of $n = 0.70 \pm 0.17$ and identified a intrinsic permeability value at reference configuration of $k = 8.81 \cdot 10^{-15}\,\mathrm{m}^2$. The porosity value $n = 0.70$ was used herein.

5.2.6 Bulk Modulus

The bulk modulus for hard tissue is defined by two elastic constants. For instance, with Young's modulus and Poisson's ratio, by Eq. 2.20.

To set the scene for soft tissue Wells and Liang (2011) is quoted, 'The literature is bereft of data for the bulk modulus of soft tissues. Surprisingly, standard biomechanics textbooks (such as [Fung (1993)]) are almost completely silent in this respect.' Numerous investigators assume incompressibility. For simple geometries, with this assumption some closed form solutions are readily available (see e.g. Rice and Cleary (1976), Holmes and Mow (1990)). This may have contributed to the popularity of the incompressibility assertion.

Sonography is a well established examination method in medicine. For pressure waves, the adiabatic bulk modulus K_a is related to the velocity of sound c and density ρ by equation $K_a = c^2\rho$ (Trendelenburg (1939), Chap. 21). According to the reference book of Duck (1990), Tab. 15.1, the bulk modulus for soft tissues calculated from measurements of the ultrasonic sound velocity and tissue density ranges from about $1.8\,\mathrm{GPa}$ to $2.6\,\mathrm{GPa}$. The bulk modulus of substances accessible to direct measurement, like sea water ($2.34\,\mathrm{GPa}$), paraffin oil ($1.62\,\mathrm{GPa}$) and polypropylene (1.1 to $1.4\,\mathrm{GPa}$) (Kaye and Laby, 1995), are of a similar magnitude. In terms of poroelasticity, adiabatic bulk modulus K_a corresponds to the undrained bulk modulus K_u of the soft tissue. Cowin and Doty (2007), Chap. 11.6, argue that, 'In the case of soft tissues the bulk moduli of the soft tissue matrix and the pore water are almost the same ... Thus, for soft tissues the incompressibility assumptions of the fluid and solid constituents are a reasonable approximation.' With the first argument the bulk modulus of the periodontal ligament solid matrix would be in the order of magnitude of $2.2\,\mathrm{GPa}$.

5.2.7 Permeability

The intrinsic permeability k (units m^2) assumed for the different domains is listed in Tab. 5.1. Permeability in ABAQUS (2016) is consistent with Darcy's permeability constant, today commonly referred to as *hydraulic conductivity* K (units $\mathrm{m/s}$). Another term frequently used is *coefficient of permeability*, defined as $\kappa = k/\mu$ (units $\mathrm{m^3 s/kg}$), where μ is the dynamic viscosity of the fluid. The relation between these constants is (Cowin (2001), Eq. 25.3)

$$K = \frac{k\rho g}{\mu} = \kappa\rho g \, , \tag{5.3}$$

where ρ is the density of the interstitial fluid and g is the acceleration of gravity. Here, the value at see level, $g = 9.807\,\mathrm{m/s^2}$, was assumed.

In biomechanics permeability is commonly estimated by virtue of Eq. 2.64, i.e. the coefficient of permeability κ is calculated from measurement of the pressure gradient across the specimen and the volume flux (e.g. Bergomi et al. (2011)). A measurement of the dynamic viscosity and density of the fluid is not required. Permeability in ABAQUS (2016) is defined by specifying the hydraulic conductivity K and the *specific weight* $\gamma = \rho g$. It is evident from the discrete version of Eq. 2.64, that the coefficient of permeability κ is relevant for simulation. Hence, the specific weight γ, specified in conjunction with the hydraulic conductivity K, cancels out and is merely a means to define the coefficient of permeability κ.

5.2.8 Interstitial Fluid

In accordance with Cowin and Doty (2007), Tab. 11.3, and Bergomi et al. (2011), who conducted tests with specimens that were fully immersed in physiological saline at ambient temperature and pressure, a dynamic viscosity of $\mu = 1.0 \cdot 10^{-3}\,\mathrm{Pa\,s}$ is assumed. For values taken from Bergomi et al. (2011), the specific weight stated therein, $\gamma = 9965\,\mathrm{N\,m^{-3}}$, is used. For the remaining domains, density of physiological saline solution ($9\,\mathrm{g}$ NaCl per litre) at ambient temperature ($22\,^\circ\mathrm{C}$) is assumed, i.e. $\rho = 1.0046 \cdot 10^3\,\mathrm{kg/m^3}$ (McCutcheon et al. (1993)).

Regarding compressibility Cowin and Doty (2007), page 359, is adopted, 'The bulk modulus for salt water is $2.3\,\mathrm{GPa}$, and it is assumed that bone fluid has this bulk modulus.'

5.2.9 Summary

A summary of poroelastic constants used for mandible and tooth is found in Tab. 5.1.

TABLE 5.1: Summary of Poroelastic Constants used for Mandible and Tooth.

Property		Units	Cortical Bone	Cancellous Bone	Alveolar Bone	Tooth
Young's Modulus	E	GPa	14.58	0.41	0.345	15.0
Poisson's Ratio	ν	–	0.325	0.3	0.31	0.31
Intrinsic Permeability	k	m^2	$1.47 \cdot 10^{-20}$	$1.0 \cdot 10^{-9}$	$5.29 \cdot 10^{-14}$	$3.88 \cdot 10^{-17}$
Porosity	n	–	0.05	0.8	0.8	0.05

5.3 Static Analysis

5.3.1 Linear Elastic Constitutive Model

A geometric nonlinear analysis, with linear elastic material behaviour, was performed. For estimation of the tangent stiffness an actuator displacement of $0.01\,\mathrm{mm}$ and for estimation of the secant stiffness an actuator displacement of $0.2\,\mathrm{mm}$ was applied as a ramp function at the reference node. The corresponding reaction force was evaluated. As a target for the reaction force, the static value of the model function Eq. 4.20, with parameters from Tab. 4.8, was used. A parametric study was conducted, with Poisson's ratio ranging from 0.15 to 0.45 in steps of 0.05 and a initial Young's modulus of $0.5\,\mathrm{MPa}$. For the next iteration, Young's modulus was scaled according to the ratio of target and calculated reaction force value from the current iteration. After a few iterations the reaction force matched the target value to four digits. Figure 5.2 shows a plot of the tangent and secant reaction force curve. Poisson's ratio, tangent and secant Young's modulus of the final iteration and corresponding tangent and secant bulk modulus, calculated with Eq. 2.20, are given in Tab. 5.2.

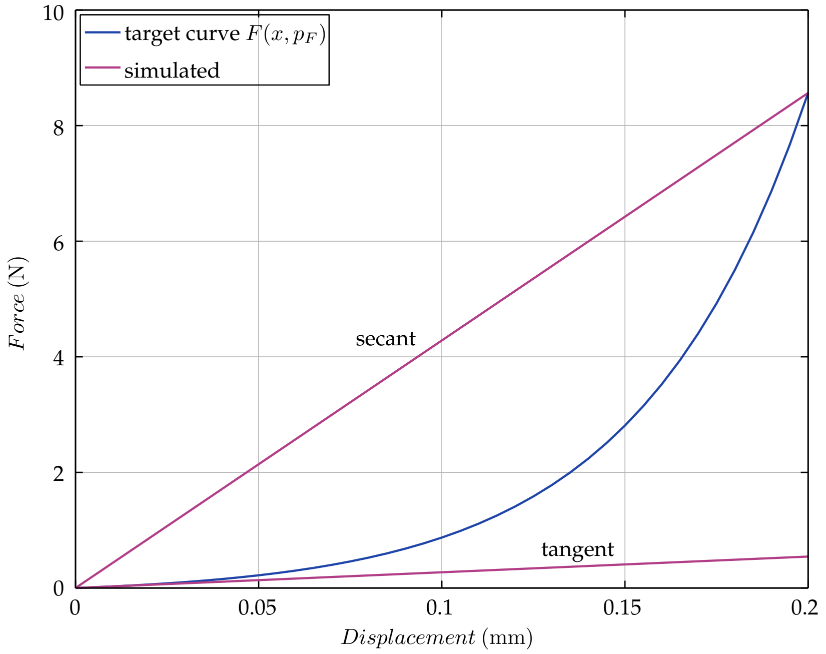

FIGURE 5.2: Reaction force versus actuator displacement of target curve (blue) and simulated response (magenta) with linear elastic constitutive model.

TABLE 5.2: Static linear elastic analysis: Young's modulus, Poisson's ratio of final iteration and corresponding bulk modulus.

Young's modulus MPa		Poisson ratio –	bulk modulus MPa	
tangent	secant		tangent	secant
0.0568	0.967	0.15	0.0270	0.460
0.0564	0.962	0.20	0.0314	0.534
0.0552	0.941	0.25	0.0368	0.628
0.0527	0.900	0.30	0.0439	0.750
0.0484	0.828	0.35	0.0538	0.919
0.0412	0.706	0.40	0.0686	1.18
0.0288	0.497	0.45	0.0961	1.66

5.3.2 Hyperelastic Model for Compressible Material - Storåkers Model

A geometric nonlinear analysis, with the hyperelastic constitutive model for compressible material described in Chap. 2.1.2, was performed. The strain energy density function, Eq. 2.3, was used with one term, i.e. $N = 1$. With that, three material parameters, μ, α and β are unknown. The actuator displacement $d_{ramp} = 0.2\,\mathrm{mm}$ was applied as a ramp function at the reference node and the corresponding reaction force was evaluated. As target for the reaction force curve, the static part of the model function Eq. 4.20, with parameters from Tab. 4.8, was used. The difference between target force and calculated reaction force is a measure of the error e and should be minimal with respect to a suitable norm $\|\;\|$. With that the problem can be stated as

$$\text{find} \quad \mu, \alpha, \beta \in \mathbb{R}_{>0} \qquad \text{such that} \quad \|e\| = min\,. \tag{5.4}$$

A parametric study was conducted to identify the material parameters. Recalling Chap. 2.1.2, with $N = 1$ the first parameter μ is identical to the initial shear modulus. Considering the linear elastic response and static target curve in Fig. 5.2, the initial shear modulus must be considerably smaller than the secant Young's modulus identified in Chap. 5.3.1 and larger than zero. Therefore the parameter μ was varied from 0.02 to 0.05 in steps of 0.01. The second parameter α must be larger than one for a progressive characteristic. The parameter α was varied from 10 to 40 in steps of 10. The third parameter β is related to Poisson's ratio ν, which must be greater than zero and smaller than 0.5. In the parameter study ν was varied from 0.1 to 0.4 in steps of 0.1. The chosen parameter values resulted in $4^3 = 64$ parameter combinations and the study was executed and evaluated with parametric study utilities of ABAQUS (2016). Exemplary reaction force curves are shown in Fig. 5.3. The target curve is in the range spanned by parameter combination 1, with all parameters at smallest level, and parameter combination 64, with all parameters at largest level. Several parameter combinations resulted in reaction force curves which intercepted the target curve. This was deemed unfavourable, since it indicates a low initial slope followed by an excessive progression or vice versa. Reaction force curves that came closest to the target curve without intercepting were parameter combination 11 ($\mu = 0.04$, $\alpha = 30$ and $\nu = 0.1$) as lower and parameter combination 43 ($\mu = 0.04$, $\alpha = 30$ and $\nu = 0.3$) as upper bound.

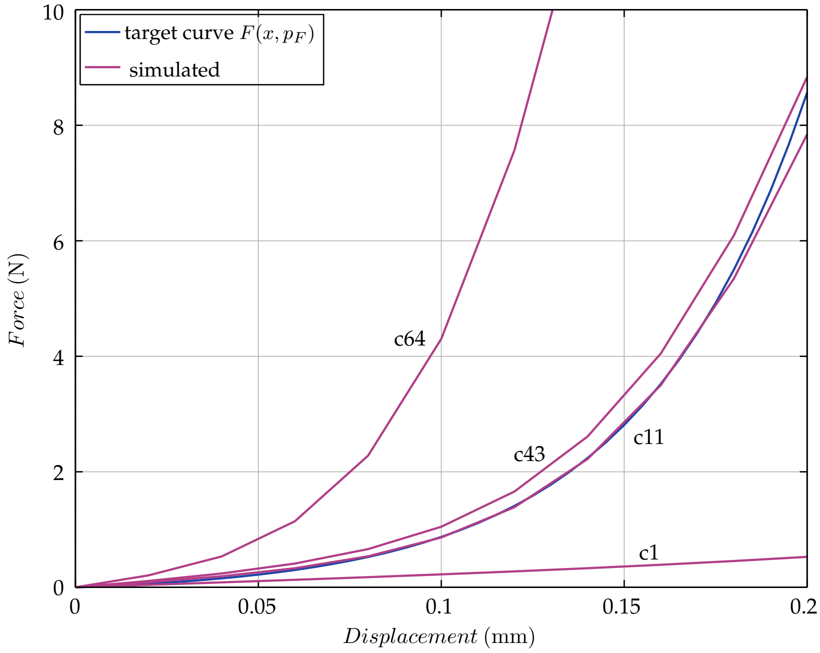

FIGURE 5.3: Reaction force versus actuator displacement of target curve (blue) and simulated response (magenta) with Storåkers constitutive model and parameter combination 1, 11, 43 and 64.

Further the error, i.e. calculated reaction force minus target force, was evaluated for actuator displacement 0.1 and $0.2\,\mathrm{mm}$ and the mapping $\mathbb{R}^3_{>0} \mapsto \mathbb{R}^2$, that is the mapping from the parameters to the errors, was considered. Based on the region identified with the parameter study, parameter intervals were refined and the corresponding errors were estimated by means of optimal interpolation (Ref. Barth et al. (2008)) implemented in the Octave *optiminterp* function. Compared to a finite element analysis this considerably reduced computational cost.

The parameters identified by means of optimal interpolation are $\mu = 0.0337$, $\alpha = 31.68$ and $\nu = 0.238$ and the corresponding errors estimated are smaller than $0.001\,\mathrm{N}$.

Based on the parameters identified, a second parameter study was conducted. The last significant digit of each parameter was incremented and decremented three times by one unit and the parametric study was executed and evaluated with parametric study utilities of ABAQUS (2016). The parameter combination with lowest error was $\mu = 0.0338$, $\alpha = 31.68$ and $\nu = 0.236$. The corresponding error is smaller than $0.001\,\mathrm{N}$ at actuator displacement $0.1\,\mathrm{mm}$ and $0.2\,\mathrm{mm}$. Around actuator displacement $0.18\,\mathrm{mm}$ a deviation of $0.2\,\mathrm{N}$ is observed (Fig. 5.4). The stress-strain curve for uniaxial loading according to Eq. 2.4, with Storåkers constitutive model and parameters identified, is shown in Fig. 5.5.

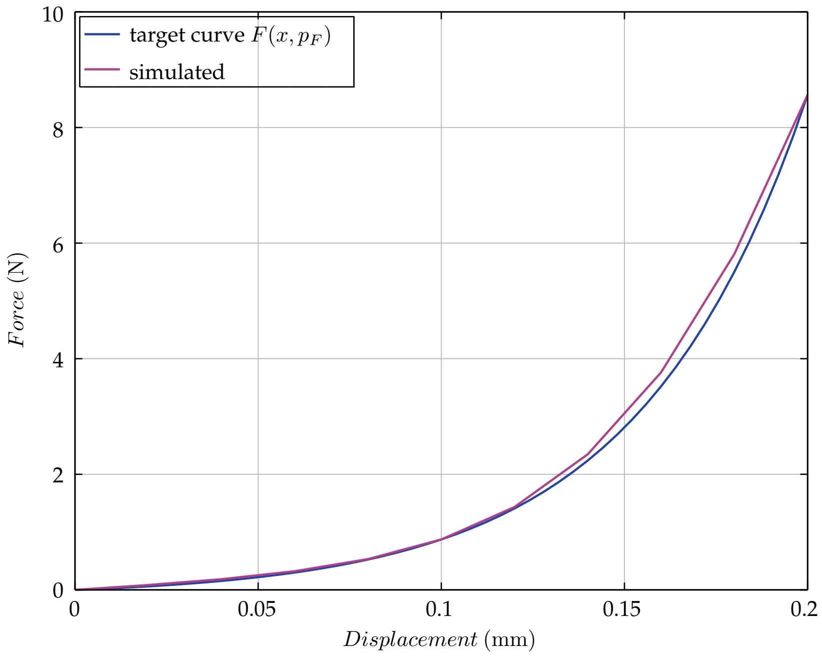

FIGURE 5.4: Reaction force versus actuator displacement for target curve (blue) and simulated response (magenta) with Storåkers constitutive model and final parameters $\mu = 0.0338$, $\alpha = 31.68$ and $\nu = 0.236$.

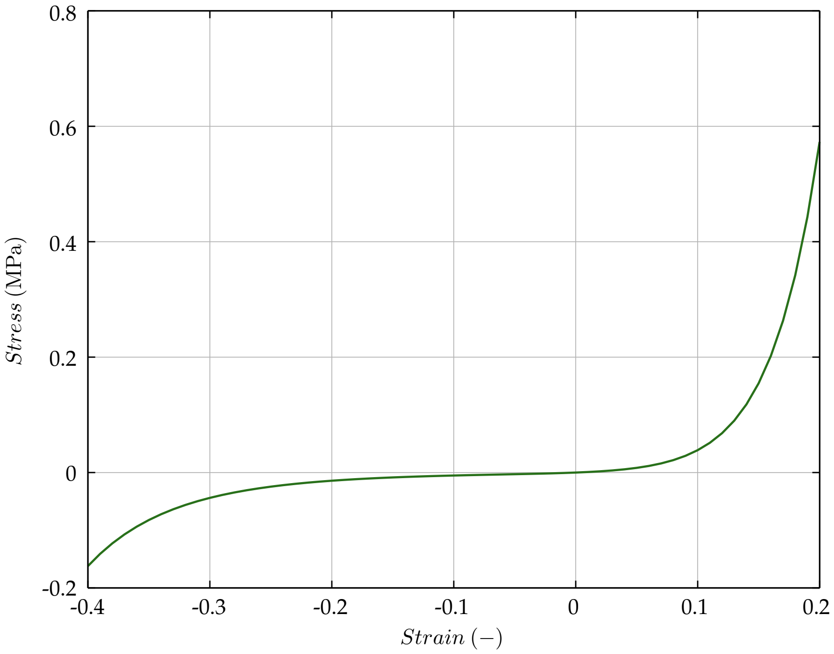

FIGURE 5.5: Stress versus strain for an uniaxial load according to Eq. 2.4 and Storåkers constitutive model with final parameters $\mu = 0.0338$, $\alpha = 31.68$ and $\nu = 0.236$.

5.3.3 First-Invariant Hyperelastic Model - Marlow Model

Recall from Chap. 2.1.3, that for uniaxial tension the strain energy density function Eq. 2.12 will reproduce the measured stress-strain response used in the integral precisely. Since measured stress strain data are not available, it is assumed that there is a mapping of the actuator displacement versus target force curve to the strain versus stress curve of the PDL. At zero actuator displacement the reaction force is zero and this corresponds to the zero strain and stress point. A candidate for the mapping is to assume that strain ε is proportional to actuator displacement x, and stress σ is proportional to the target force F, given by the static part of the model function Eq. 4.20, with parameters from Tab. 4.8.

For a chosen mapping and corresponding stress - strain curve, the reaction force is calculated with a geometric nonlinear analysis, using the Marlow constitutive model and actuator displacement $d_{ramp} = 0.2\,\mathrm{mm}$, applied as a ramp function at the reference node. It was assumed that Poisson's ratio is identical to the value identified in Chap. 5.3.2. The difference between target force and calculated reaction force is a measure of the error e and should be minimal with respect to a suitable norm $\| \ \|$. With that the problem can be stated as:

$$\text{find} \quad a, b \in \mathbb{R}_{>0} \quad (F, x) \mapsto (\sigma, \varepsilon) = (aF, bx) \qquad \text{such that} \quad \|e\| = min\,. \tag{5.5}$$

The minimisation problem Eq. 5.5 can be split in two parts. With assumed initial values for a and b the model is simulated. First, for a fixed value of b, that is for fixed strain mapping, the value of a is multiplied by the ratio of the target to calculated reaction force at actuator displacement $d_{ramp} = 0.2\,\mathrm{mm}$, the stress mapping is updated with the new a value and the model is simulated again. The first step is repeated until the calculated reaction force at actuator displacement $d_{ramp} = 0.2\,\mathrm{mm}$ is within specified error tolerance[1]. Second, in an outer loop, the value of b is varied and the first step is repeated, until the calculated reaction force at actuator displacement $d_{ramp} = 0.1\,\mathrm{mm}$ is within specified error tolerance. The bisection method was used for the variation of b.

Considerable computational cost can be saved with reasonable initial values. The test was non-destructive. Therefore the upper strain limit should be well below ultimate strain, say roughly $\varepsilon_{max} < 0.3...0.4$, corresponding to $b < 2$. The numerical value of the maximum target reaction force is higher than ultimate stress reported in e.g. Toms et al. (2002), hence $a < 1$.

An ABAQUS (2016) CAE Python script was written to carry out the described minimisation algorithm. An error limit of $0.001\,\mathrm{N}$ was used at actuator displacement $0.1\,\mathrm{mm}$ and $0.2\,\mathrm{mm}$, and parameters found are $a = 0.0274044, b = 1.19350$. Figure 5.6 shows the corresponding reaction force curve. Around actuator displacement $0.18\,\mathrm{mm}$ a deviation of $0.1\,\mathrm{N}$ is observed. The respective stress versus strain curve of Marlow constitutive model is shown in Fig. 5.7.

---

[1] The first, inner loop converges against the target force at actuator displacement $d_{ramp} = 0.2\,\mathrm{mm}$. Since the model consists of various domains with different material properties, several iterations are necessary. This can be attributed to the various domain stiffness arranged in series. For a model with only one (Marlow) domain the reaction force would be exact after one iteration. This is because Eq. 2.12 is homogeneous.

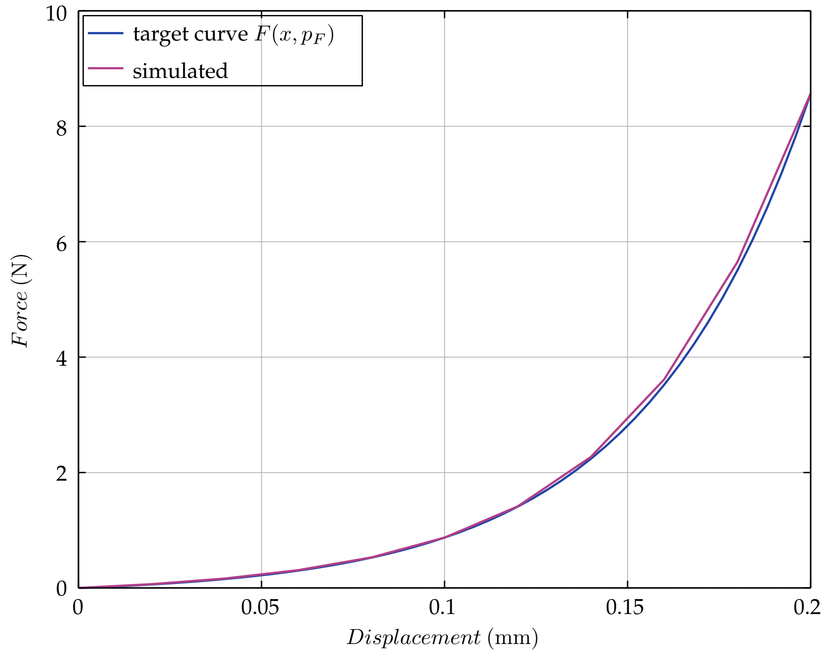

FIGURE 5.6: Reaction force versus actuator displacement of target curve (blue) and simulated response (magenta) with Marlow constitutive model and parameters of Eq. 5.5 $a = 0.0274044$ and $b = 1.19350$.

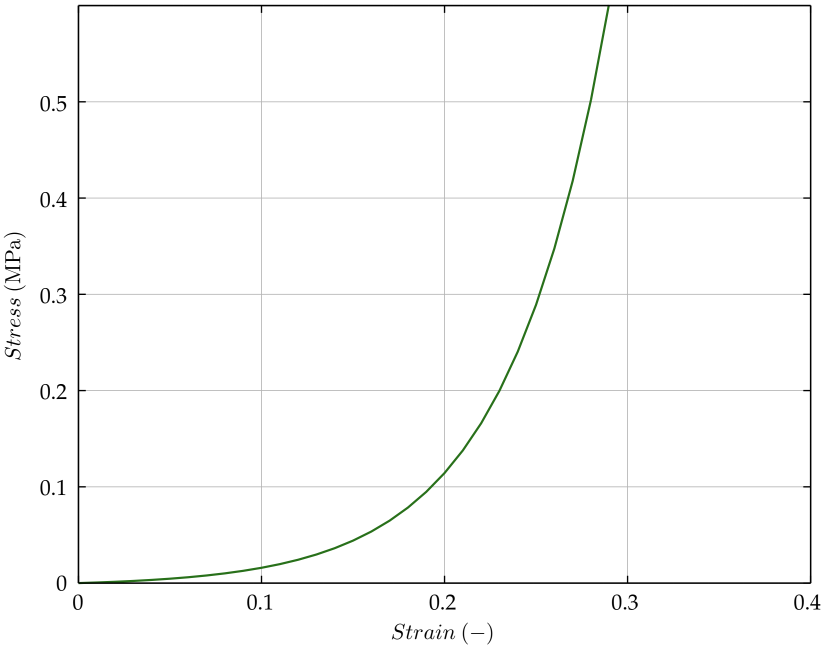

FIGURE 5.7: Stress versus strain of Marlow constitutive model, with parameters of Eq. 5.5 $a = 0.0274044$ and $b = 1.19350$.

5.3.4 Discussion - Constitutive Model

With the linear elastic constitutive model, the reaction force versus actuator displacement curve was estimated that passes through the zero point and the target force at actuator displacement $0.01\,\mathrm{mm}$ and $0.2\,\mathrm{mm}$ (Fig. 5.2). Therefore, corresponding Young's modulus estimated can be considered as a tangent and secant modulus respectively.

Considering Tab. 5.2, we observe that the Young's modulus found depends on the Poisson's ratio. Young's modulus decreases and Bulk modulus increases with increased Poisson's ratio. Based on this analysis, without further information, it is not possible to deduce on the valid Young's modulus. Often investigators assume a Poisson's ratio and state the corresponding Young's modulus. If the Poisson's ratio is not based on direct measurements this approach is questionable.

The shear modulus can be estimated from Young's modulus in Tab. 5.2 and Eq. 2.16. For the Poisson's ratio $\nu = 0.236$, identified with the Storåkers model, the tangent shear modulus is $G = 0.0344\,\mathrm{MPa}$. This value is slightly larger than the value identified with the Storåkers model $\mu = G = 0.0338\,\mathrm{MPa}$. It is anticipated that the tangent shear modulus estimated would approach the value identified with Storåkers model, if the second point used for tangent approximation, i.e. actuator displacement $0.01\,\mathrm{mm}$, approaches the zero point.

Both, the Storåkers and the Marlow hyperelastic constitutive model identified reproduce the target force curve accurately. The parameters of model function, Tab. 4.8, were optimised for actuator displacement $0.1\,\mathrm{mm}$ and $0.2\,\mathrm{mm}$. The difference between target force and calculated reaction force, i.e. the error, at these points is smaller than $0.001\,\mathrm{N}$. At actuator displacement $0.18\,\mathrm{mm}$ a deviation of $0.2\,\mathrm{N}$ is observed for the Storåkers model and a deviation of $0.1\,\mathrm{N}$ is observed for the Marlow model.

For the Marlow model the deviation at $0.18\,\mathrm{mm}$ is presumably due to the nonlinearity introduced by the domain stiffness arranged in series. For only one domain the Marlow model would reproduce the stress-strain response precisely. For the Storåkers model the deviation at $0.18\,\mathrm{mm}$ is slightly larger. Observe that the corresponding strain energy density function, Eq. 2.3, dependence on strain invariants is in polynomial form, the target curve is however a exponential function. This may explain the slightly larger deviation compared to the Marlow model. If a polynomial function were chosen to represent the static part of the model function the fit of the Storåkers model should further improve. Concluding, the slightly larger deviation of the Storåkers model at actuator displacement $0.18\,\mathrm{mm}$ may be considered as artefact and should not be used as argument to prefer one model over the other.

In terms of computational cost the Marlow model was $1.8\,\%$ more expensive than the Storåkers model. In Chap. 2.1.3 we have seen that for the Marlow model stretches are mapped to an equivalent stretch, which involves additional computations and may explain the slightly increased computational cost.

Considering the mode of deformation of the periodontal ligament, regions of compression and tension are observed. The Marlow model maps both, compression and tension stretches to an equivalent tension stretch with corresponding stress. The stress-strain curve identified for the Marlow model reproduces the target force curve well. However the stress-strain curve is an average curve and estimated stress may deviate from the actual compression or tension stress in the periodontal ligament. In contrast Storåkers model involves no mapping of the stretches. Stress is estimated directly from the strain energy density function, with parameters identified to match both, compression and tension region. On these grounds Storåkers model was chosen for subsequent analysis.

The parameters identified for the Storåkers constitutive model, $\mu = G = 0.0338$ and $\nu = 0.236$, and Eq. 2.16 and 2.20, lead to the bulk modulus $K = 0.365\,\mathrm{MPa}$. This is four orders of magnitude lower than the adiabatic bulk modulus for soft tissue, $K = 2.2\,\mathrm{GPa}$, deduced in Chap. 5.2.6. The adiabatic bulk modulus values for soft tissue are based on measurements of the ultrasonic sound velocity and tissue density. They represent the bulk modulus of the soft tissue as a whole. Taking into account porosity and bulk modulus of the interstitial fluid, the adiabatic bulk modulus values for soft tissue deduced may be dominated by the interstitial fluid contribution. The result presented in this Chapter for the Storåkers model, in particular the Poisson's ratio of $\nu = 0.236$ identified, does not support the incompressibility assertion, which is equivalent to $\nu = 0.5$.

As a final remark, based on harmonic tension–compression tests at 0.1, 0.5 and $1\,\mathrm{Hz}$ on hydrated bovine periodontal ligament, with cylindrical specimen of diameter $(5.8 \pm 0.1)\,\mathrm{mm}$, Bergomi et al. (2011) reported values for the Storåkers model of $\mu = 0.03$, $\alpha = 20.9$ and $\nu = 0.257$. These are in good agreement with the values identified here, i.e. $\mu = 0.0338$, $\alpha = 31.68$ and $\nu = 0.236$. In particular μ, which can be interpreted as the initial shear modulus, and ν, the Poisson's ratio, are in good agreement. A larger difference is observed for the exponent α, which primarily controls the progression of the stress-strain curve. Bergomi et al. (2011) used a poroelastic simulation, with Storåkers constitutive model. The transient part of the response is governed by Darcy's Law and the long term response is determined by hyperelastic part. Therefore, their values identified for the Storåkers model are related to the long term response. On the contrary, the values for the Storåkers model identified here are related to the instantaneous response of the visco-hyperelastic model. This may explain the difference in the exponent α observed.

5.4 Visco-Hyperelastic Analysis

5.4.1 Transient Response

A transient static, geometric nonlinear simulation with visco hyperelastic material was performed. Storåkers constitutive model, with parameters identified in Chap. 5.3.2, was used. For viscoelastic material definition the corresponding curve fit parameters from Tab. 4.8 and option *instantaneous moduli* was used[2]. Model parameters are listed in Tab. 5.3, No. 1. The actuator displacement was applied as a ramp function at the reference node, according to Eq. 4.1, and the resulting reaction force was evaluated.

As a target for the reaction force the viscoelastic part of the model function Eq. 4.20, with parameters from Tab. 4.8, was used. The coefficient of multiple correlation of the viscoelastic target force with respect to measured data is $R^2 = 0.8386$. This value is lower than reported in Tab. 4.8, because the ramp rise time term, $H(x, p_H)$ and the prior load history term, $K(t, p_K)$, which are not part of the viscoelastic model, were omitted.

Figure 5.8 shows a plot of the viscoelastic target force, labelled *curve fit*, and the simulated response. The simulated response accords with principle trends of the target curve, however simulated response shows a higher force level, in particular for actuator displacement $0.2\,\mathrm{mm}$. The coefficient of multiple correlation of the simulated response with respect to the viscoelastic target force is $R^2 = 0.6639$.

Derivation of the target curve assumed a spatially homogeneous stress distribution. This would hold for a specimen loaded in simple tension. In the in vitro test of Papadopoulou et al. (2013) the tooth was loaded in lateral direction, resulting in regions of compression and tension in the periodontal ligament. Therefore a spatially inhomogeneous stress distribution is observed, which may explain the difference in target and simulated response.

In order to improve accordance of simulated to target response a parameter study was conducted. The difference between the viscoelastic target force and

---

[2] ABAQUS (2016) code used for viscoelastic material definition:

```
*HYPERFOAM, N=1, MODULI=INSTANTANEOUS
  <my>,  <alpha>,  <ny>
*VISCOELASTIC, TIME=PRONY
  <p4>,  <p4>,  <tau1>
  <p6>,  <p6>,  <tau2>
  <p8>,  <p8>,  <tau3>
```

simulated reaction force is a measure of the error e and should be minimal with respect to a suitable norm $\| \ \|$. With that the problem can be stated as:

$$\text{find} \quad \alpha, p_4, p_6, p_8 \in \mathbb{R}_{>0} \quad \text{such that} \quad \|e\| = min\,. \tag{5.6}$$

Parameters chosen for the study are the constants that determine the weighting of the viscoelastic elements, that is p_4, p_6 and p_8, as well as exponent α of the Storåkers constitutive model.

Considering Fig. 5.8, it is clear that there should be a higher weight on the first viscoelastic term with lowest time constant, that is p_4 should increase. Again, the equality constraint Eq. 4.10 holds and the long term response is determined by $p_3 = 1-(p_4+p_6+p_8)$, which must be greater than zero[3]. This limits the admissible parameter combinations of p_4, p_6 and p_8. A preliminary study showed, that for a balanced long term response between actuator displacement $0.1\,\mathrm{mm}$ and $0.2\,\mathrm{mm}$ tests, α should decrease. As a measure for the error the coefficient of multiple correlation, R^2, between the viscoelastic target force and simulated reaction force, was used ($\|e\| \to 0^+$ for $R^2 \to 1^-$). In addition the error of all tests at the time when the peak force occurred t_{Fmax}, at the test finish time t_{max} and at an intermediate time was evaluated.

To solve the minimisation problem Eq. 5.6, the same approach as described in Chap. 5.3.2 was used. That is, for selected parameter combinations the response was simulated. In the region where the error was minimal a refined parameter study was conducted by means of optimal interpolation (Ref. Barth et al. (2008)). The thus found refined parameter region was verified by simulation.

The final, optimised parameter combination is listed in Tab. 5.3, No. 2 and a plot of the corresponding simulation result is shown in Fig. 5.9. The coefficient of multiple correlation of the simulated response with respect to the viscoelastic target force has improved to $R^2 = 0.9285$. The simulated response follows closer the target curve, in particular the long term response coincides well.

---

[3] In the material definition p_3 is not defined explicitly. It follows from the equality constraint. Ref.: ABAQUS (2016), Theory Manual.

TABLE 5.3: Parameters used for visco hyperelastic simulation with Storåkers constitutive model. R^2 with respect to viscoelastic target force.

No.	μ	α	ν	p_4	τ_1	p_6	τ_2	p_8	τ_3	R^2
-	-	-	-	-	s	-	s	-	s	-
1	0.0338	31.68	0.236	0.239	3.21	0.252	31.1	0.234	372.	0.6639
2	0.0338	29.7	0.236	0.45	3.21	0.20	31.1	0.08	372.	0.9285

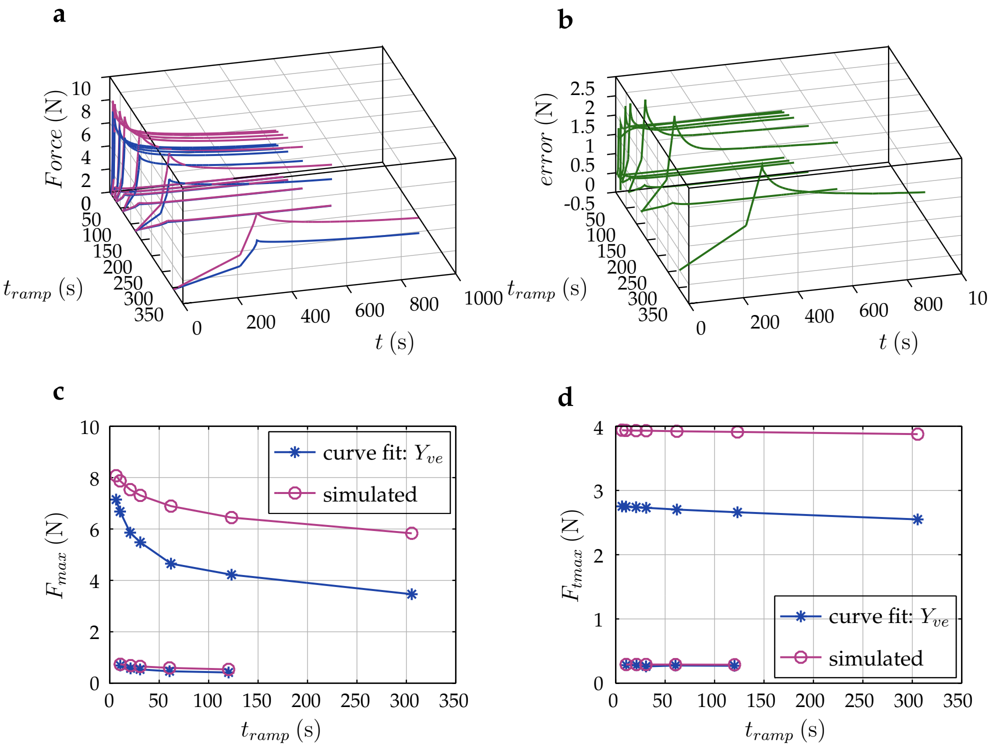

FIGURE 5.8: Viscoelastic Model: Viscoelastic target force, labelled curve fit (viscoelastic part of Eq. 4.20 with parameters from Tab. 4.8) versus simulated force (geometric nonlinear visco-hyperelastic, Storåkers constitutive model, parameters from Tab. 5.3, No. 1). The value $R^2 = 0.6639$ is with respect to the viscoelastic target force. The figures are:

- **a**, curve fit (blue) and simulated (magenta) force versus time t and ramp rise time t_{ramp} of the test;
- **b**, error, that is simulated minus curve fit force versus time t and ramp rise time t_{ramp} of the test;
- **c**, peak force, curve fit (blue) and simulated (magenta), versus ramp rise time t_{ramp} of the test;
- **d**, force at the end of the test, curve fit (blue) and simulated (magenta), versus ramp rise time of the test.

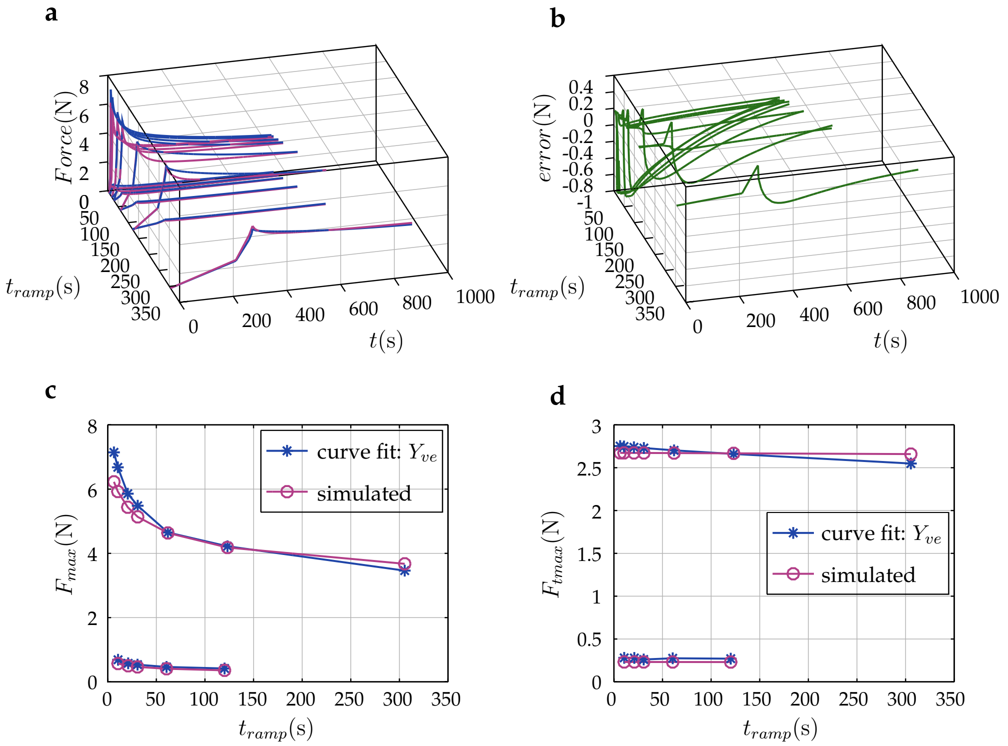

FIGURE 5.9: Viscoelastic Model: Viscoelastic target force, labelled curve fit (viscoelastic part of Eq. 4.20 with parameters from Tab. 4.8) versus simulated force (geometric nonlinear visco hyperelastic, Storåkers constitutive model, parameters from Tab. 5.3, No. 2). The value $R^2 = 0.9285$ is with respect to the viscoelastic target force. The figures are:

- **a**, curve fit (blue) and simulated (magenta) force versus time t and ramp rise time t_{ramp} of the test;
- **b**, error, that is simulated minus curve fit force versus time t and ramp rise time t_{ramp} of the test;
- **c**, peak force, curve fit (blue) and simulated (magenta), versus ramp rise time t_{ramp} of the test;
- **d**, force at the end of the test, curve fit (blue) and simulated (magenta), versus ramp rise time of the test.

5.4.2 Steady State Response

In Chap. 5.3.4, the difference in the Storåkers constitutive model exponent α reported by Bergomi et al. (2011) and given here was mentioned. It was argued that this could be due to the difference in poro-hyperelastic and visco-hyperelastic (with option *instantaneous*) approach used to identify the parameters.

To clarify the issue, the visco-hyperelastic model with Storåkers constitutive equation and parameters from Tab. 5.8, No. 2, was simulated using *static* solution with option *long term*. This is equivalent to the transient steady state solution. Next, the response was simulated using the static solution option *instantaneous*. The long term response is determined by $p_3 = 1 - (p_4 + p_6 + p_8) = 0.27$, whereas for the instantaneous response all terms of the visco-hyperelastic model are used. Therefore, it is obvious that the reaction force increases with option instantaneous. Next, the coefficient α was reduced to achieve the same reaction force at actuator displacement $0.2\,\mathrm{mm}$ as in the first simulation. This was achieved with $\alpha = 20.87$. A plot of the reaction force versus actuator displacement for the three cases is shown in Fig. 5.10.

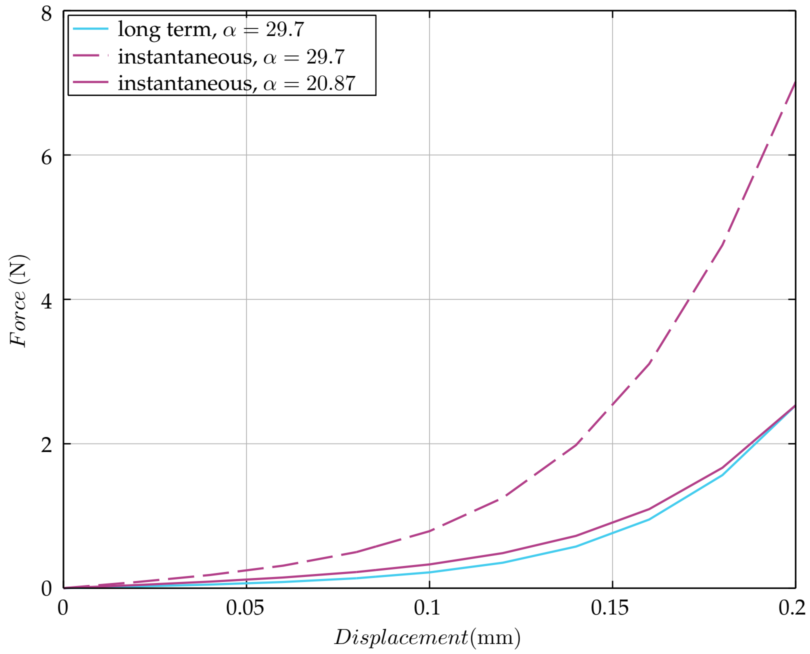

FIGURE 5.10: Visco-hyperelastic material with Storåkers constitutive model ($\mu = 0.0338$, $\nu = 0.236$): steady state response, reaction force versus actuator displacement with *static* solution option *long term* ($\alpha = 29.7$) and *instantaneous* ($\alpha = 29.7$ and $\alpha = 20.87$).

5.4.3 Tooth and Mandibular Bone Stiffness Contribution

Deducing the model function in Chap. 4, an underlying assumption was, that the measured reaction force is dominated by the behaviour of the periodontal ligament. To validate this assumption, the visco-hyperelastic model, with Storåkers constitutive law, was simulated. The simulation was repeated with tooth, mandibular bone, and tooth and mandibular bone successively modelled rigid[4]. The three domains are arranged in series. The stiffness of the specimen c_{vhe}, defined as reaction force divided by actuator displacement of the visco-hyperelastic simulation, has contributions of the tooth c_{tooth}, the periodontal ligament c_{PDL}, and the mandibular bone c_{bone}. As a first approximation, stiffness is estimated from the equation for three springs arranged in series:

$$\frac{1}{c_{vhe}} = \frac{1}{c_{tooth}} + \frac{1}{c_{PDL}} + \frac{1}{c_{bone}} \,. \tag{5.7}$$

This neglects, if present, geometric nonlinear effects and possible interactions of the domains. It is straight forward to estimate the stiffness terms from the four reaction force curves shown in Fig. 5.11. For example, with tooth and mandibular bone rigid, we have $1/c_{tooth} = 1/c_{bone} = 0$, and the contribution of the periodontal ligament c_{PDL}, follows. After estimation of the stiffness terms, total stiffness estimated with Eq. 5.7 was compared to the stiffness obtained directly from the simulation. Deviation was smaller than $4\,\%$ at the peak force, and about $1\,\%$ at the end of the test.

From Eq. 5.7 a *partition of unity* follows, which provides the contribution of each domain to total specimen compliance:

$$1 = \frac{c_{vhe}}{c_{tooth}} + \frac{c_{vhe}}{c_{PDL}} + \frac{c_{vhe}}{c_{bone}} \,. \tag{5.8}$$

This is shown in Fig. 5.11. A linear elastic constitutive model was assumed for tooth and mandibular bone. Therefore, their stiffness is constant. Storåkers constitutive model was assumed for the PDL, which results in a corresponding progressive stiffness characteristic. After the peak force, with constant actuator displacement, the stiffness of the PDL decreases due to stress relaxation. As a consequence, the stiffness of the specimen c_{vhe} decreases, and the contribution of the PDL to the total compliance c_{vhe}/c_{PDL} increases. An increase from about $60\,\%$ to $80\,\%$ is observed in Fig. 5.11. Concluding, the contribution of the PDL

---

[4] ABAQUS (2016) code used for rigid domain definition: `*RIGID BODY, REF NODE=node number, ELSET=element set name`

to the total compliance is dominant, nevertheless, tooth and mandibular bone stiffness have a significant effect on the reaction force. This may contribute to explain the observed difference between target force and simulated response, in Chap. 5.4.1.

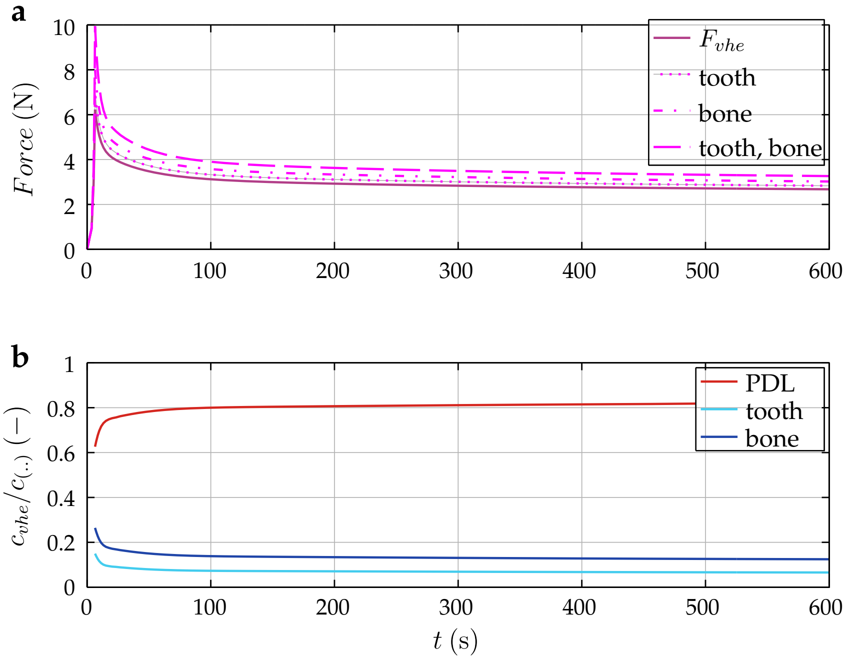

FIGURE 5.11: Visco-hyperelastic response of Test No. 2.:
- **a**, simulated force versus time for baseline F_{vhe}, with rigid tooth, rigid bone, and rigid tooth and bone;
- **b**, compliance contribution $c_{vhe}/c_{(...)}$ of PDL, tooth, and bone.

5.4.4 Discussion - Visco-Hyperelastic Analysis

After parameter optimisation the simulated response matches well the visco-elastic target force curve. Correlation could possibly be further improved, on the expense of computational cost, by including also the time constants in the parameter optimisation. However the discrepancy of the homogeneity assumption in the model function remains. In Chap. 5.4.3 we have seen that the contribution of the PDL to the total compliance is dominant, nevertheless, tooth and mandibular bone stiffness have a significant effect on the reaction force.

To improve the situation two routes are proposed. First, one could try to improve the model function by taking the spacial inhomogeneity and the contribution of tooth and mandibular bone compliance into account. This could be done by series arrangement of springs for the tooth, PDL and bone. In addition the spatial inhomogeneity of the PDL could be modelled by parallel arrangement of several force elements, with suitably reduced displacement input. A priori, the weighting of these force elements and the suitable reduction in displacement input per force element is unknown. The second approach would be to use a co-simulation, where visco-hyperelastic response is simulated and compared to a target force, which is the measured force corrected with the ramp rise time term $H(x, p_H)$ and the prior load history term $K(t, p_K)$. Since these terms contain parameters of the simulation model, the target force has to be updated for each parameter combination. The second approach is computationally expensive, however spacial inhomogeneity is taken into account correctly.

One may argue to identify the parameters of the simulated visco-hyperelastic response with respect to measured force directly, that is, to neglect the ramp rise time term $H(x, p_H)$ and the prior load history term $K(t, p_K)$. This would disregard the effect of the ramp rise time, respectively the ramp velocity, identified in Chap. 4.1.5. A visco-hyperelastic simulation cannot depict this effect[5]. As a consequence, the coefficient of multiple correlation is anticipated to be poor, presumably lower than the value in Tab. 4.4, that was for actuator displacement $d_{ramp} = 0.2\,\mathrm{mm}$ only.

As a final remark, as suspected in Chap. 5.3.4, the different exponents of the Storåkers constitutive model reported can be explained by the difference in poro-hyperelastic and visco-hyperelastic (with option *instantaneous*) approach used to identify the parameters. To reiterate the point, in the poro-hyperelastic simulation by Bergomi et al. (2011), the transient part of the response is governed by Darcy's Law and the long term, steady state response is determined by the hyperelastic part. The values for the Storåkers model identified here are related to the instantaneous response. In fact, the exponent $\alpha = 20.87$, identified with visco-hyperelastic model and option instantaneous, that gives the same static reaction force at actuator displacement $0.2\,\mathrm{mm}$ as the visco-hyperelastic model with option long term, is in good agreement with the value $\alpha = 20.9$, reported by Bergomi et al. (2011).

---

[5] Observe that Eq. 2.98 has no input-strain-rate dependency.

5.5 Poro-Visco-Hyperelastic Analysis

5.5.1 Transient Response

The poro-visco-hyperelastic analysis is based on the visco-hyperelastic model described in Chap. 5.4.1. The model includes the poroelastic parameters and boundary conditions mentioned in Chap. 5.2 and the visco-hyperelastic parameters in Tab. 5.3, No. 2. In addition, a Neumann boundary condition (free draining) was specified at the free PDL surface, adjacent to the alveolar crest, where gingiva was removed from the specimen. For the PDL strain dependent permeability, based on the relation proposed by Argoubi and Shirazi-Adl (1996) and adopted in the investigation of Bergomi et al. (2009) [6], was assumed:

$$k = k_0 \left(\frac{n}{n_0} \right)^2 e^{M(\lambda - 1)} \, . \tag{5.9}$$

Here, k is the permeability, n is the porosity, $M \in \mathbb{R}^{+} \backslash 0$ is a constant greater than zero, λ is the stretch, and the subscript 0 refers to the reference state, i.e. $\lambda = 1$. As starting point, values published by Bergomi et al. (2009) were assumed, that is $k_0 = 8.81 \cdot 10^{-15}\,\mathrm{m}^2$ and $M = 14.2$. Though not explicitly stated in literature, Eq. 5.9 was derived for compression strains. Therefore, it was assumed that in tension permeability remains constant, i.e. $k = k_0$ for $\lambda \geq 1.0$. The solution procedure was changed to poro-elasticity[7].

A plot of the poro-visco-hyperelastic response, versus the visco-hyperelastic response, for test No. 2, is shown in Fig. 5.12. In the bottom of the plot, the difference between poro-visco-hyperelastic response and visco-hyperelastic response is shown. With the chosen parameters, the maximal difference at peak force is about $0.04\,\mathrm{N}$. The difference between poro-visco-hyperelastic and visco-hyperelastic peak force for all tests with actuator displacement $0.2\,\mathrm{mm}$ is shown in Fig. 5.13. The difference decreases with ramp rise time.

---

[6] In the paper of Bergomi et al. (2009) the n/n_0 ratio is stated without exponent. However, the original paper of Argoubi and Shirazi-Adl (1996) and the review paper of Riches et al. (2002) show the exponent two. The quadratic term was used here.

[7] ABAQUS (2016) poro-elastic analysis procedure is invoked with: `*SOILS, CONSOLIDATION`

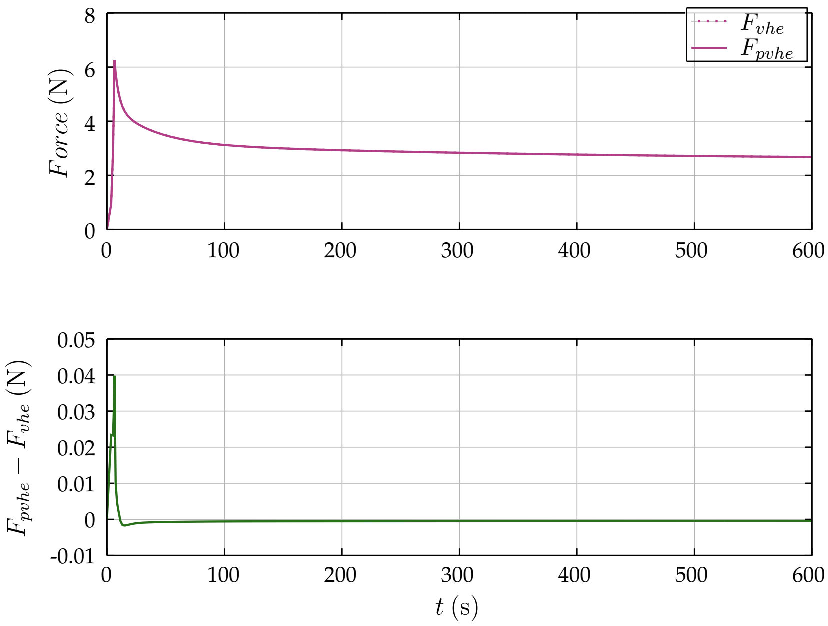

FIGURE 5.12: Poro-visco-hyperelastic response F_{pvhe} ($k_0 = 8.81 \cdot 10^{-15}\,\mathrm{m}^2$, $M = 14.2$) versus visco-hyperelastic response F_{vhe}, with parameters form Tab. 5.3 No. 2, for the test No. 2 in Tab. 4.1.

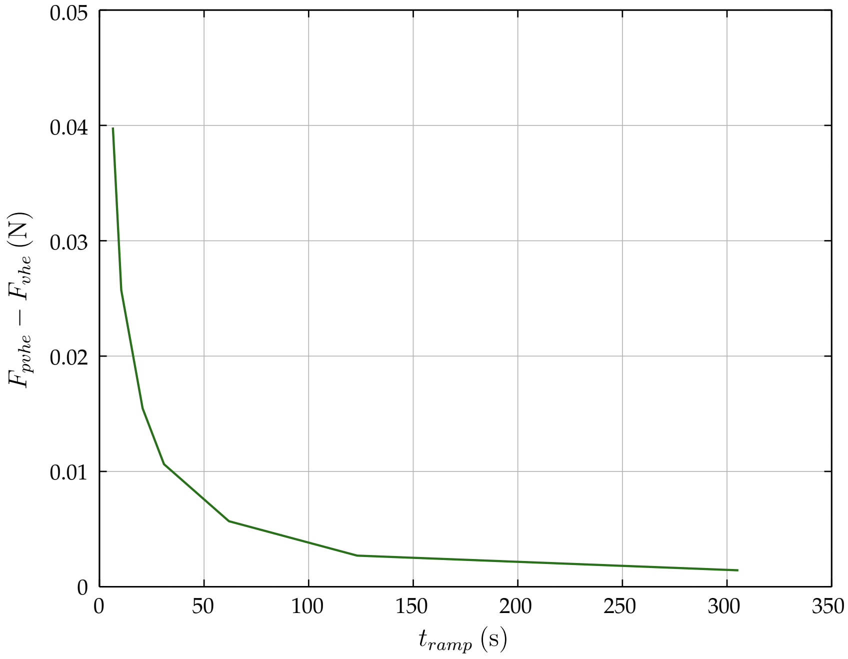

FIGURE 5.13: Difference between poro-visco-hyperelastic F_{pvhe} and visco-hyperelastic F_{vhe} peak force versus ramp rise time t_{ramp}, for all tests with actuator displacement $0.2\,\mathrm{mm}$.

5.5.2 Parameter Study

Various parameters deemed relevant for Darcy's flow were varied. The effect of decreasing the initial permeability k_0 is shown in Fig. 5.14, and the effect of increasing the exponent M is shown in Fig. 5.15. For both, an increase of the peak force, for a short duration, is observed. Further, the permeability of the alveolar bone was varied. The response is shown in Fig. 5.16, and again, an increase of the peak force for a short duration is observed with decreased alveolar bone permeability. The effect of decreasing the cancellous bone permeability k is shown in Fig. 5.17. Decreasing the cancellous bone permeability by two orders of magnitude has a negligible effect on the response.

Next, the influence of the Neumann boundary condition (free draining) was investigated. In Fig. 5.18 the poro-visco-hyperelastic response with Neumann boundary condition, without Neumann boundary condition at the free PDL surface, and in addition, with alveolar bone permeability decreased by ca. $1/2$, that is $k = 10^{-15}\,\mathrm{m}^2$, is shown. Without Neumann boundary condition, that is, without free draining at the PDL surface, peak force is slightly increased, and a small increase in the steady state force level is observed. Decreasing the permeability of the alveolar bone increases peak force.

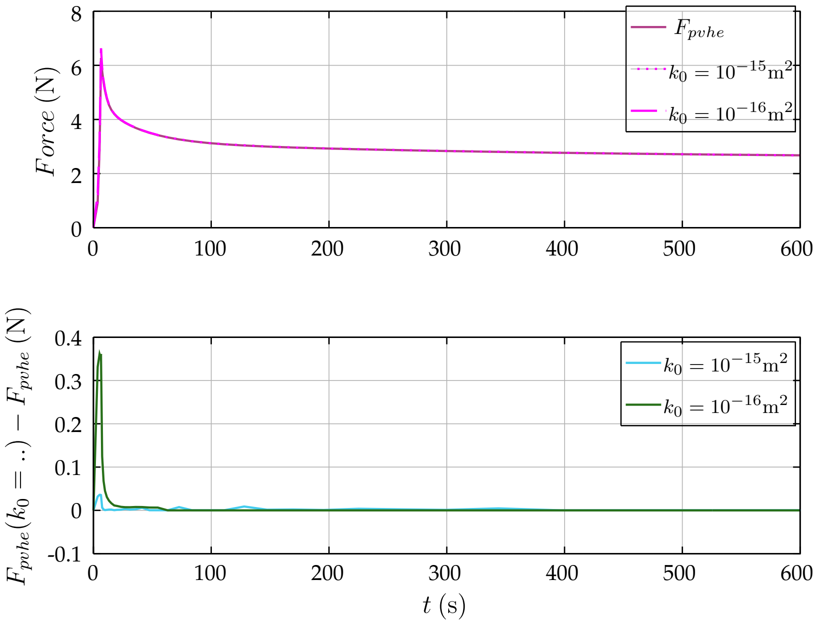

FIGURE 5.14: PDL parameter k_0 variation: Poro-visco-hyperelastic response F_{pvhe}, with $M = 14.2$ and $k_0 = 8.81 \cdot 10^{-15}\,\mathrm{m}^2$, versus $k_0 = 1.0 \cdot 10^{-15}\,\mathrm{m}^2$, and $k_0 = 1.0 \cdot 10^{-16}\,\mathrm{m}^2$.

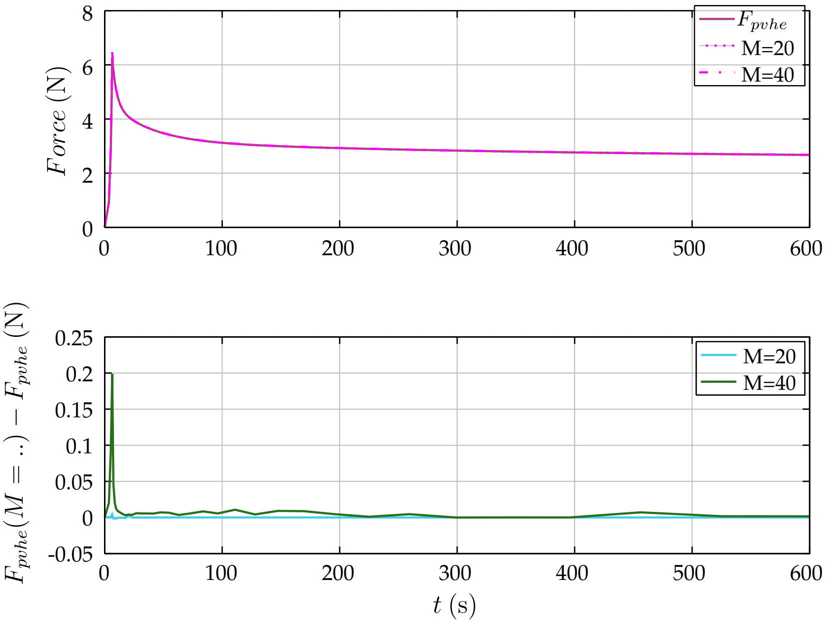

FIGURE 5.15: PDL parameter M variation: Poro-visco-hyperelastic response F_{pvhe}, with $k_0 = 8.81 \cdot 10^{-15}\,\mathrm{m}^2$ and $M = 14.2$, versus $M = 20$ and $M = 40$.

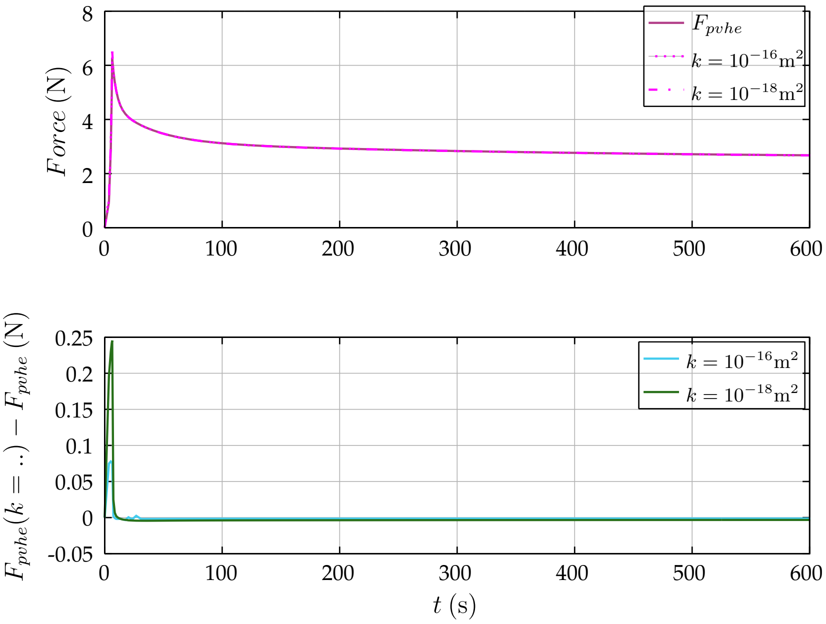

FIGURE 5.16: Alveolar bone permeability k variation: Poro-visco-hyperelastic response F_{pvhe}, with alveolar bone permeability $k = 5.29 \cdot 10^{-14}\,\mathrm{m}^2$, versus $k = 10^{-16}\,\mathrm{m}^2$, and $k = 10^{-18}\,\mathrm{m}^2$.

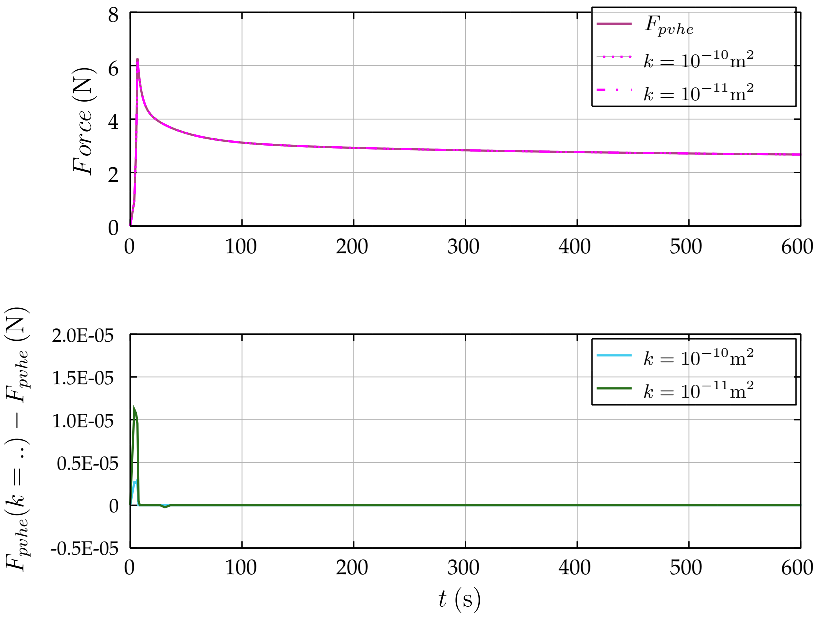

FIGURE 5.17: Cancellous bone permeability k variation: Poro-visco-hyperelastic response F_{pvhe}, with cancellous bone permeability $k = 10^{-9}\,\mathrm{m}^2$, versus $k = 10^{-10}\,\mathrm{m}^2$, and $k = 10^{-11}\,\mathrm{m}^2$.

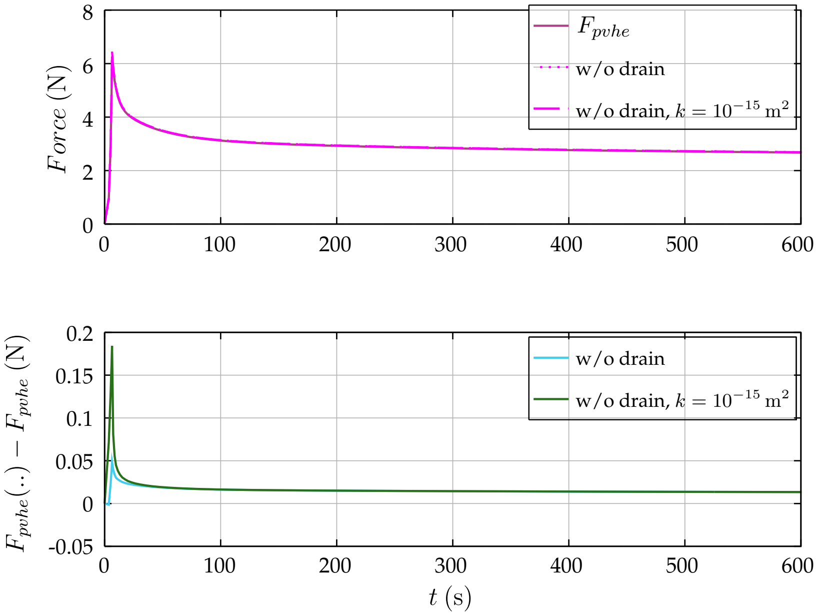

FIGURE 5.18: Poro-visco-hyperelastic response with Neumann boundary condition F_{pvhe}, Neumann boundary condition at the free PDL surface removed (labeled: w/o drain), and in addition, alveolar bone permeability decreased by ca. 1/2, that is $k = 10^{-15}\,\mathrm{m}^2$.

5.5.3 Discussion – Poro-visco-hyperelastic Analysis

Tooth and cortical bone permeability were not varied in the parameter investigation. They are three, respectively six orders of magnitude lower than alveolar bone permeability (Ref. Tab. 5.1). Therefore, pore fluid flow in tooth and cortical bone is deemed negligible. For the tooth, this was also concluded by Bergomi et al. (2011).

Darcy'c Flow Contribution

Considering Fig. 5.12, the poro-visco-hyperelastic response shows, for a short duration, a slight increase of the peak force versus the visco-hyperelastic response. Shortly after the initial peak, responses are practically identical. The difference between poro-visco-hyperelastic and visco-hyperelastic peak force, shown in Fig. 5.13, decreases with ramp rise time, or equivalently, increases with actuator velocity. An animation of flow velocities reveals that Darcy's flow ceases shortly after the initial peak force. This observation is in agreement with the presumption made in Chap. 3. That is, poroelastic behaviour will gradually cease when visco-elastic relaxation progresses. The results here indicate that the line drawn in Fig. 3.1, for the PDL in situ, should be shifted down about 2 orders of magnitude. Part of this maybe due to the actual mass diffusion coefficient D, which could be larger than assumed. The first time constant identified here, $\tau_1 = 3.21\,\mathrm{s}$, is smaller than assumed.

PDL, Alveolar Bone, and Cancellous Bone Permeability

According to Fig. 5.14 and Fig. 5.15, changing the PDL permeability, by decreasing initial permeability k_0, or increasing the exponent M of Eq. 5.9, will both increase the poro-visco-hyperelastic peak force.

Next, in Fig. 5.16, with decreased permeability of the alveolar bone, an increased peak force is observed. The results indicate that, with suitable choice of the parameters, peak force and width of the peak can be increased. For all cases, duration of increased force level versus the visco-hyperelastic response is short. Again, Darcy's flow ceases shortly after the initial peak force.

The effect of cancellous bone permeability on the response, shown in Fig. 5.17, is negligible. According to Cowin (2001), Fig. 25.3, permeability decreases two orders of magnitude going from porosity 0.8, used here, to 0.4. This represents the lower bound, that is, lower values of cancellous bone permeability are not shown in the diagram. Recalling Tab. 5.1, cancellous bone permeability used here, is about five orders of magnitude higher than alveolar bone permeability. Therefore, alveolar bone represents the determinative resistance to interstitial fluid flow and cancellous bone permeability, within physically justified limits, has a negligible effect on the response. Concluding, it appears that alveolar bone permeability has a essential role defining interstitial fluid flow from the PDL.

Neumann Boundary Condition

The effect of removing the Neumann boundary condition (free draining) at the free PDL surface, adjacent to the alveolar crest, where gingiva was removed from the specimen, is shown in Fig. 5.18. A slight increase in the peak force is observed. In addition, force level of the long term response is ca. $0.02\,\mathrm{N}$ higher than the visco-hyperelastic response. Again, with decreased permeability of the alveolar bone, an increased peak force is observed. However, long term response is not changed. It may be argued that, in vivo, the PDL is *sealed* at the alveolar crest, by the gingival fibre bundles. This assertion is supported by the observation that, for tendons, according to Cowin and Doty (2007), page 588, the permeability in fibre direction is about 2.5 times greater than perpendicular to the fibre direction. That is, gingival fibre bundles would represent a barrier for interstitial fluid flow. However, gingiva was removed from the specimen at the alveolar crest. It is thus unlikely, that the PDL was sealed in the test. Therefore, the assumed Neumann boundary condition (free draining) is deemed justified. Nevertheless, in vivo, the hypothesised sealing effect of the gingival fibre bundles, and the influence shown in Fig. 5.18, may be relevant. That is, a slightly increased peak force, and more important, a slightly increased long term force plateau may be observed in vivo, which may be attributed to a increased pore pressure at the alveolar bone, without free draining. When removing the external load, increased pore pressure at the alveolar bone may contribute to the restoring mechanism, that drives the tooth back to its original position.

Ramp Rise Time Term

Recalling the model function Eq. 4.20, measured data were approximated by the sum of a viscoelastic term, a ramp rise time term, and a prior load history term. In the simulation, the viscoelastic term is covered by the transient visco-hyperelastic analysis in Chap. 5.4.1. The prior load history term can be discarded. It represents the influence of prior tests, on the current test, during measurement. Simulations were started in the reference state[8], i.e. for simulations done, there is no influence of the previous tests. Left over is the ramp rise time term. It represents a force that is proportional to the actuator displacement, and decays exponentially with ramp rise time. Clearly, the difference between poro-visco-hyperelastic response and visco-hyperelastic response shown in Fig. 5.12, that is the contribution of Darcy's flow to the reaction force, does not depict this characteristic. It could explain an increased force for short ramp rise time, or equivalently for high actuator velocity. However, contrary to the ramp rise time term, it ceases shortly after the initial peak force. Therefore, in this investigation, no final parameters for Darcy's flow were deduced.

Trapped vs. Free Interstitial Fluid and Vascular System

Based on light and scanning electron microscope investigation of rabbit incisor periodontal ligaments, sliced in transverse, oblique, and axial (median) planes, Sloan (1978) distinguished three zones, the alveolar, middle, and cemental zone, respectively occupying about $40\,\%$, $50\,\%$, and $10\,\%$ of the total ligament width. Considering the axial (median) plane, Sloan (1978) observed that, 'the middle zone appeared as an undulating, sheet-like continuum of fibers which formed a series of compartments.' Resting upon that, Zhurov et al. (2007) argued, 'Although the PDL has a porous structure, the fluid cannot move easily between compartments ... Therefore, there is no need to consider fluid flows in a porous medium explicitly in our model.' However, in the opinion of the author, there is no evidence, that the interstitial fluid remains trapped in the interstitial areas. Considering sections of the periodontal ligament, e.g. Hand and Frank (2015), Fig. 6.13, collagen fibre bundles, interstitial areas and blood vessels are observed. In addition, there may be free interstitial fluid between the fibre bundles. The measurement of Bergomi et al. (2011) showed the presence of interstitial fluid flow. Also, the simulation done here showed that Darcy's flow contribution is expected in the initial phase of the Papadopoulou et al. (2013) test, before visco-hyperelastic response prevails.

Upon these observations, it might be argued to split porosity according to trapped interstitial fluid, free interstitial fluid, and vascular fluid (blood)[9]. The porosity value used here, based on Bergomi et al. (2011), was 'assessed by measuring the volume of fluid blotted out of the PDL under a compressive force'.

---

[8] One could start simulation in deformed state after the rest time of the previous test. However, there are no measurement records of the load time history between the test and it would be computationally expensive.

This might have contained vascular fluid. Therefore, for interstitial fluid flow, actual porosity could be smaller than measured. One could argue that the contribution of the vascular system should be modelled. As mentioned in Chap. 1, Cowin and Doty (2007) state for bone tissue a vascular relaxation time of $1.36\,\mu\mathrm{s}$ and argued that, 'even under accidental impact loading, the stress rise time never approaches the vascular porosity relaxation time.' If this holds true, the vascular system will not contribute significantly to the reaction force, and may be negligible for the tests considered here. This is also supported by the observation that blood pressure is about $100\,\mathrm{mmHg}$ ($13.3\,\mathrm{kPa}$), stresses in the PDL during test is in the order of magnitude $1\,\mathrm{MPa}$, i.e. two orders of magnitude higher.

Still, porosity of the PDL could be reduced to take the portion of the trapped interstitial fluid and bold in the vascular system into account. This has an effect on the permeability, since intrinsic permeability is dependent on porosity (Cheng and Detournay, 1993). Here we have done parameter studies, changing PDL permeability three orders of magnitude, and did not infer on a particular value. Small adjustments of porosity, of a couple of percent, do not alter the conclusions of the parameter study.

Further, the effect of trapped fluid, if it exists, was certainly present in the measurement. Identified parameters of the constitutive model are based on the measured reaction force curves. Therefore, the effect of the trapped fluid is taken into account by the identified parameters of the constitutive model.

---

[9] ABAQUS (2016) implemented two fluids in the porous medium. One, the 'wetting liquid' is split into a free and trapped part. The other can be relatively compressible. This could be utilised to refine the model.

Chapter 6

Summary – Discussion – Conclusion

6.1 Summary

In Chap. 3, the experimental setup was classified based on dimensionless analysis. Regions where poroelasticity or viscoelasticity dominate were distinct. Dimensionless analysis indicates that initially poroelasticity is observed, however viscoelasticity will prevail after an initial transition phase.

Then, in Chap. 4, a curve fit of the in vitro experiment of Papadopoulou et al. (2013) is described. A model function, assuming viscoelasticity, was introduced. The viscoelastic model function was augmented by a ramp rise time term, to account for observed dependence of the response on ramp rise time, and a previous load history term, to account for the effect of the previous tests on the current test. Curve fits of individual tests, tests with actuator displacement $0.1\,\mathrm{mm}$ and $0.2\,\mathrm{mm}$, and of all tests grouped together, were done. The final curve fit of all tests grouped together had a correlation coefficient of $R^2 = 0.9800$. Parameters are listed in Tab. 4.8.

Next, a curve fit of the in vivo experiment of Konermann et al. (2017) was done. Good correlation was found for a simplified model function, without viscoelastic effect. Final parameters, with correlation coefficient of $R^2 = 0.9637$, are listed in Tab. 4.10, No. 4. Presumably due to the short test duration (the test duration was between $0.4\,\mathrm{s}$ and $20\,\mathrm{s}$) viscoelastic effects were not evident. For both tests, in vitro and in vivo, the ramp rise time term improved correlation.

In Chap. 5, the in vitro experiment of Papadopoulou et al. (2013) was simulated. Parameters for the Storåkers and the Marlow hyperelastic constitutive model were identified. Based on the argument, that stress is estimated directly from the strain energy density function, with parameters identified to match both, compression and tension regions, Storåkers constitutive model was selected for subsequent analysis. Parameters of the Storåkers constitutive model found here (Chap. 5.4.4) are in good agreement with values published by Bergomi et al. (2011). The parameters of the visco-hyperelastic model were optimised to match the viscoelastic target force curve. The final parameters are listed in Tab. 5.3, No. 2, and the coefficient of multiple correlation is $R^2 = 0.9285$.

Then, in Chap. 5.5, the poro-visco-hyperelastic model was simulated and sensitivity to selected model parameters was studied. The poro-visco-hyperelastic response shows, for a short duration, a slight increase of the force level versus the visco-hyperelastic response, and Darcy's flow decays shortly after the initial peak force. This behaviour was anticipated based on the dimensionless analysis in Chap. 3. Peak force is sensitive to various model parameters. Permeability of the PDL and also permeability of the alveolar bone have a significant effect. The ramp rise time term could not be explained with Darcy's flow contribution to the simulated poro-visco-hyperelastic response. Therefore, no final parameters for Darcy's flow were concluded.

6.2 Discussion

Corresponding topics are discussed at the end of each chapter: Chap. 3.2 – Dimensionless Analysis, Chap. 5.3.4 – Constitutive Model, Chap. 5.4.4 – Visco-hyperelastic Analysis, and Chap. 5.5.3 – Poro-visco-hyperelastic Analysis. Here, some additional, chapter overreaching points are discussed.

6.2.1 Poro-Visco-Hyperelastic Model

In Chap. 3 and Chap. 5.5 it was concluded, that poroelastic behaviour will gradually cease when viscoelastic relaxation progresses. Poroelasticity is, due to the additional degree of freedom for pressure, computationally more expensive. In addition, the Neumann boundary condition (free draining) poses a discontinuity[1], with associated numerical challenge. For *slow* loading, or if initial response to *fast* loading is not of interest, a visco-hyperelastic model may suffice.

---

[1] ABAQUS (2016), Users Manual, Chap. 30.4.6, Pore fluid flow: 'In all cases the freely draining flow type represents discontinuously nonlinear behaviour, and its use may require appropriate solution controls.'

6.2.2 Sequence Effect and Strain Rate Hardening

In Chap. 5.5, it was shown that the ramp rise time term of model function Eq. 4.20 could not be explained by Darcy's flow contribution to the poro-visco-hyperelastic response. Darcy's flow contribution represents a short duration, additional force, that increases inversely with actuator velocity and ceases shortly after actuator displacement remains constant. This behaviour, that after a initial poroelastic contribution viscoelastic behaviour prevails, was also expected from dimensionless analysis in Chap. 3. The ramp rise time term represents a force, that is proportional to the actuator displacement and decays exponentially with ramp rise time, or equivalently decays with inverse ramp velocity. A tempting supposition, to explain this effect on the micro scale, would be to assume *strain rate hardening*. A higher strain rate, due to higher actuator velocity, would result in a higher stress level. In favour of this presumption is that for both, the in vitro and the in vivo experiment, the ramp rise time term improved the correlation coefficient. Before endeavour this route, the possibility that the observation is a result of the test sequence should be clarified. Recall that the test sequence of Papadopoulou et al. (2013) was not randomised. That is, tests were done with ramp time $5\,\mathrm{s}$, $10\,\mathrm{s}$, $20\,\mathrm{s}$, $30\,\mathrm{s}$, $60\,\mathrm{s}$, $120\,\mathrm{s}$, $300\,\mathrm{s}$, $450\,\mathrm{s}$ and $600\,\mathrm{s}$, in the stated sequence. Properties of the specimen may have altered in the course of the experiment. In particular, tests with high actuator velocity, and associated high stress, were done first. To avoid these concerns, a random test order should be used.

Strain rate hardening has been observed by other investigators. For the rat middle cerebral arteries, David Bell et al. (2018) observed, 'Although both in vivo stiffness and failure stress increased significantly with strain rate, failure stretch did not depend on rate.' According to Burgin et al. (2014), 'The mechanical properties of articular cartilage vary enormously with loading rate, and how these properties derive from the composition and structure of the tissue is still unclear.' For biological composites Chintapalli et al. (2014) adapted a strain rate hardening model, which follows a general constitutive model for metals stated in Meyers (1994), that captures strain hardening as well as rate effects. Whether this model is suitable for soft biological tissues is in question, in particular since the underlying microstructural mechanism is not known.

6.2.3 Parameter Identification by Means of a Model Function versus Finite Element Simulation

In this work, a model function, that was successively refined to take observed effects into account, was used to identify model parameters. In other works, e.g. Bergomi et al. (2011) and Seifzadeh et al. (2012), model parameters are identified directly by means of finite element simulation. In both cases mentioned, the specimen was a cylindrical plug and a axisymmetric model was used. Compared to the specimen used here, this considerably reduced model size and associated computational cost, which makes direct parameter identification with finite element simulation an option. In principle this is, on the expense of computational cost, also feasible for the model used here. However, parameter identification by means of a model function has some merits: First, computational cost is considerably reduced, even compared to a rough, simplified finite element model. It requires, and arguably fosters, a thorough anticipation of the physical processes involved, to come up with a meaningful model function, that describes relevant effects in the most basic form. However, there is certainly a limit to what extend this can be achieved. For example, in Chap. 5.4 we found that a single Maxwell element could not describe the reaction force, resulting from a spacial inhomogenous stress distribution in the PDL, with desired accuracy. As a consequence, parameters identified by means of the model function had to be further optimised by means of finite element simulation.

6.2.4 Optimisation Strategy

Suffice to say that optimisation has been a subject of intensive research for decades. To categorise the optimisation strategies used herein, refer to the introduction in the contribution of Roshanian et al. (2018) to the proceedings of the Twelfth World Congress of Structural and Multidisciplinary Optimisation. In this context, the model defined by optimal interpolation of points, predicted with a finite element analysis, would be referred to as *optimum interpolation meta-model*. Similar meta-models, based on interpolation, appeared in the second half of the 1990s. Evaluation of the meta-model is computationally cheap. Therefore full factorial experiments were feasible.

Throughout this work several minimisation problems had to be solved. In Chap. 4.1.3, based on a model function, a full factorial experiment was used, and at points, where the coefficient of multiple correlation was better than a threshold, a Levenberg-Marquardt curve fit was executed to further optimise parameters. Evaluation of the model function is computationally cheap, which made a full factorial experiment an option.

In Chap. 5 optimal parameters of the finite element model were identified on several occasions. Evaluation of the finite element model is computationally expensive. Therefore, in Chap. 5.3.2 and Chap. 5.4.1, for limited number of parameter combinations the response was simulated with the finite element model. In the parameter region where the norm of the error was minimal, a refined parameter study was conducted by means of optimal interpolation (e.g. Barth et al. (2008)). The thus found optimal parameters were further refined and verified by simulation with the finite element model. For the second step, initially response surface methods were tried. However optimal interpolation, which does not require assumptions on the nature of the response surface, worked superior. It is computationally cheap, which allowed a refined full factorial experiment in the identified parameter region at low cost.

As a final remark, defining the meta-model in a suitable way is of utmost importance. For the minimisation problems stated here, we wanted to minimise the norm of the error, which is, by definition of a norm, a positive real number. Assume we want to interpolate between known points, where the error changes sign. Provided the function of the error is continuous, there is at least one zero of the error between these points, with corresponding minimum (zero) of the norm of the error. Interpolating the error, there is a good chance to find the zero. However, interpolating the norm of the error will give a positive real number, and it is unlikely to find the minimum. Concluding, for the minimisation problems stated herein, a optimal interpolation meta-model based on error will perform superior.

6.3 Conclusion

- The present work indicates that the macroscopic response of the periodontal ligament to an external load can be simulated with a poro-visco-hyperelastic model. For the hyperelastic model of the ground substance, Storåkers constitutive model was used, and parameters identified herein are in good agreement with values published in Bergomi et al. (2011). Given that the experimental setup was completely different, the agreement is remarkable. The simulation showed that poroelastic behaviour will gradually cease when viscoelastic relaxation progresses. This followed also from dimensionless analysis. As a consequence, for slow loading, or if initial response to fast loading is not of interest, a visco-hyperelastic model may suffice.

- The curve fit of the model function conceived herein is in good agreement with measured data. The model function includes a ramp rise time term, which could not be covered with the poro-visco-hyperelastic simulation. A supposition to explain this effect on the micro scale is to assume *strain rate hardening*. For soft tissues strain rate effects were observed by other investigators, e.g. David Bell et al. (2018) and Burgin et al. (2014), however the underlying microstructural mechanism is still unknown. Papadopoulou et al. (2013) did not randomise the test sequence with respect to ramp rise time. Therefore, it can not be excluded that the effect is due to test sequence. To clarify this objection, further tests with randomised test sequence are recommended.

- In addition to randomised test sequence, subsequent tests should bear in mind the time required for viscoelastic relaxation. To minimise the residual effect of the previous on the current test, rest time between individual tests should be at least four times the largest time constant anticipated. Alternatively one could consider making the unloading phase part of the test protocol. That is, unloading with the actuator would provide additional information that could be used.

- The final parameters of the visco-hyperelastic simulation with Storåkers constitutive model identified herein are listed in Tab. 6.1. The parameters of the Storåkers constitutive model are: the initial shear modulus μ, the exponent α and the effective Poisson's ratio ν. The parameters g_i and τ_i, with $i \in \{1, 2, 3\}$, are the modulus ratios and time constants of the corresponding Maxwell-elements.

TABLE 6.1: Final parameters of the visco-hyperelastic simulation with Storåkers constitutive model.

μ	α	ν	g_1	τ_1	g_2	τ_2	g_3	τ_3
-	-	-	-	s	-	s	-	s
0.0338	29.7	0.236	0.45	3.21	0.20	31.1	0.08	372.

Bibliography

ABAQUS (2016). *ABAQUS Documentation*. Dassault Systèmes.

Argoubi, M. and A. Shirazi-Adl (1996). 'Poroelastic creep response analysis of a lumbar motion segment in compression'. In: *Journal of Biomechanics* 29.10, pp. 1331 –1339.

Arruda, E.M. and M.C. Boyce (1993). 'A Three-Dimensional Constitutive Model for the Large Stretch Behavior of Rubber Elastic Materials'. In: *Journal of the Mechanics and Physics of Solids* 41, pp. 389–412.

Ateshian, G.A. et al. (1997). 'Finite deformation biphasic material properties of bovine articular cartilage from confined compression experiments'. In: *Journal of Biomechanics* 30.11, pp. 1157–1164.

Barth, Alexander et al. (2008). *Introduction to Optimal Interpolation and Variational Analysis*. University of Liège: GeoHydrodynamics and Environment Research Institute.

Bergomi, Marzio et al. (2009). 'Mechanical response of periodontal ligament: Effects of specimen geometry, preconditioning cycles and time lapse'. In: *Journal of Biomechanics* 42.14, pp. 2410 –2414.

Bergomi, Marzio et al. (2011). 'Hydro-mechanical coupling in the periodontal ligament: A porohyperelastic finite element model'. In: *Journal of Biomechanics* 44.1, pp. 34 –38.

Beyer, W. H., ed. (1984). *CRC Standard Mathematical Tables*. 27th ed. Boca Raton, Florida, USA: CRC Press.

Biot, M. A. (1941). 'General theory of three-dimensional consolidation'. In: *Journal of Applied Physics* 12, pp. 155 –164.

— (1956a). 'Theory of propagation of elastic waves in a fluid-saturated porous solid, part I: low frequency range'. In: *The Journal of the Acoustical Society of America* 28, pp. 168 –178.

— (1956b). 'Theory of propagation of elastic waves in a fluid-saturated porous solid, part II: higher frequency range'. In: *The Journal of the Acoustical Society of America* 28, pp. 179 –191.

— (1973). 'Nonlinear and semilinear rheology of porous solids'. In: *Journal of Geophysical Research* 78.23, pp. 4924 –4937.

Biot, M.A. and D.G. Willis (1957). 'The elastic coefficients of the theory of consolidation'. In: *Journal of Applied Mechanics* 24, pp. 594–601.

Boer, R. de (2000). *Theory of Porous Media: Highlights in Historical Development and Current State*. 1st ed. Berlin Heidelberg: Springer-Verlag.

Boer, R. de and W. Ehlers (1986). 'Theorie der Mehrkomponentenkontinua mit Anwendung auf bodenmechanische Probleme'. In: *Forschungsberichte aus dem Fachbereich Bauwesen*. Vol. 40. Essen: Universität Essen.

Boltzmann, L. (1874). 'Zur Theorie der elastischen Nachwirkung'. In: *Sitzungsb. Math. Naturwiss. Kl. Kaiserl. Akad. Wiss.* Vol. 70 (2), pp. 275–306.

Bonet, Javier and Richard D. Wood (2008). *Nonlinear Continuum Mechanics for Finite Element Analysis*. 2nd ed. Cambridge University Press.

Boschetti, Federica et al. (2004). 'Biomechanical properties of human articular cartilage under compressive loads'. In: *Biorheology* 41, pp. 159–166.

Bowen, Ray M. (1980). 'Incompressible porous media models by use of the theory of mixtures'. In: *International Journal of Engineering Science* 18.9, pp. 1129 –1148.

Bronstein, I.N. et al. (2005). *Taschenbuch der Mathematik*. 6th ed. Frankfurt am Main: Wissenschaftlicher Verlag Harri Deutsch GmbH.

Burgin, L.V. et al. (2014). 'The mechanical and material properties of elderly human articular cartilage subject to impact and slow loading'. In: *Medical Engineering Physics* 36.2, pp. 226 –232.

Burstone, C. J. (1962). 'The biomechanics of tooth movement'. In: *Vistas in Orthodontics*. Ed. by B. S. Kraus and R. A. Riedel. Philadelphia, PA: Lea Febiger, 197–213.

Capone, Claudia Cristiana Chiara (2010). *Poro_Thermoelastic Duality and FE-based strategies for the analysis of biological tissues*. Italy: University of Naples. URL: `http://www.fedoa.unina.it/7962/`.

Charras, Guillaume T. et al. (2009). 'Animal cell hydraulics'. In: *Journal of Cell Science* 122.18, pp. 3233–3241.

Cheng, A.H.-D. and E. Detournay (1993). 'Fundamentals of poroelasticity'. In: *Comprehensive Rock Engineering: Principles, Practice and Projects, Analysis and Design Methods* 2. Ed. by C. Fairhurst, pp. 113 –171.

Chintapalli, Ravi Kiran et al. (2014). 'Strain rate hardening: A hidden but critical mechanism for biological composites?' In: *Acta Biomaterialia* 10.12, pp. 5064 –5073.

Chong, Edwin Kah Pin and Stanislaw H. Zak (2013). *An introduction to optimization*. 4th ed. Wiley-Interscience series in discrete mathematics and optimization. New York: Wiley.

Christensen, Richard M. (1982). *Theory of Viscoelasticity*. 2nd ed. Academic Press.

Christian, John T. (1968). 'Undrained stress distribution by numerical methods'. In: *Journal of the Soil Mechanics and Foundations Division* 94.6, pp. 1333–1345.

Coussy, Olivier (1995). *Mechanics of Porous Continua*. John Wiley.

— (2004). *Poromechanics*. 2nd ed. John Wiley.

Cowin, Stephen C (1999). 'Bone poroelasticity'. In: *Journal of Biomechanics* 32.3, pp. 217–238.

Cowin, Stephen C. (2001). *Bone mechanics handbook*. 2nd ed. CRC Press.

Cowin, Stephen C. and Stephen B. Doty (2007). *Tissue Mechanics*. 1st ed. Springer.

David Bell, E. et al. (2018). 'Material Properties of Rat Middle Cerebral Arteries at High Strain Rates'. In: *Journal of Biomechanical Engineering* 140.7, pp. 071004 –071004–7.

Davidovitch, Zeev and Vinod Krishnan (2015). *Biological Mechanisms of Tooth Movement*. 2nd ed. Wiley-Blackwell.

Deuflhard, Peter and Andreas Hohmann (2002). *Numerische Mathematik*. Vol. 1. Berlin, Boston: De Gruyter.

Draper, Norman R. and Harry Smith (1998). *Applied Regression Analysis*. 3rd ed. Wiley Series in Probability and Statistics. Wiley-Interscience.

Duck, F. A. (1990). *Physical Properties of Tissues. A Comprehensive Reference Book*. Academic Press.

Eaton, John W. et al. (2017). *GNU Octave version 4.2.1 manual: a high-level interactive language for numerical computations*. URL: `https://www.gnu.org/software/octave/doc/v4.2.1/`.

Eckert, Ernst (1949). *Einführung in den Wärme- und Stoffaustausch*. Berlin Heidelberg: Springer.

Ehlers, W. and B. Markert (2001). 'A linear viscoelastic biphasic model for soft tissues based on the theory of porous media'. In: *Journal of Biomechanical Engineering* 123.5, pp. 418 –424.

Fill, Ted S. et al. (2012). 'Analytically determined mechanical properties of, and models for the periodontal ligament: Critical review of literature'. In: *Journal of Biomechanics* 45.1, pp. 9 –16.

Findley, William N. and Kasif Lai James S.and Onaran (1976). *Creep and Relaxation of Nonlinear Viscoelastic Materials - With an Introduction to Linear Viscoelasticity*. Dover Publications.

Flory, P. J. (1961). 'Thermodynamic relations for high elastic materials'. In: *Transactions of the Faraday Society* 57, pp. 829–838.

Fung, Y.C. (1967). 'Elasticity of soft tissues in simple elongation'. In: *American Journal of Physiology* 213, pp. 1532 –1544.

Fung, Yuan-Cheng (1993). *Biomechanics: Mechanical Properties of Living Tissues*. 2nd ed. New York: Springer-Verlag.

Gambolati, Giuseppe (2006). 'Anthropogenic Land Subsidence'. In: *Encyclopedia of Hydrological Sciences*. Ed. by Malcolm G. Anderson. John Wiley & Sons.

Ghaboussi, J. and E. L. Wilson (1973). 'Flow of compressible fluid in porous elastic media'. In: *International Journal for Numerical Methods in Engineering* 5.3, pp. 419–442.

Gong, J. K. et al. (1964). 'Composition of trabecular and cortical bone'. In: *The Anatomical Record* 149.3, pp. 325–331.

Gough, J. et al. (1999). 'Determination of constitutive equations for vulcanized rubber'. In: *Finite Element Analysis of Elastomers*. Ed. by D. Boast and V.A. Coveney. Vol. 5-26. London: Professional Engineering Publisher.

Hand, Arthur R. and Marion E. Frank (2015). *Fundamentals of Oral Histology and Physiology*. 1st ed. Wiley-Blackwell.

Hermann, L.R. and F.E. Peterson (1968). 'A numerical procedure for viscoelastic stress analysis'. In: *Seventh meeting of ICRPG mechanical behavior work group*. Vol. 177. Orlando, FL: CPIA Publication.

Hodgskinson, R. and J. D. Currey (1992). 'Young's modulus, density and material properties in cancellous bone over a large density range'. In: *Journal of Materials Science: Materials in Medicine* 3.5, pp. 377–381.

Holmes, M.H. and V.C. Mow (1990). 'The nonlinear characteristics of soft gels and hydrated connective tissues in ultrafiltration'. In: *Journal of Biomechanics* 23.11, pp. 1145–1156.

Holzapfel, Gerhard A. (2001). 'Biomechanics of Soft Tissue'. In: *Handbook of Materials Behavior Models*. Ed. by Jean Lemaitre. Burlington: Academic Press, pp. 1057 –1071.

Incropera, Frank P. and David P. DeWitt (1985). *Fundamentals of Heat and Mass Transfer*. 2nd ed. Wiley.

Kaliske, M. and H. Rothert (1997). 'Formulation and implementation of three-dimensional viscoelasticity at small and finite strains'. In: *Computational Mechanics* 19.3, pp. 228–239.

Kaye, G.W.C. and T.H. Laby (1995). *Tables of Physical Chemical Constants*. 16th ed. Kaye Laby Online. Version 1.0 (2005). URL: `www.kayelaby.npl.co.uk`.

Kilian, H.-G. et al. (1986). 'The Use of the van der Waals Model to Elucidate Universal Aspects of Structure-Property Relationships in Simply Extended Dry and Swollen Rubbers'. In: *Colloid and Polymer Science* 264, 866–876.

Konermann, Anna et al. (2017). 'In vivo determination of tooth mobility after fixed orthodontic appliance therapy with a novel intraoral measurement device'. In: *Clinical Oral Investigations* 21.4, pp. 1283–1289.

Krishnan, Vinod and Ze'ev Davidovitch (2015). *Biological Mechanisms of Tooth Movement*. 2nd ed. Wiley-Blackwell.

Levenberg, K. (1944). 'A Method for the Solution of Certain Non-linear Problems in Least Squares'. In: *The Quarterly of Applied Mathematics* 2.2, pp. 164–168.

Levenston, M.E. et al. (1998). 'Variationally derived 3-field finite element formulations for quasistatic poroelastic analysis of hydrated biological tissues'. In: *Computer Methods in Applied Mechanics and Engineering* 156.1, pp. 231–246.

Marlow, Randall S. (2003). 'A General First-Invariant Hyperelastic Constitutive Model'. In: *Constitutive Models for Rubber III*. Ed. by Busfield and Muhr. Lisse: A.A. Balkema.

Marquardt, D.W. (1963). 'An Algorithm for the Least-Squares Estimation of Nonlinear Parameters'. In: *Journal of the Society for Industrial and Applied Mathematics* 11.2, 431—441.

McCutcheon, S.C. et al. (1993). 'Water Quality'. In: *Handbood of Hydrology*. Ed. by D.R. Maidment. New York: McGraw-Hill.

Meyers, Marc A. (1994). *Dynamic Behavior of Materials*. Wiley.

Minns, R.J. et al. (1972). 'The role of the fibrous components and ground substance in the mechanical properties of biological tissues: A preliminary investigation'. In: *Journal of Biomechanics* 6.2, pp. 153–165.

Mooney, M. (1940). 'A theory of large elastic deformation'. In: *Journal of Applied Physics* 11.9, pp. 582–592.

Neter, J. et al. (2004). *Applied linear statistical models*. 5th ed. McGraw-Hill.

Oftadeh, Ramin et al. (2015). 'Biomechanics and Mechanobiology of Trabecular Bone: A Review'. In: *Journal of Biomechanical Engineering* 137.1, p. 15.

Ogden, R. W. (1972). 'Large Deformation Isotropic Elasticity - On the Correlation of Theory and Experiment for Incompressible Rubberlike Solids'. In: *Proceedings of the Royal Society of London A: Mathematical, Physical and Engineering Sciences* 326.1567, pp. 565–584.

Pandolfi, Anna (2012). *An Introduction to Nonlinear Solid Mechanics*. Italy: Politecnico di Milano.

Papadopoulou, Konstantina et al. (2013). 'Biomechanical time dependency of the periodontal ligament: a combined experimental and numerical approach'. In: *The European Journal of Orthodontics* 35.6, pp. 811 –818.

Reese, Stefanie and Sanjay Govindjee (1998). 'A theory of finite viscoelasticity and numerical aspects'. In: *International journal of solids and structures* 35.26, pp. 3455–3482.

Renders, G. A. P. et al. (2007). 'Porosity of human mandibular condylar bone'. In: *Journal of Anatomy* 203.3, pp. 239 –248. URL: `https://www.ncbi.nlm.nih.gov/pmc/articles/PMC2100285/`.

Rendulic, L. (1936). 'Porenziffer und Porenwasserdrunk in Tonen'. In: *Der Bauingenieur* 17, pp. 559 –564.

Rice, James R. (1998). *Elasticity of Fluid-Infiltrated Porous Solids (Poroelasticity)*. Revision 2013. Department of Earth and Planetary Sciences, Harvard University. URL: `http://esag.harvard.edu/rice/e2_Poroelasticity.pdf`.

Rice, James R. and M. P. Cleary (1976). 'Some basic stress-diffusion solutions for fluid-saturated elastic porous media with compressible constituents'. In: *Reviews of Geophysics and Space Physics* 14, pp. 227 –241.

Riches, P.E. et al. (2002). 'The internal mechanics of the intervertebral disc under cyclic loading'. In: *Journal of Biomechanics* 35.9, pp. 1263 –1271.

Rivlin, R.S. (1948). 'Large elastic deformations of isotropic materials. IV. Further developments of the general theory'. In: *Philosophical Transactions of the Royal Society of London. Series A, Mathematical and Physical Sciences* 241.835, pp. 379–397.

Rosenbluth, Michael J. et al. (2008). 'Slow Stress Propagation in Adherent Cells'. In: *Biophysical Journal* 95, pp. 6052–6059.

Roshanian, Jafar et al. (2018). 'Metamodel-Based Multidisciplinary Design Optimization of a General Aviation Aircraft'. In: *Advances in Structural and Multidisciplinary Optimization: Proceedings of the 12th World Congress of Structural and Multidisciplinary Optimization (WCSMO12)*. Ed. by Axel Schumacher et al. 1st ed. Springer.

Rudnicki, J.W. (2001). 'Linear poroelasticity'. In: *Handbook of Materials Behavior Models*. Ed. by J. Lemaitre. 1st ed. Academic Press. Chap. 11.6, pp. 1118 – 1125.

Sandhu, R.S. and E.L. Wilson (1969). 'Finite element analysis of seepage in elastic media'. In: *Journal of the Engineer Mechanics Division* 95.3, pp. 641–652.

Schroeder, Hubert (1986). *The Periodontium*. 1st ed. Vol. 5. Handbook of Microscopic Anatomy. Berlin Heidelberg: Springer-Verlag.

Schwarz, A. M. (1932). 'Tissue changes incidental to orthodontic tooth movement.' In: *International Journal of Orthodontia, Oral Surgery and Radiography* 18.4, 331–352.

Seifzadeh, A. et al. (2012). 'Determination of nonlinear fibre-reinforced biphasic poroviscoelastic constitutive parameters of articular cartilage using stress relaxation indentation testing and an optimizing finite element analysis'. In: *Computer Methods and Programs in Biomedicine* 107.2, pp. 315 –326.

Severino, P. C. Marques and J. Creus Guillermo (2012). *Computational Viscoelasticity*. 1st ed. Springer Briefs in Applied Sciences and Technology. Berlin Heidelberg: Springer-Verlag.

Sharpe, William N. (2008). *Springer Handbook of Experimental Solid Mechanics*. LLC New York: Springer Science+Business Media.

Simo, J. C. (1987). 'On a Fully Three-dimensional Finite-strain Viscoelastic Damage Model: Formulation and Computational Aspects'. In: *Computer Methods in Applied Mechanics and Engineering* 60.2, pp. 153–173.

Skempton, AW (1954). 'The pore-pressure coefficients A and B'. In: *Geotechnique* 4.4, pp. 143–147.

Sloan, P. (1978). 'Scanning electron microscopy of the collagen fibre architecture of the rabbit incisor periodontium.' In: *Archives of Oral Biology* 23.7, pp. 567–572.

Storåkers, B. (1986). 'On material representation and constitutive branching in finite compressible elasticity'. In: *Journal of Mechanics Physics of Solids* 34, pp. 125–145.

Taylor, Robert L. et al. (1970). 'Thermomechanical analysis of viscoelastic solids'. In: *International Journal for Numerical Methods in Engineering* 2.1, pp. 45–59.

Terzaghi, K. (1923). 'Die Berechnung der Durchlässigkeitsziffer des Tones aus dem Verlauf der hydrodynamischen Spannungerscheinungen'. In: *Sitzungsberichte der Akademie der Wissenschaften in Wien, mathematish-naturwissenschaftliche Klasse, Abteiling IIa*. Vol. 132, pp. 125–138.

Toms, Stephanie R. et al. (2002). 'Quasi-linear viscoelastic behavior of the human periodontal ligament'. In: *Journal of Biomechanics* 35, pp. 1411–1415.

Treloar, L. R. G. (1943). 'The elasticity of a network of long chain molecules (I and II)'. In: *Transactions of the Faraday Society* 39. pp. 36-64 and 241-246.

Trendelenburg, F. (1939). *Einführung in die Akustik*. Berlin Heidelberg: Springer-Verlag.

Truesdell, C. (1969). *Rational thermodynamics*. New York: McGraw-Hill.

Verruijt, Arnold (2008). 'Consolidation of Soils'. In: *Encyclopedia of Hydrological Sciences*. Ed. by Malcolm G. Anderson. John Wiley & Sons, Ltd.

— (2013). *Theory and problems of poroelasticity*. Netherlands: Delft University of Technology.

Wang, H.F. (2000). *Theory of Linear Poroelasticity*. Princeton University Press.

Wells, Peter N.T. and Hai-Dong Liang (2011). 'Medical ultrasound: imaging of soft tissue strain and elasticity'. In: *Journal of the Royal Society Interface* 8.64, pp. 1521–1549.

Yeoh, O.H. (1990). 'Characterization of elastic properties of carbon-black-filled rubber vulcanizates'. In: *Rubber Chemistry and Technology* 63, pp. 792–805.

Zhurov, Alexei et al. (2007). 'A constitutive model for the periodontal ligament as a compressible transversely isotropic visco-hyperelastic tissue'. In: *Computer Methods in Biomechanics and Biomedical Engineering* 10 (3), pp. 223–235.

Zienkiewicz, O.C. et al. (2005). *The Finite Element Method: Its Basis and Fundamentals*. 6th ed. Oxford: Elsevier Butterworth Heinemann.

Zimmerman, R.W. (2000). 'Coupling in poroelasticity and thermoelasticity'. In: *International Journal of Rock Mechanics and Mining Sciences* 37, pp. 79–87.

Zimmerman, RW et al. (1985). 'The Effects of Pore Pressure and Confining Pressure on Pore and Bulk Volume Compressibilities of Consolidated Sandstones'. In: *Measurement of Rock Properties at Elevated Pressures and Temperatures*. Ed. by H.J. Pincus and E.R. Hoskins. Vol. 869. ASTM STP, pp. 24–36.